72-9036

INHABER, Herbert, 1941-
    SUPERCONDUCTIVITY AND HYSTERESIS IN INDIUM-
CADMIUM ALLOYS.

    The University of Oklahoma, Ph.D., 1971
    Physics, solid state

THE UNIVERSITY OF OKLAHOMA

GRADUATE COLLEGE

SUPERCONDUCTIVITY AND HYSTERESIS IN INDIUM-CADMIUM ALLOYS

A DISSERTATION

SUBMITTED TO THE GRADUATE FACULTY

in partial fulfillment of the requirements for the

degree of

DOCTOR OF PHILOSOPHY

BY

HERBERT INHABER

Norman, Oklahoma

1971

SUPERCONDUCTIVITY AND HYSTERESIS IN INDIUM-CADMIUM ALLOYS

APPROVED BY

Keith J. Carroll

C. T. Sikora

R. A. Levy

S. E. Bull, Jr.

DISSERTATION COMMITTEE

PLEASE NOTE:

Some Pages have indistinct
print. Filmed as received.

UNIVERSITY MICROFILMS

ACKNOWLEDGEMENTS

This work is dedicated to my wife, Elizabeth, without whose self-sacrifice I could not have succeeded.

"Pacience is an heigh vertu, certeyn"

(Chaucer, The Franklin's Tale).

Dr. Keith Carroll provided the inspiration for this project. He gave a great deal of help with the theoretical and experimentals aspects of this work, and asked the right questions at the right time.

David Wilson provided some much-needed experimental insight at crucial junctures.

Lester Sisemore and James Nicholson, my co-workers on low temperatures, cooperated with the distribution of our precious liquid helium, and provided encouragement.

Brian Johnston helped build some of the vacuum apparatus, and wrote a much-used FORTRAN program.

TABLE OF CONTENTS

LIST OF TABLES

LIST OF ILLUSTRATIONS

SUPERCONDUCTIVITY AND HYSTERESIS IN INDIUM-CADMIUM ALLOYS

CHAPTER I

INTRODUCTION

The most striking feature of all superconductors (and the first of their properties to be discovered) is the lack of any electrical resistance below a well-defined critical temperature T_c. For superconductors, T_c ranges from a few millidegrees K to about 20 K.

However, in the past half-century many more unusual attributes of superconductors have been found. Prominent among these characteristics has been their behavior under an applied magnetic field. In fact, the differences in this response in bulk superconductors (i.e., those of greater thickness than thin films) have led to two general classifications: Type I and Type II. Although Type I superconductors were discovered first (by Onnes, in 1911), considerable work has been done on the latter since the pioneering of Shubnikov et al (1).

As a rule of thumb, Type I superconductors tend to be elements and alloys whose current-carrying ability (before superconductivity is extinguished) is low; Type II superconductors tend to be alloys with higher current-carrying ability. However, there are exceptions and the distinctions will be put on a more physical basis in the next section.

In this work we shall discuss the magnetization properties of Type

II superconductors. Specifically, we shall deal with Indium-Cadmium alloys. The reasons for discussing this system are (a) a large amount of data has been published on the alloys of indium, and thus it will be useful to compare these alloys to the others in terms of their superconducting parameters; (b) comparatively little superconducting work has been performed on this system because of the low solubility of Cd in In at room temperature. Noting that Cd has a greater solubility at higher temperatures, the problem was alleviated by cooling the alloys rapidly from these temperatures, preserving the lattice structure.

In addition to this work, a discussion of hysteresis in superconductors will be presented. Hysteresis is that condition in which a one-to-one correspondence between the applied magnetic field and the resultant magnetization of the sample is not achieved. In superconductors, we often find that the magnetization for a decreasing field is less than that of the increasing field. We shall discuss this effect in the light of present-day theories of superconductivity.

As well as In-Cd alloys, work has been done on other alloys which show more of a Type I characteristic.

CHAPTER II

TYPE II SUPERCONDUCTIVITY

The theoretical aspects of Type II superconductivity pertinent to experimental data are now discussed. Consider first typical data and the quantities derivable from them. In Figs. 11a and 11b perfect diamagnetism (i.e., B = 0) exists until the point where flux first penetrates the sample, at $H = H_{c_1}$. In Type I superconductors, the point of initial flux penetration is that of total flux penetration, so that $H_{c_1} = H_{c_2} = H_c$. At the applied field H_{c_2}, the specimen becomes normal with a second order transition. The order of the transition is determined by specific heat discontinuities and the fact that the volume change at this transition is zero (30). Using the concept of the critical field H_c,

$$\int_0^{H_{c_2}} M \, dH = -H_c^2/8\pi \tag{2.1}$$

where M is the magnetization. The critical field H_c is not observed experimentally in Type II superconductors, but is still a useful parameter.

H_c, H_{c_1}, H_{c_2}, and many superconducting variables are determined thermodynamically and have a temperature variation. The magnetization M is then dependent on temperature. A general idea of this dependence is given in Figs. 1a and 1b. It should be noted before pro-

3
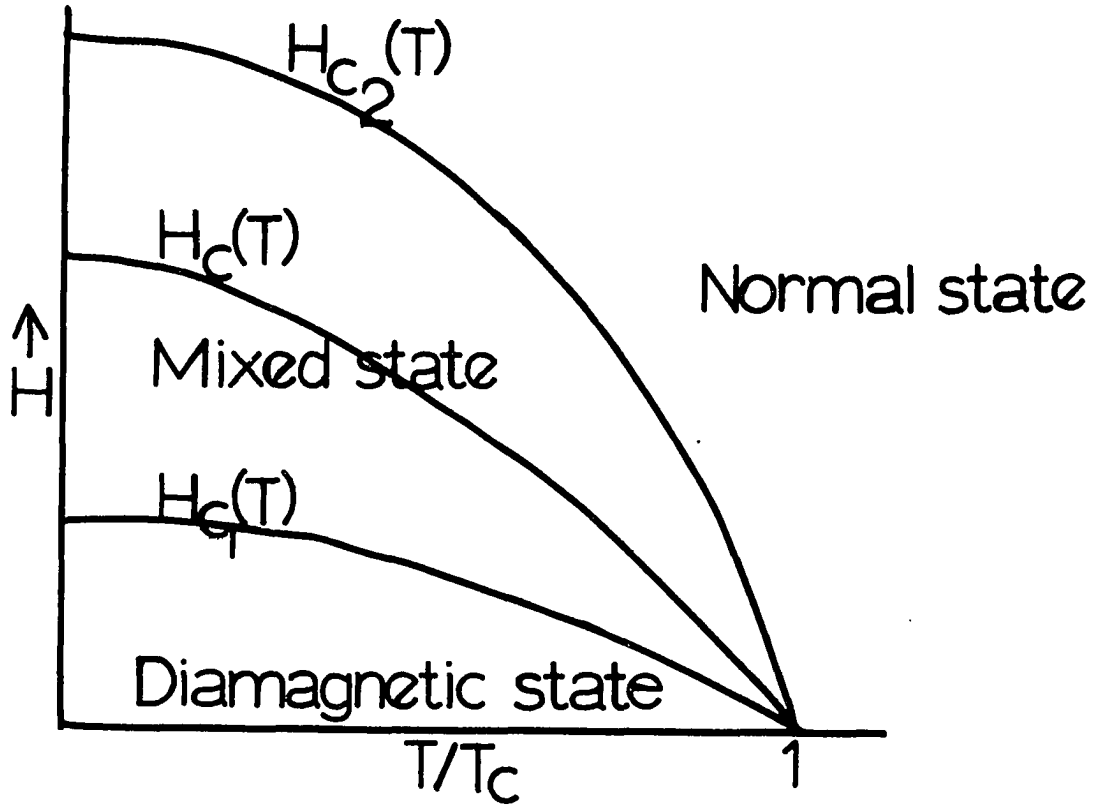
Fig. 1a. Variation of critical fields in a Type II
superconductor with temperature.
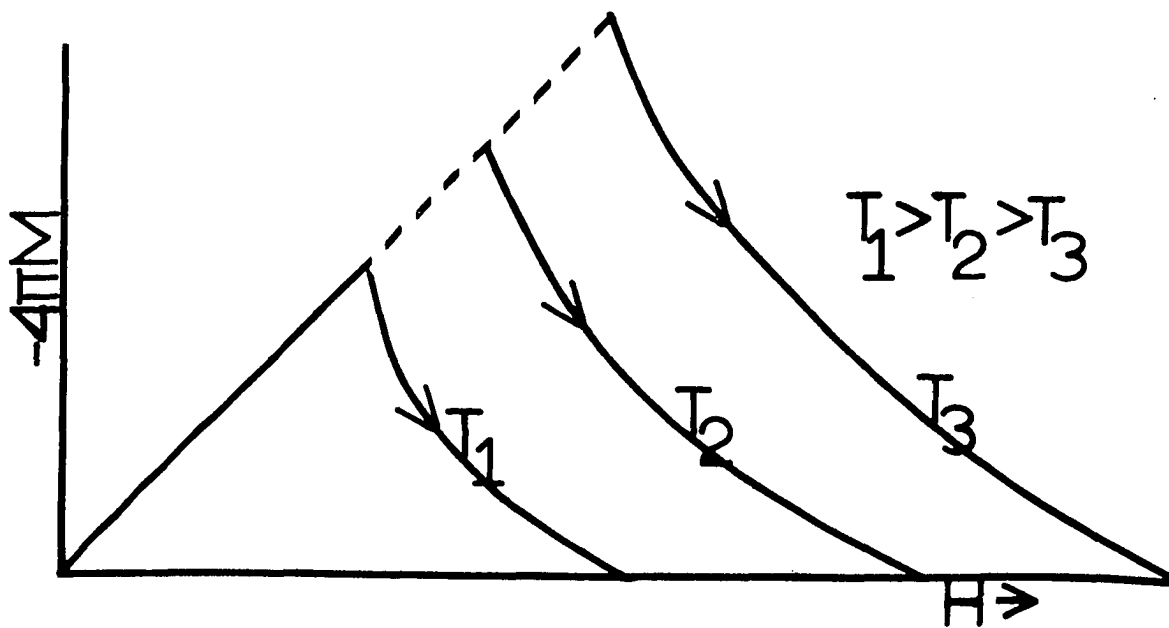
Fig. 1b. Variation of magnetization in a Type II superconductor with
temperature.

ceeding that we shall consider only the geometry of a long cylindrical

sample in a uniform magnetic field parallel to its axis, corresponding

to the conditions of this experiment. In Fig. 1a, T_c is the temperature

at which all traces of superconductivity disappear.

The most successful efforts to describe the macroscopic propert-

ies of superconductors in terms of microscopic behavior have been those

of Ginzburg and Landau (GL) (2) and Bardeen, Cooper and Schrieffer (BCS)

(3). Abrikosov (4) discussed Type II superconductivity by using the GL

differential equations. Both experimental and theoretical aspects of Type

II superconductivity have been reviewed by Goodman (5) and Saint-James

et al (6). Only results relevant to this work will be presented.

The BCS theory is based on the fact that if there is an attractive

interaction between electrons, those which are in the neighborhood of the

Fermi surface will condense into a state of lower energy. This interact-

ion produces a state where each electron is paired with one of opposite

momentum and spin. Then the scattering which was allowed in the now energ-

etically unfavorable normal state is forbidden, and the correlated pairs

can now carry lossless current without inelastic scattering, i.e., cur-

rent without resistance. We have, if $N(0)V \ll 1$,

$$\frac{1}{N(0)\ V} = \log \frac{1.14\ \hbar\omega_D}{k\ T_c} \qquad (2.2)$$

where $N(0)$ is the density of states per unit energy and volume at the

Fermi level, ω_D is the Debye frequency, k is the Boltzmann constant,

and V is the electron-electron interaction strength.

There are two parameters, having the dimensions of length, which

are useful in the theory of superconductivity. ξ is the range of coher-

ence of the superconducting wave functions, and λ_L is the penetration

depth at which the field has fallen to $1/e$ of its value at the surface (7). The ratio of the two lengths can be shown to be

$$\lambda_L/\xi = H_{c_2}/H_c = \sqrt{2}\kappa ; \qquad (2.3)$$

κ is called the GL parameter. In deriving this, the GL theory, which is based on the Landau-Lifshitz theory of second order phase transitions, has been used. Strictly speaking, the former theory is applicable only at temperatures near T_c; however, it has been used for other temperatures. Other derivable formulas are

$$H_c = \pi k T_c \{2\pi N(0)/8.4\}^{\frac{1}{2}}\{1 - (T/T_c)\} \qquad (2.4)$$

near $T = T_c$;

$$H_c \xi \lambda_L = \phi_o/4\pi \qquad (2.5)$$

where ϕ_o ($=\hbar c/2e$) is the flux quantum. Each of Abrikosov's (4) fluxoids carry flux quantized in units of ϕ_o. These fluxoids are the entities distinguishing Type II from Type I superconductors. They consist of a normal tube, parallel to the applied field, of radius $\sim \xi$, surrounded by a sheath of supercurrent of radius $\sim \lambda_L$. Goodman (5) shows how these properties may be determined from the original GL equations. It has been shown theoretically and experimentally (8) that the lowest energy configuration for these fluxoids is triangular. The fluxoids appear only when the flux penetrates macroscopically (H $\geq$ H_{c_1}) and the interfluxoid distance is

$$d = (4/3)^{\frac{1}{4}}\sqrt{\phi_o/B} \qquad (2.6)$$

Unfortunately, the resultant equations relating applied field, lattice structure and λ_L are in the form of an infinite series of Bessel functions of imaginary argument. However, when H $\simeq$ H_{c_2}, they can be

written in the form

$$- \frac{4\pi dM}{dH} = \frac{1}{1.16(2\kappa_2^2 - 1)} \tag{2.7}$$

We now have two parameters, κ and κ_2. The former was merely defined in the GL theory as the ratio of the two lengths of Eq. (2.3). The second relation of this equation will define a parameter κ_1. κ_2 in Eq. (2.7) is a new generalized GL parameter; it has been shown theoretically (9 - 10) that $\kappa_1(T) = \kappa_2(T)$ to within a few percent over the entire range of T, and that $\kappa_1(T_c) = \kappa_2(T_c)$. Maki (9) also introduced another GL parameter κ_3 to relate the first penetration field H_{c_1} to the critical field H_c:

$$H_{c_1}(T) = \{H_c(T)/2\kappa_3(T)\}\log \kappa_3(T) \tag{2.8}$$

Goodman (11) defined yet another GL parameter, labelled κ_4, defined by

$$\kappa_4 = \kappa_o + 7.53 \times 10^{-3} \gamma^{\frac{1}{2}} \rho_n, \tag{2.9}$$

where κ_o is the GL parameter of the pure (unalloyed) material which forms the main component of the alloy, ρ_n is the normal state resistivity, in $\mu\rho$ - cm, and γ is the electronic coefficient of specific heat, in erg - cm^{-3} - K^{-2}. Since almost all superconducting elements (as opposed to alloys or compounds) are Type I, $\kappa_o \approx 0.1$.

One reason why we deal with parameters like κ_1, κ_2, and not only with physical quantities like H_{c_1} and H_{c_2} is that we are concerned with the shape and slope of the magnetization curve, as evidenced by H_c and - $4\pi(dM/dH)$. The GL parameters enable us to characterize these quantities.

In Eq. (2.3), if $\kappa \leq 1/\sqrt{2}$, Abrikosov (12) showed that we have

Type I superconductivity. We thus can use the GL parameters to determine easily the type of superconductors under study.

Three separate theories of superconductivity (Ginzburg-Landau, BCS and Abrikosov) have been dealt with. The derivation of the last from the first has already been mentioned; Gorkov (13) determined the equivalency of the BCS and GL formulations.

We have said very little as yet about the metallurgical aspects of superconductivity. Since we have quantities like the Fermi velocity, mean free path of electrons(through the normal state resistivity), as well as the whole range of defect structure (through the common hysteretic behavior of the magnetization curves), the metallurgy of the sample plays a large part in the final results. Livingston and Schadler (14) reviewed much of the literature on this subject. However, for the moment we shall not discuss all these aspects, but later on we shall develop those parts germane to the present work.

In this spirit, there are other equations which could be developed on Type II superconductors, both as a combination of the preceding equations and from the fundamental theory. To conserve space, we shall produce them only as needed in the subsequent sections, as a generally adequate overview of Type II superconductivity has been given in the preceding pages.

CHAPTER III

EXPERIMENTAL PROCEDURES

In this section we shall describe and discuss the experimental procedures used in this work.

Sample Preparation

The samples were cast in the form of cylinders, in order to simplify geometrical considerations. The sample holder was constructed from a Teflon rod; its dimensions are illustrated in Fig. 2a. It was made as large as possible consistent with the size of the pickup coils which detected the signal. The lower section, where the actual sample rests after preparation, is a cylindrical mold with a 2.0 x 20 mm. bore. The larger chamber above serves as a holder for the constituent elements of the alloy, as well as a mixing chamber.

The In used was supplied by Cominco American Inc. (lot HPM 8908) and was claimed to be 99.9999% pure. The Cd was supplied by Electronic Space Products Inc. (lot K960D) and claimed to be of the same purity. The precut and weighed pieces of the elements were placed inside the large chamber of the holder. In order to achieve the exact percentage compositions desired, it was occasionally necessary to have samples which had a total mass slightly different from sample to sample. (Typical sample weight was 0.43 grams.) The difference was no greater than

LEGEND
Search coil
dc Electromagnet
Stainless steel supports

TO SCALE

Plug

3.8 mm.

10.5 mm.

sample holding & mixing chamber

35 mm

20 mm.

sample mold (2.03 mm.)

Fig. 2a. Sample holder

TO SCALE

3.5"

B

3 "

M

T

1.3"

5.6"

4.4"

1.4"
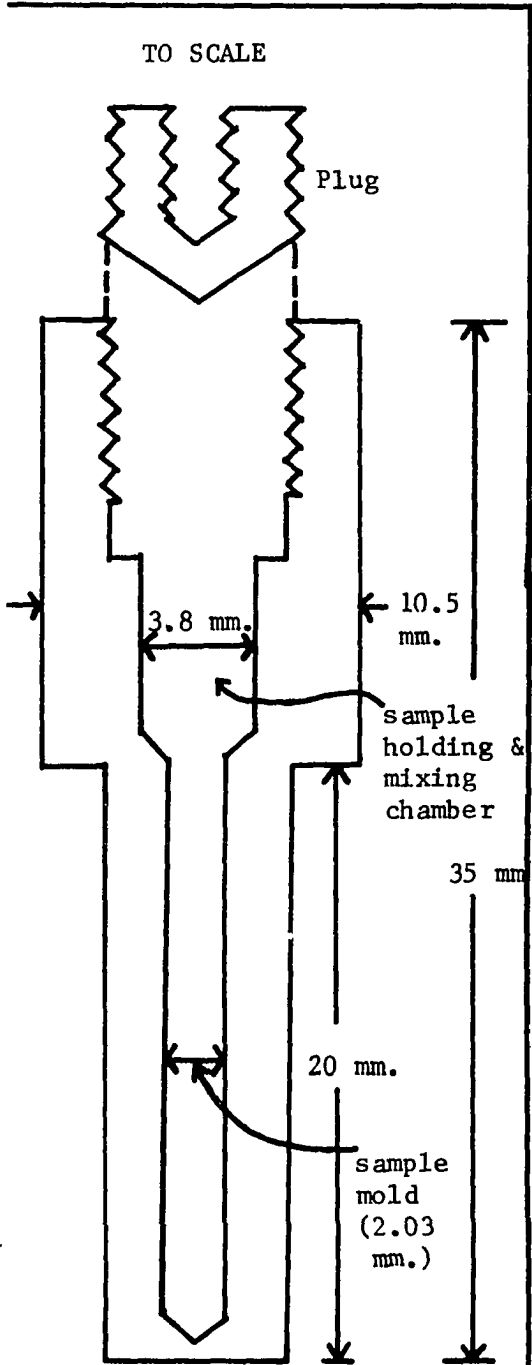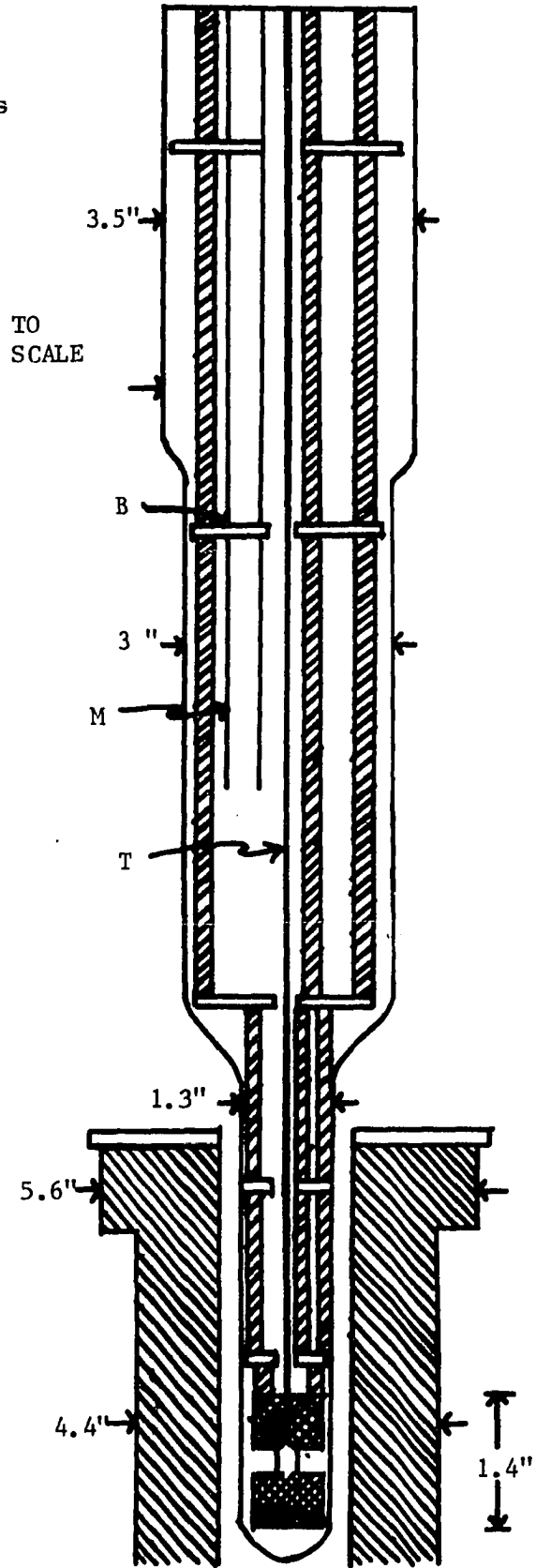
Fig. 2b. Experimental cryostat

a few percent. However, the experimental procedure employed "normal-izes" the data with respect to mass and no correction is necessary.

A large problem in preparing any alloy is ensuring that the constituents are properly mixed. A fairly elaborate procedure was devised in the present work to make certain of this.

After the Teflon plug was screwed into the sample holder, it was placed in a glass tube suspended in a furnace. The tube was evacuated to 2 microns of pressure or less, flushed with argon, and the procedure repeated. The constituents of the alloy were then melted together. However, a problem which arose was that the upper limit of temperature of the furnace was about 240 C, while the melting point of Cd is 321 C. The difficulty was obviated by noting that the melted In would have a high interdiffusion rate with the solid Cd at that temperature (240 C). It was assumed that after a 24 hour melting period at 240 C the Cd would have completely diffused into solution. Subsequent magnetization measurements, to be discussed, bore out this conclusion.

The sample holder was agitated to ensure that the molten alloy had fallen completely into the lower chamber.

After this first stage, the sample was slowly cooled to room temperature under vacuum. It was then exposed to air, and inspected to see if all the Cd had melted. This proved almost always to be the case.

In the second stage, the plug was screwed completely into the sample holder, and the holder, after a series of evacuations and flushings similar to that of the first stage, was sealed off under a few mm of argon in a glass tube about 3" in length.

The sealed-off tube was then fastened in a special holder and rotated in a vertical plane after being heated to 240 C again for about two days. The exact times of rotations and heating are listed in the chapter on results. It was felt that this long period of rotation and heating ensured the homogeneity of the sample. After the rotation, the sample was positioned vertically in the oven, and lightly shaken for 5 more minutes. This forced the material down into the cylindrical section of the sample holder. If any material accidentally remained outside the cylinder, the resultant magnetization curves proved aberrant and the sample was then discarded.

In the third stage, the sample was annealed at the appropriate temperature for at least 15 days. The temperature used will be discussed in the section on metallurgy. The temperature was lowered from 240 C to the annealing temperature at no greater than 20 C/hr., in order to maintain phase equilibrium.

The time of annealing was chosen on an empirical basis, after shorter annealing times produced inadequate samples. Of course, the sample was undisturbed during the annealing. When complete, the sample was removed from the furnace, the glass envelope broken, and the sample kept in liquid nitrogen until the measuring apparatus was sufficiently cold to make certain that the sample was not inadvertently warmed by being placed in it. The transfer process from oven to nitrogen bath took less than 20 seconds. The sample was then ready for use.

Metallurgical Considerations

In Fig. 3 we see the phase diagram of the In-Cd system (15), for
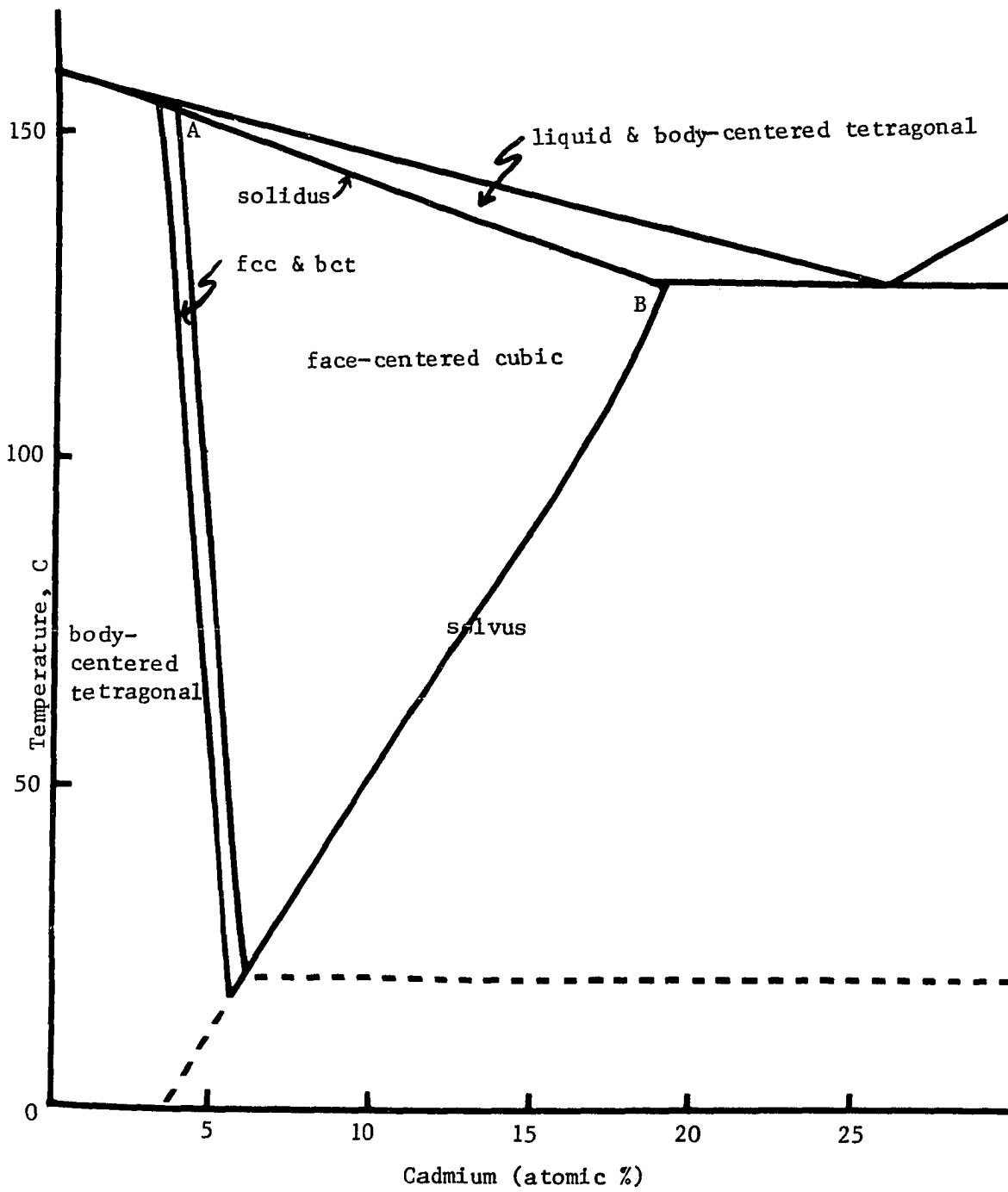
Fig. 3. Phase diagram of Indium-Cadmium system

the In-rich portion. Until the present work, almost all efforts dealing with superconductive aspects of this alloy have concentrated on the bct phase, below 6 atomic % Cd. However, the fcc phase may be investigated if sufficient care is taken.

If we have, for example, a 16 at. % Cd alloy at T = 125 C, Cd will tend to precipitate if the temperature is lowered below 97 C. This will of course change the metallurgical properties of the sample. However, if the temperature is lowered rapidly below the solvus line, the initial lattice structure will be retained. As Rhines (16) points out, the diffusion velocity (and so the rate of precipitation) is halved for a decrease in temperature of about 50 C, so that the precipitation rate is about 60 times less at liquid nitrogen temperature (- 196 C) than at a typical solvus temperature in this diagram.

In conjunction with this last statement, when annealing the alloy we wish the diffusion rate (of non-fcc phases into the fcc phase, and of lattice imperfections into perfect lattices) to be as large as possible, so we anneal close to the line AB. For convenience, for most alloys this was taken as 125 C.

In a related paper, Heumann and Predel (17) found that the unit cell volume decreased from 104.9 kX^3 to 102.7 kX^3 linearly, as the concentration was increased from 0 to 15.3 at. % Cd. If we assume that this also occurs at low temperatures, we have

$$D = 7.30 + (A/100) \tag{3.1}$$

where D is the density of the alloy, and A is the atomic percent Cd. Densities of In and Cd at 0 C are 7.30 and 8.64, respectively. Their atomic weights are 114.82 and 112.4, respectively. Thus the average at-

omic weight is

$$114.82(1 - A) + A(112.4) = 114.82 - 2.4A. \tag{3.2}$$

Since In and Cd have 3 and 2 electrons/atom, respectively, the number of pairs/atom is

$$N = 1.5 - 0.5A. \tag{3.3}$$

Combining Eqs. (3.1), (3.2), and (3.3), we have

$$\frac{\text{electron pairs}}{\text{cc}} = \frac{6.02 \times 10^{23}(7.3 + A)(1.5 - 0.5A)}{114.82 - 2.4A} \tag{3.4}$$

This quantity will be used in a later section.

Experimental Cryostat

The cryostat used in the experiments is depicted in Fig. 2b. This inner dewar, filled with liquid helium, is suspended in a liquid nitrogen bath (not shown) to pre-cool its interior.

The sample is connected by its end plug to a stainless steel thrust rod T which extends out of the top plate of the cryostat. In operation, the sample is pushed manually by means of the rod from the upper search coil to the lower one. The search coils were wound commercially and each consists of 8000 turns of #40 wire. They are connected in series and wound in opposition, to reduce the effect of external field changes.

The rest of the cryostat is built around this lower part. A further consideration is minimizing the helium loss. Thus, the cryostat's length is such that the top, at room temperature, is a considerable distance from the helium level. A series of baffles B is used to reduce radiation inflow. The support rods are made of stainless steel.

A manometer tube M for measurement of temperature is shown in Fig. 2b, as well as the dc electromagnet. Both will be discussed later.

16

Because helium gas will, over a period of time, permeate the glass of the dewar, the jacket was occasionally re-evacuated.

The general principles of cryostat design are described by White (18).

dc Electromagnet

The position of the dc electromagnet, used to produce a uniform magnetic field around the sample, is shown in Fig. 2b. It is positioned so that the center of the search coils is at its center. It is suspended in the liquid nitrogen, and has a current capacity of at least 14 A.

The electromagnet is powered by a regulated and very stable Hewlett - Packard 6268A dc power supply (with current regulation of 0.1%) connected in series to a switching circuit of high-wattage resistors. The resistors enable the experimenter to reduce the sensitivity and thus to maximize the selectivity of the voltage and current controls of the power supply.The resistance of the electromagnet at 77 K is 1.7Ω.

The electromagnet was wound on the Garrett (19) principles, i.e., with appropriate correction coils on the ends to make the center field extremely uniform. The coils were wound with about 20 longitudinal strips of nylon wire between each copper wire layer (to allow the liquid nitrogen to circulate) and had a length of 9". Other dimensions are in Fig. 2b. The computed field variation along the center axis is shown in Fig. 4a. It is constant to 0.1% for a total distance of 3.2".

Using the coil geometry, we find that at the center of the magnet,

$$H = 1694 \ V, \tag{3.5}$$

where V is the voltage across a precision resistor of resistance = .1044Ω, carrying the magnet current, and H is the magnetic field in Oe. Dr. S. E. Babb, Jr. measured the resistance.
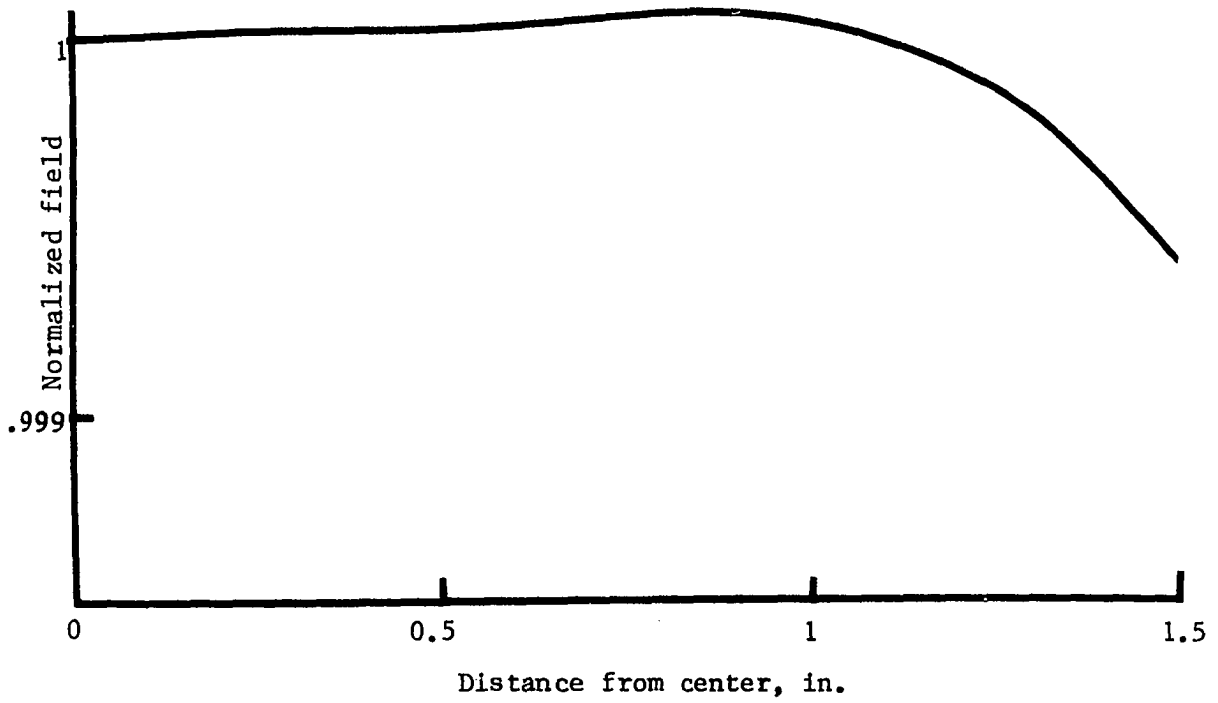
Fig. 4a. Electromagnet field along axis (normalized)
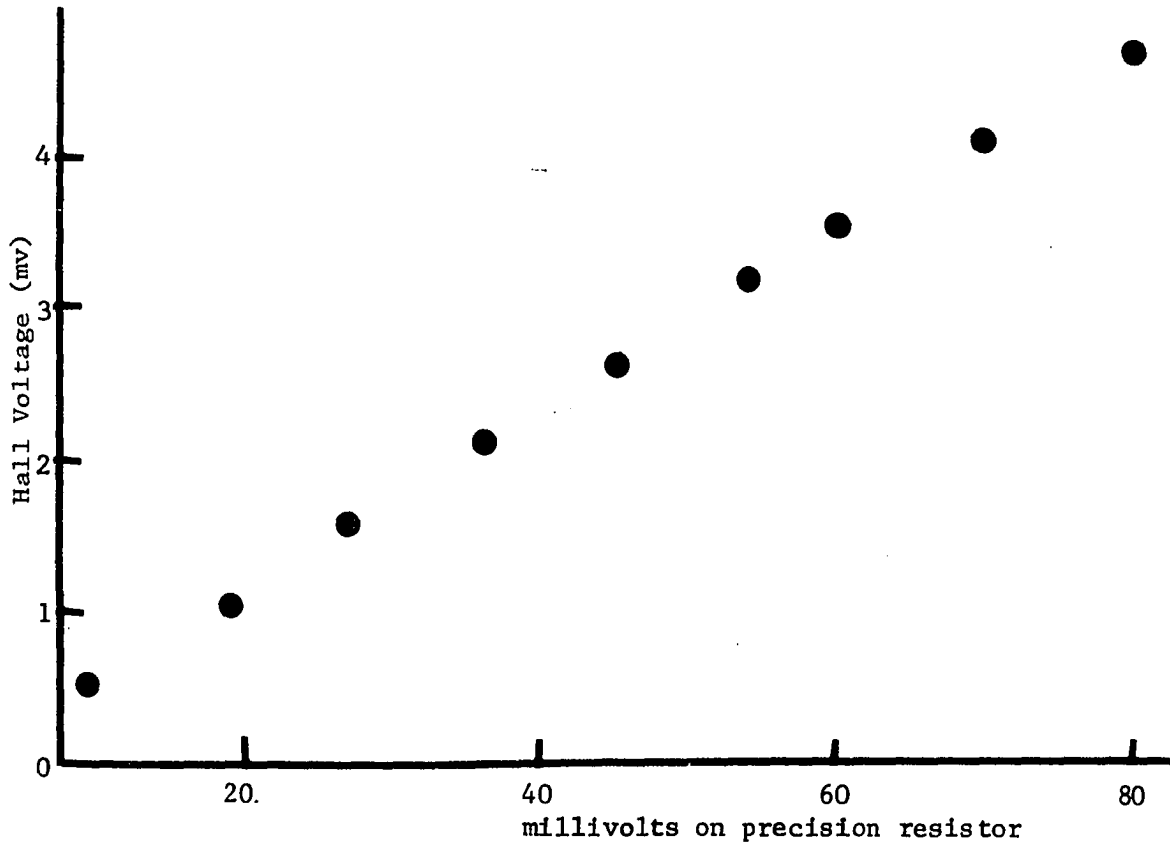
Fig. 4b. Hall voltage of Electromagnet

The field in the magnet was measured by L. Sisemore and J. Nicholson, using a Hall probe. In Fig. 4b the results of their determination is shown. The Hall probe was calibrated by means of a standard magnet, and their results yield

$$H = (1704.8 \pm 9.9) \ V \qquad (3.6)$$

which makes the calculated value very close to the experimental value. The error sign in the last equation refers to two standard deviations. The average of the coefficients of Eqs. (3.5) and (3.6) (1700) was used in calculations.

Experimental Method

The standard (20) ballistic throw method was the basis of these experiments. If a body with magnetization M is moved through a constant magnetic field, the change in flux linkage can be made to produce an emf in a coil. This emf is proportional to the magnetization of the body. The coils used are the search coils of Fig. 2b. The motion is produced by pushing on the thrust rod T. The search coils and electromagnet were carefully aligned with respect to each other. The signal was sent through an L&N 2285E ballistic galvanometer, with a circuit arranged to produce the maximum signal with a large degree of damping. The circuit is shown in Fig. 5a. It was found theoretically and experimentally that the time T taken to push the sample through the search coils did not affect the results, as long as T ≤ 2 sec.

The deflection of the galvanometer in response to the induced emf was measured on a wall chart, approximately 12 ft. from the instrument. The nonlinear scale of the chart had a typical scale of 2.5" ≈ 1 degree, so that increments of 0.01 degree could be read.

LEGEND
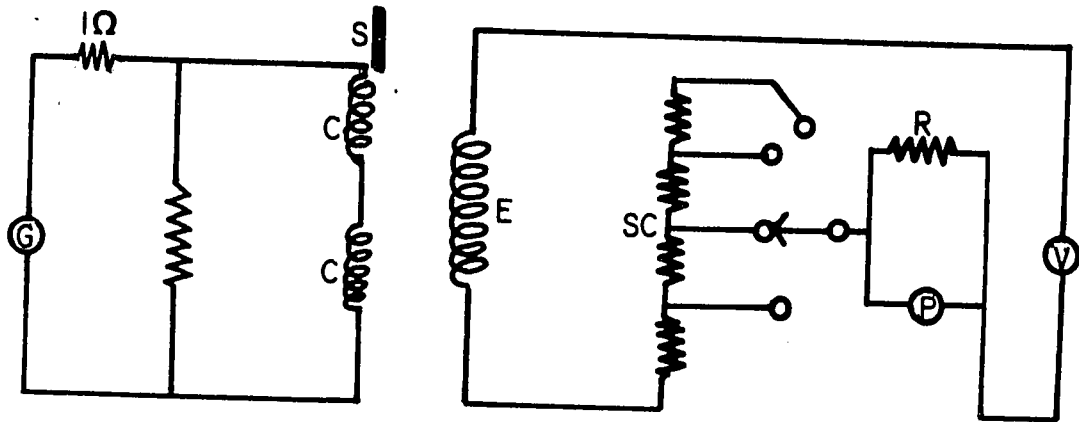
S — Sample   SC — High-wattage switching circuit
C — Search coils   E — Electromagnet
P — Potentiometer   R — Precision resistor
G — Galvanometer (wall)   V — Regulated power supply

Fig. 5a. Experimental circuitry to measure magnetization of superconductors.
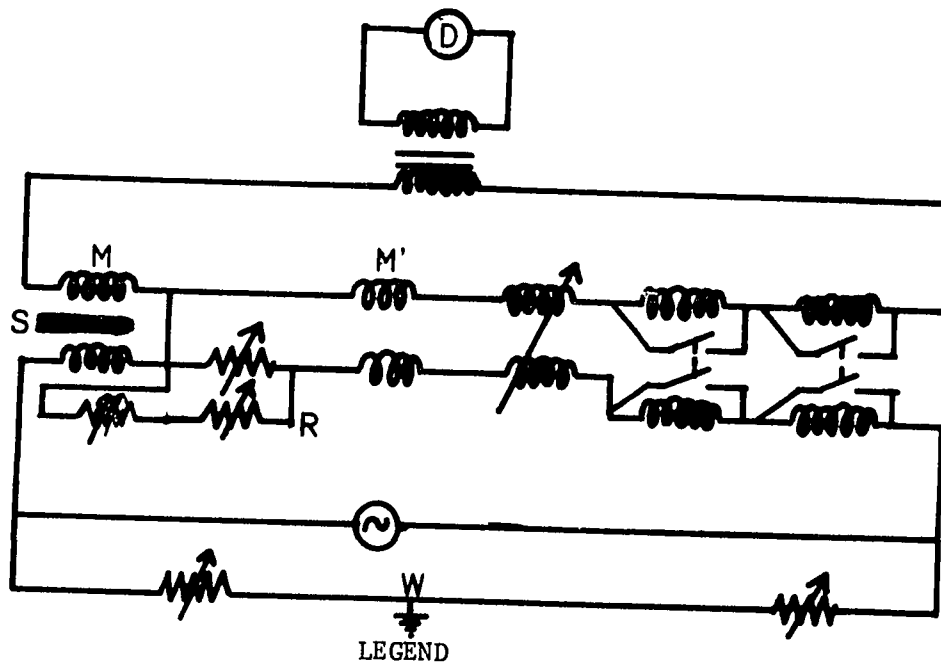
LEGEND

W — Wagner ground   R — Variable resistances
S — Sample   D — Detector
∿ — Oscillator   M — Sample coils
M'— Compensating coils

Fig. 5b. Circuit to measure normal state resistivity.

The voltage across the precision resistor was monitored by a potentiometer (L&N K3) and was converted to magnetic field by the previous relation. We now have a correspondence between magnetic field and the wall galvanometer deflection when the sample is thrust from one search coil to another.

The problem of calibration was handled by noting that the sample is perfectly diamagnetic for $-4\pi M < H_{c_1}$; i.e., $-4\pi M = H$ over that range. The slope of the deflection vs. field graph was found using at least 6 measurements and a least squares fit for each alloy and temperature, and converted to magnetization using $H = 1700V$. There were only slight changes in this slope for changes in sample and composition. As mentioned above, the volume of the sample plays no part in this calculation.

The actual experiment begins by cooling the apparatus down by using liquid nitrogen in the outer dewar. The sample holder is then screwed on the thrust rod quickly, to prevent it from warming. The sample and search coils are then briefly immersed in liquid nitrogen before being returned to the inner dewar. The entire transfer process takes less than 40 sec.

Liquid helium is then added to the inner dewar, and pumped down to the appropriate temperature. The readings are then taken, with a field being set by adjustment of the power supply and the wall galvanometer deflection noted. The liquid helium lasted approximately 2 hr. for most experiments.

The temperature of the sample may be changed in the course of the experimentation. Due to convection problems in the helium bath, this is not done by merely changing the pumping rate. Instead, a small heat-

er below the sample was used to raise the temperature of the bath above T_c. The temperature is then lowered the appropriate amount. The procedure ensures the removal of any trapped flux.

A small correction to the magnetization results was made. When an empty sample holder was used, a small but significant increase in deflection was noted with increasing magnetic field. This effect was probably due to the earth's magnetic field, slight magnetization of the stainless steel thrust rod, and other causes. When the effect was first noted, the equation of the correction was

$$D = 0.569V + 0.099 \qquad (3.7)$$

where D is the deflection in degrees, and V is the voltage across the precision resistor. Since the effect was found to increase slightly with time, periodic re-evaluations of the constants in this equation were undertaken. D was subtracted from the experimental deflection values. B. Johnston wrote a computer program in FORTRAN which corrected data for these residual deflections, converted deflections into magnetization, and computed the GL parameters (κ_1, κ_2, and κ_3), H_c, H_{c_1} and H_{c_2}.

Resistivity

In Eq. (2.10), it is shown that the normal-state resistivity (or residual resistivity) will play a part in the theory of Type II superconductors. Since the resistivity changes very little at low temperatures, the residual resistivity will be taken to mean the resistivity at 4.2 K (the temperature of liquid helium at atmospheric pressure), if the material concerned is not superconducting at that temperature.

However, because of the construction of the sample holder it would have been difficult to measure the resistivity by the standard 4-probe method. Furthermore, because of the danger of Cd precipitation if the sample is warmed up inadvertently, this technique would have been made more difficult. Due to the sensitive metallurgy of the samples, it was also decided to determine the resistivity of the actual samples, rather than that of similar specimens. The limitations imposed by the above constraints require the resistivity to be determined by an indirect method. The technique chosen was that of Chambers and Park (21). The resistivity can be deduced from the change of mutual inductance between two coils when the sample is introduced. To eliminate end effects, the two coils consisted of a long primary and a secondary coil about ¼ the length of the sample and centered on it. The circuitry is shown in Fig. 5b. It is essentially a Hartshorn bridge.

The bridge is balanced by adjusting the mutual inductances and resistances. The sample is then inserted in M and the bridge again balanced. If δM and $\delta R/\omega$, where ω is the angular frequency of the oscillator, are plotted versus the frequency f (= $\omega/2\pi$), we obtain, typically, Fig. 6. Chambers and Park find where the curves intersect that

$$f_m = 0.0803 \, \rho/a^2 \qquad (3.8)$$

where f_m is the frequency of intersection in Khz, a is the sample radius in cm., and ρ is the resistivity in $\mu\Omega$ - cm. Isotropic resistivity has been assumed. We thus have an equation for the resistivity in terms of measurable quantities.

In Fig. 5b, the proper grounding of the apparatus was very essential, and this is done by means of a Wagner ground (designed to put the detector at ground potential).

23
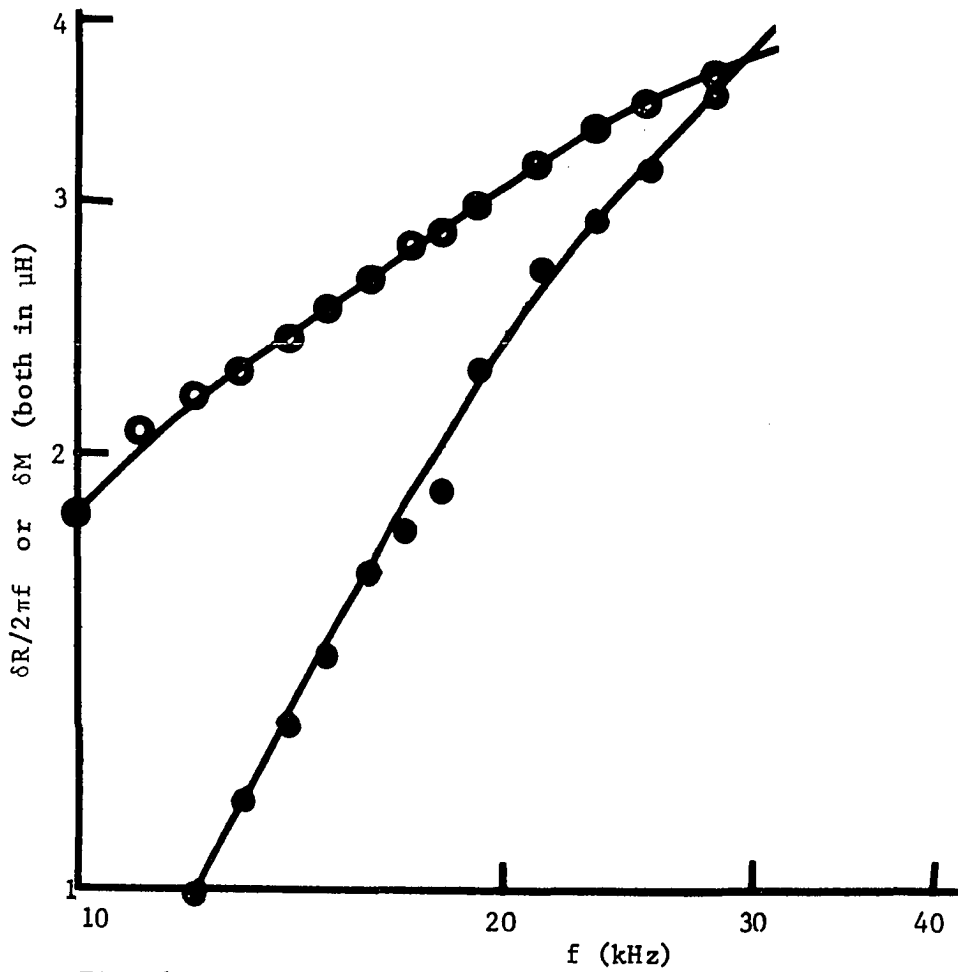
Fig. 6. Determining resistivity by Chambers' method

Other authors have found the same problem. Two of the resistances R were commercial non-inductive resistance boxes, having divisions of 100 mΩ. The third was built in the laboratory using short strips of copper wire, and had divisions of about 5 mΩ. By using these boxes in parallel, changes in resistance of 1 mΩ could be detected. All values of resistance and inductance were measured on a General Radio 1650-A Impedance Bridge. The two sets of coils M and M' were given exactly the same mutual inductance, and were connected oppositely. One coil of each set was a commercial radio choke; the other half was a 1.40 mH coil wound so as to minimize the distributed capacitance, which was 0.013 μF.

The variable inductance was a General Radio 107F Variable Inductance whose stator was tapped at 4 intermediate points. These connections plus the use of a vernier scale allowed changes of M to be read to 0.01 μH on an instrument whose largest M ≃ 90 μH. The other mutual inductances in the circuit could be used if 90 μH were insufficient to balance it. The output of the circuit was fed through a transformer to a Rohde & Schwartz Type UBM Tunable Amplifier.

In Fig. 6, we have a typical set of curves. We find the exact point of intersection by fitting each curve to a parabola (which it approximates near f_m) by least squares, on a log-log scale.

The method was checked by measuring the resistivity of pure In at 77 K and 293 K. The results were 1.795 and 7.75 μΩ-cm., respectively. The values given in Landolt-Bornstein are 1.72 and 8.19, respectively (34).

Results of the determination of ρ will be tabulated later.

Demagnetization Ratio

It was pointed out previously that the geometry of the sample plays a part in determining the relations between $4\pi M$, H and B. If the sample is in the form of an ellipsoid of revolution,

$$D = (e^{-2} - 1)\{(1/2e)\log \{(1 + e)/(1 - e)\} - 1\}, \qquad (3.9)$$

where D is the demagnetization coefficient, $e^2 = \{1 - (b^2/a^2)\}$, and a, b are the semi-major and semi-minor axes, respectively.

The shape of the sample is then characterized by D. For an infinite cylinder parallel to H, $D = 0$. For the present geometry (see Fig. 2a), $D = 0.02$. While the present geometry is not a perfect ellipsoid, it is sufficiently close for this approximation to hold.

Zoller and Dillinger (22) have shown that

$$H'_{c_1} = \{1 - (D/4\pi)\}H_{c_1}$$

$$H'_{c_2} = H_{c_2} \qquad (3.10)$$

where the primed quantities refer to the values of H_{c_1} and H_{c_2} corrected for the effect of $D \neq 0$. The relations will be used in following work.

Temperature Measurement and Control

The temperature of the helium bath was measured by means of a 2-way manometer. The tube M leading to the manometer is shown in Fig. 2b. One section of the manometer contained mercury, and the other butyl phthalate, a liquid which has a vapor pressure of less than 10 microns of Hg at room temperature. Since its density is 0.077 that of Hg, its use allows us to expand the temperature scale by a factor of 13. A four-way stopcock was used in the two-way manometer.

One end of the manometer was the above-mentioned tube in the inner dewar; the other end was pumped on by a Cenco vacuum pump, which

maintained a vacuum of a few microns. Thus the manometer was of the differential type. The difference in levels was read by a cathetometer to an accuracy of 0.05 mm.

The temperature of the helium bath (and thus the sample) was controlled by lowering the pressure above the bath by a large-capacity (110 cfm) Kinney vacuum pump. A means of controlling the pumping speed (and thus the temperature) was furnished by a Manostat Corp. No. 8 manostat, using the Cartesian diver principle. Pressure variations can easily be kept within $\pm$ 1 mm. oil during a run. This corresponds to a maximum temperature variation of $\pm$ 0.012 K at T $\simeq$ 1.1 K. In most cases, this range was held to $\pm$ 0.004 K or less.

The correspondence between pressure and temperature was made by means of the 1958 Helium Temperature Scale (23). The radius of the manometer tube was chosen sufficiently large to make the thermomolecular effect small. The greatest error due to this effect was 7 mK at the lowest temperature achieved ($\simeq$ 1.1 K) and decreased rapidly to zero as the temperature was raised.

The critical temperature was measured by applying a small field to the sample, decreasing the temperature very slowly, and noting the changes in galvanometer deflection as the sample is moved between the two coils. A typical example is shown in Fig. 7. The transition width was taken to be 80% of the change in deflection, as illustrated, and the critical temperature was taken as the midpoint of the transition width.

However, corrections must be made to this value to allow for the small magnetic field, which depresses T_c. If we assume that dilute al-
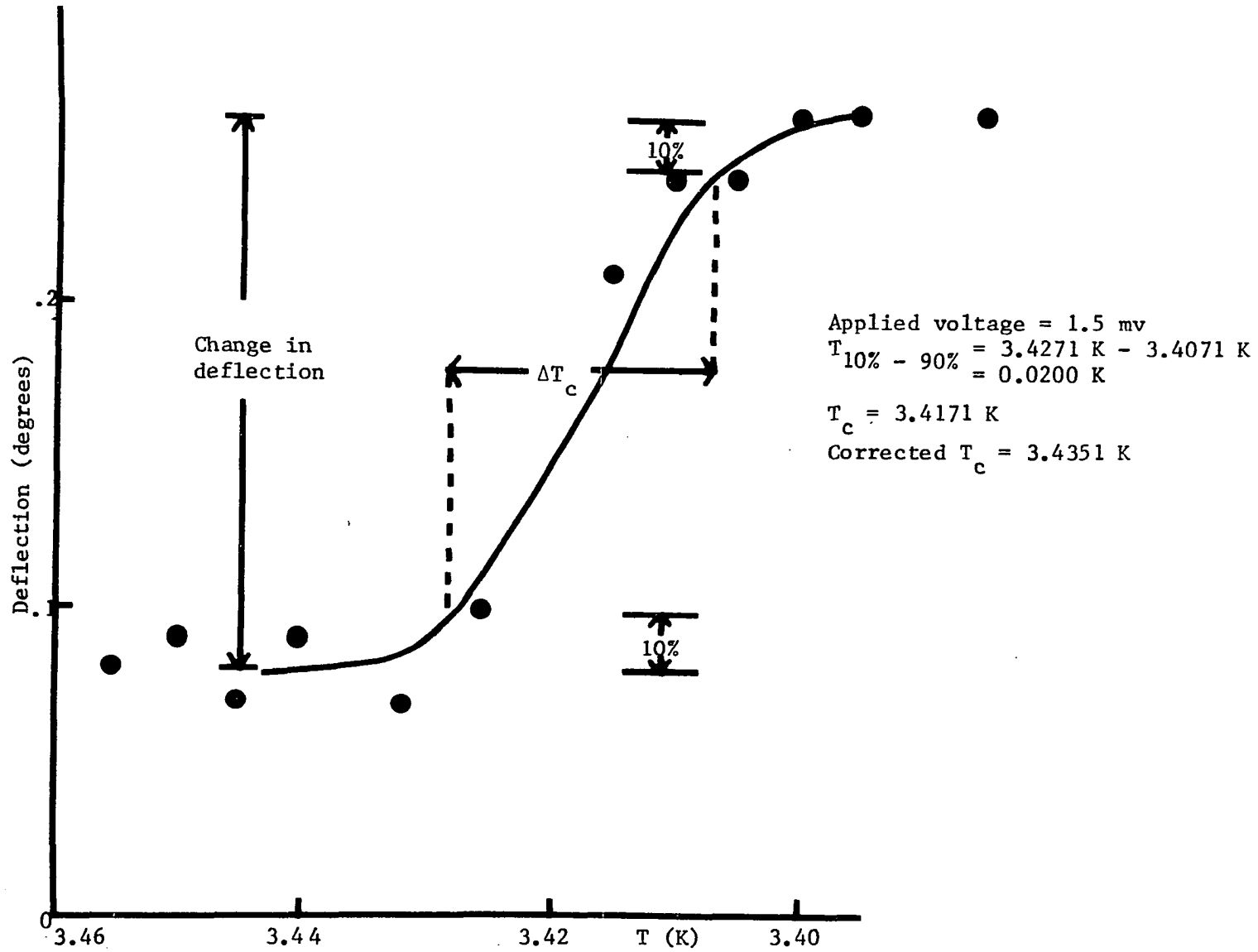
Fig. 7 Determination of the critical temperature T_c

loys of In have the same values of $(dH/dT)_{T=T_c}$ as pure In, we can use

the value 141 G/deg. K found by Shaw et al (24). Using Eq. (3.5) and

this value, we have

$$1 \text{ mV} \longleftrightarrow 12.0 \text{ mK} \tag{3.11}$$

Appropriate corrections (of the order of 18 mK) were made in all deter-

minations of the critical temperature.

To check the absolute accuracy of the temperature measurement sys-

tem, annealed samples of pure In were tested at 0.8 and 1.5 mV. Comp-

ared to Shaw's T_c = 3.4075 K, the temperatures were only 11 mK low. In

addition to this check, the levels of the oil and mercury sections were

tested frequently with vacuum on both ends to ensure that the levels

were the same.

Jarring of the Sample

One problem which occurs in the magnetization data is that of hys-

teresis. While a theoretical basis for treating this will be discussed

later, the situation can be somewhat alleviated by jarring the thrust

rod and thus the sample before each measurement. Since the hysteresis

is greatest around H= H_{c_1}, the greatest improvement in data is found in

this region. Dubeck et al (32) noted this effect in the Pb-In system

recently.

In practice, tapping and measurement alternate at a given field

until the deflection has decreased to a constant value. A typical

case is shown in Fig. 8. We see that the deflection (and the magnetiz-

ation) can be decreased up to 30% in some cases.

The physical basis for this effect is that the flux lines are pin-

ned at certain extended defects like dislocations, causing hysteresis.

Fig. 8. Typical Effect of Tapping

LEGEND: ○ -- sample tapped

● -- sample not tapped

Deflection (arbitrary units)

0   .02   .04   .06   .08

Applied voltage
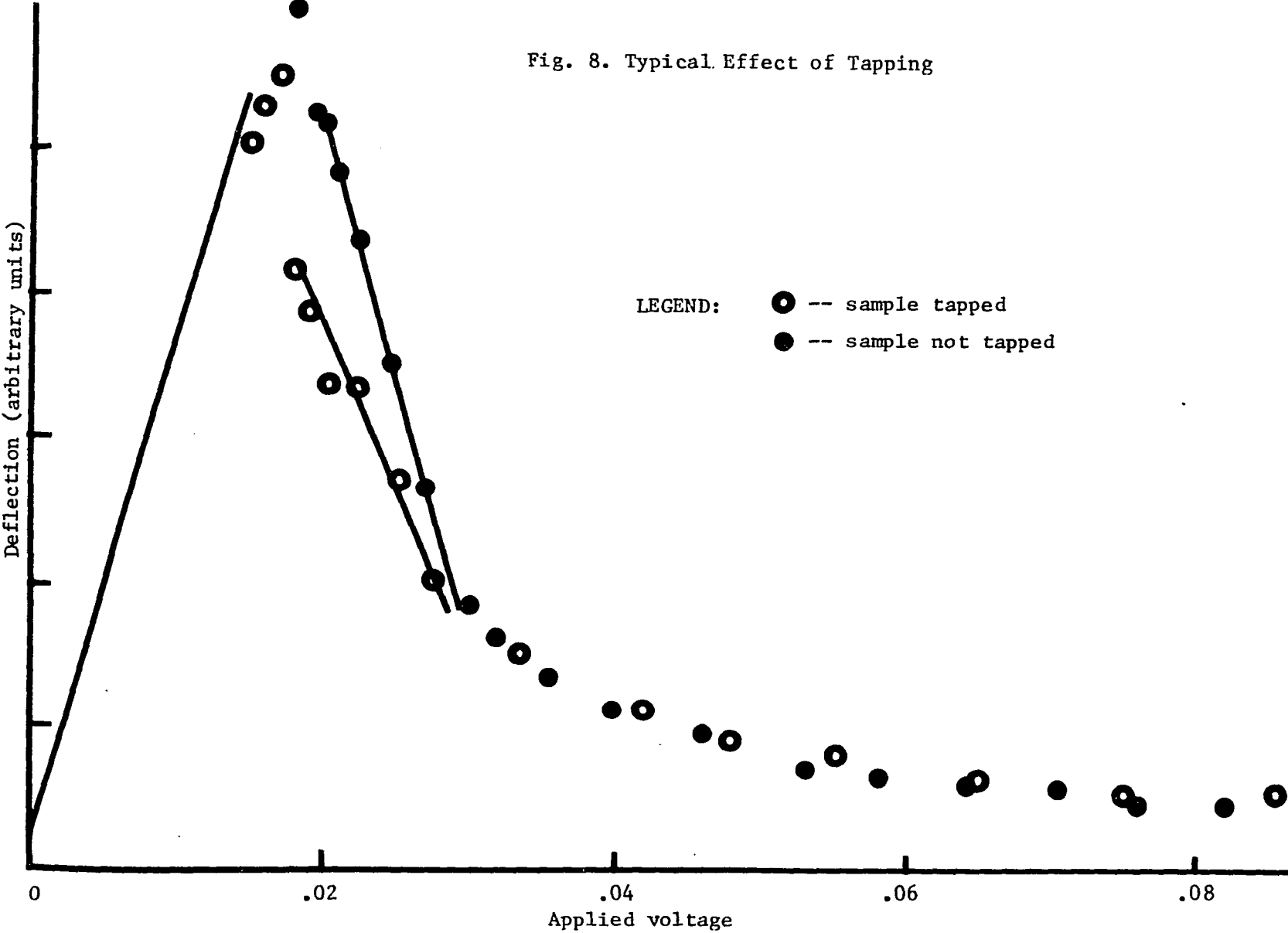
At a comparatively low magnetic field, the magnetic driving force is not sufficient to free them from their pins. The mechanical force of the jarring (or the thermal fluctuations caused thereby) is apparently sufficient to free many of the fluxoids, though not all. It might be useful in further work to study the correlation between the elimination of hysteresis and the frequency and amplitude of low-frequency vibrations applied to superconductors. This would give us more insight into the physical basis of hysteresis.

It is of interest to note that Goedemoed et al (33) achieved the same result by "wiggling" the magnetic field and the temperature.

CHAPTER IV

PRELIMINARY EXPERIMENTAL WORK

Prior to discussing the results of In-Cd alloys, we shall discuss some preliminary work which was done on the Sn-Ga and In-Ga systems. These systems were chosen for a number of reasons.

Firstly, Sn and In (both of which are superconductors) form solid solutions with a considerable number of other elements. The elements and the maximum solubility in atomic % are for Sn: Au, 0.2; Bi, 13.1; Cd, 1.1; Hg, 0.5; In, 12.5; Pb, 1.45; Sb, 10.3; Te, 0.1; Tl, 0.35; Zn, 2. For In: Bi, 12.4; Cd, 6; Ga, 18.3; Hg, 12; Li, 9; Pb, 12; Sn, 26.4; Tl, 23; Zn, 2. This data is taken from Hansen and Anderko (25). Since the solid solutions which are formed in these cases have a body-centered tetragonal crystal structure, no effort need be expended in determining this structure.

Secondly, a number of investigators have found that certain of these alloys form Type II superconductors, in contrast to the Type I behavior of pure Sn and In (26). It should be noted that while considerable work has been done on the variation of T_c with concentration for these solutions, less has been done on magnetic aspects.

While Hansen and Anderko showed no solubility of Ga in Sn, Predel (27) indicated a maximum solubility of 7.1 at. %. Their phase diagram

is shown in Fig. 9a. A number of samples were made from Ga and Sn

supplied from Electronic Space Products Inc.; both metals were claimed

to be 99.999% pure.

Because no samples were prepared near the region of possible Ga

precipitation (> 7 at. %), no annealing was done at first. A further

justification for this was that the samples were relatively non-hyst-

eretic, i.e., the trapped flux ratio was 20% or less. This ratio is

the proportion of magnetization at H = 0 on the return curve to the

maximum magnetization, at H = H$_{c_1}$. When annealing near the solidus tem-

perature was done, the trapped flux decreased by about half, but the

general shape of the forward magnetization curve remained the same.

These curves were of the Type I form, i.e., approximately triang-

ular. The magnetization had a slope of about 30 near H = H$_c$, indicat-

ing almost complete Type I behavior.

The reason why some alloys show Type II superconductivity, and

others Type I is still not known (14). In general, κ will increase

with residual resistivity (see Eq. (2.9)). If $\kappa \geq 0.707$, the supercon-

ductor is Type II. However, the residual resistivity has not been

measured for these particular alloys.

In Type I superconductors we have the relation

$$H/H_o = 1 - (T/T_c)^2 \qquad (4.1)$$

If we fit this to the present data, we can find the critical field

at T = 0 (H$_o$) and critical temperature T$_c$. Since only two sets of data

(at concentrations of 2.1 and 5.7 at. % Ga) were obtained, the results

are not reproduced here. However, in general the variation of T$_c$ agrees

with the data of Knapp and Merriam (28), i.e., a small increase of T$_c$
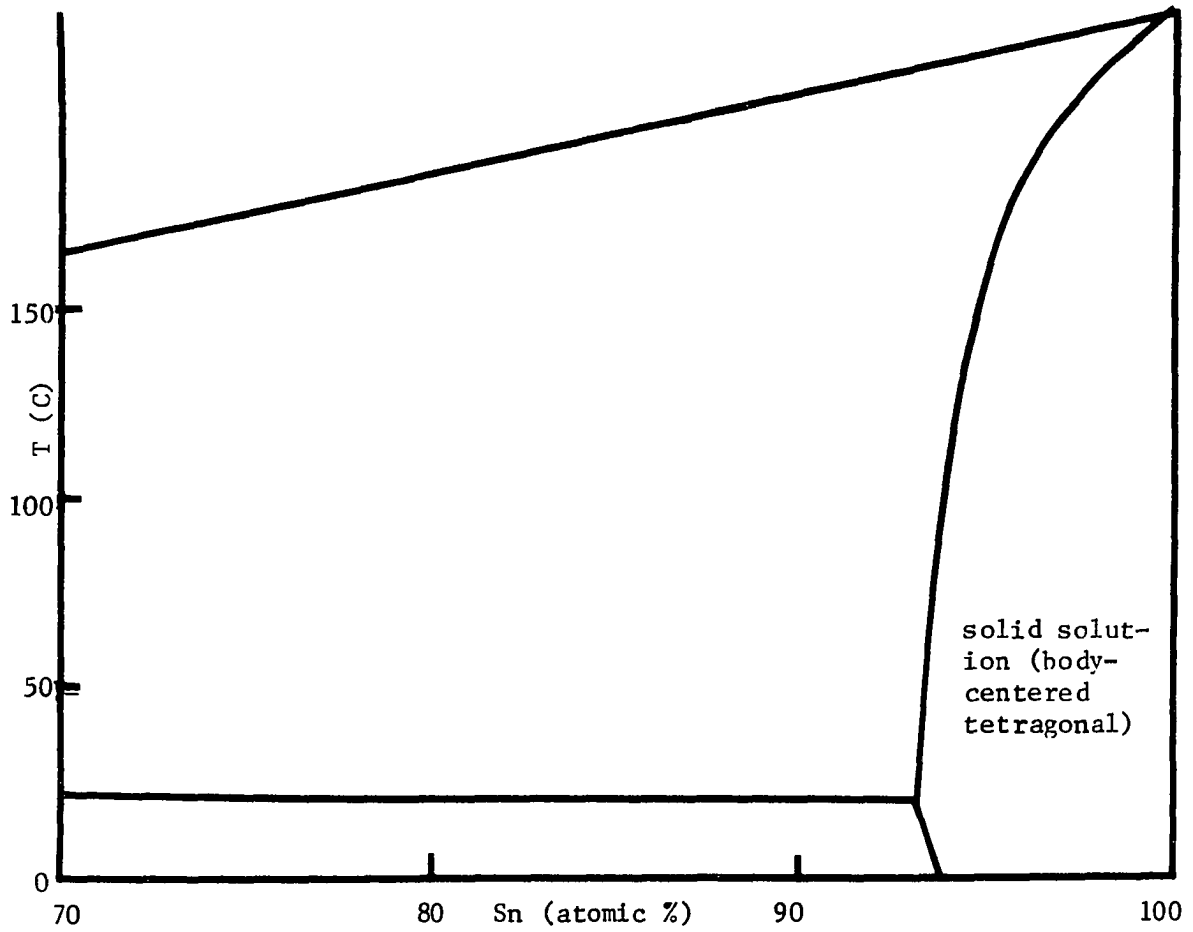
Fig. 9a. Phase diagram of Sn-Ga system
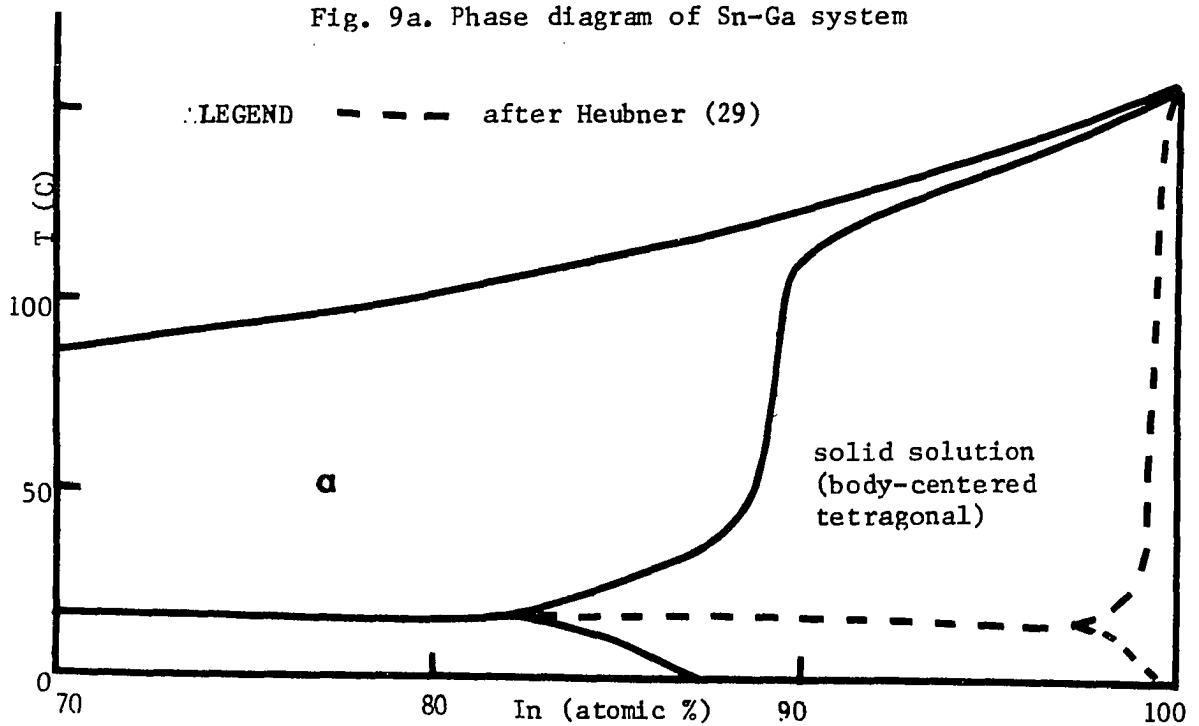
Fig. 9b. Phase diagram of In-Ga system

of a few tenths of a degree from that of pure Sn.

Since Type II superconductivity is found in 5 In alloys as compared to 3 Sn alloys, it was then decided to examine it in the In-Ga system. This system had not been checked experimentally prior to this work. The phase diagram in Hansen and Anderko (25) is shown in Fig. 9b. However, subsequently Heubner and Wincierz (29) determined a much smaller solid solubility in the In-rich end (about 1 at. % Ga at elevated temperatures, and about 2.5 at. % Ga at room temperature) by differential thermoanalysis. Since the samples were chosen on the basis of the Hansen data, they all have a Ga concentration of greater than 5 at. %.

In spite of this, all samples up to about 30 at. % Ga were Type I superconductors, as in the Ga-Sn system. Using the above procedures, we can find H_o and T_c. Results are shown in Fig. 10. As before, the samples were not annealed for long times.

Consider first the temperature data. For almost all solvents, T_c drops in a very dilute solid solution (< 1 at. %). This is due to the removal of energy gap anisotropy by alloying. However, little systematic analysis has been done for greater concentrations. For example, Fischer (26) found a slight decrease in T_c in the In-Tl system beyond the dilute range (in agreement with Merriam et al (35)) but a strong increase with the addition of Bi, Sn and Pb to In. In the In-Ga system, we see little variation of T_c with concentration of Ga. If the Ga had not really dissolved in In, this would provide an explanation, as we would be measuring the T_c of In.

Presumably some Ga is partially segregated in the alloys at the concentrations used.

Fig. 10. Critical Fields and Temperatures in In-Ga system
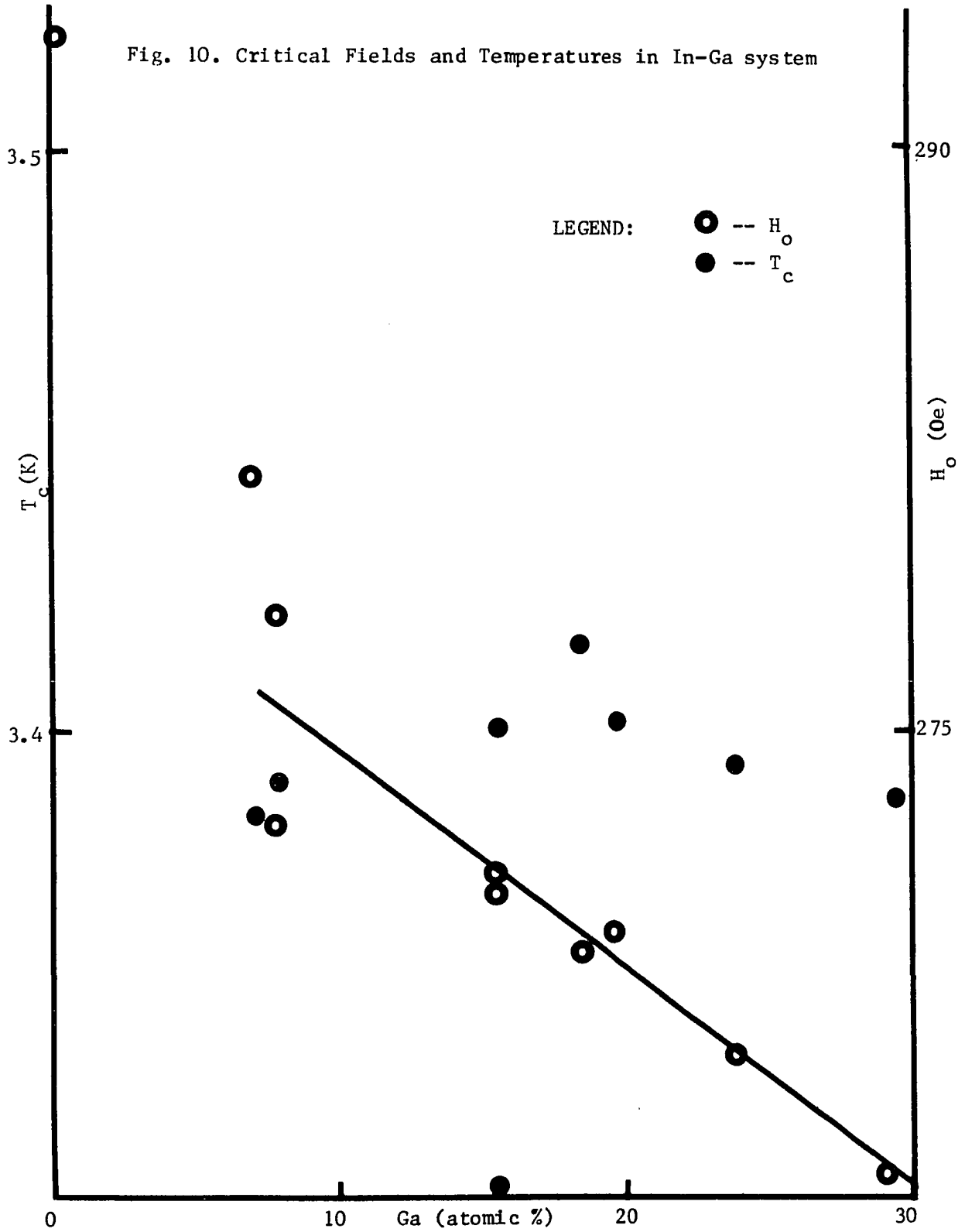
When concentrations of greater than 30 at. % Ga were used, the magnetization curves developed characteristics similar to those of Type II superconductors. However, the curves often had two maxima, indicating that the samples may have consisted of more than one phase. The final slopes of the curves were approximately 2, indicating at least partial Type II behavior. These broadened flux transitions were also noted by Chiou et al (31) in other In solid solutions. Because of the high trapped flux ratios found, work on these materials was not continued.

CHAPTER V

MAGNETIC HYSTERESIS IN TYPE II SUPERCONDUCTORS

The inter-relationships between H_{c_1}, H_{c_2}, H_c and the GL paramet-
ers κ are based on the assumption that the magnetization curve is rever-
sible, i.e., the magnetization curve of a superconducting specimen is
the same for external field H increasing or decreasing. Experimentally,
what is generally found is illustrated in Fig. 11a. The region of great-
est hysteresis is near $H = H_{c_1}$. The difference between the forward and
reverse curves gradually diminishes as $H \to H_{c_2}$, where the magnetization
for either the forward or reverse direction vanishes. However, the same
phenomenon is not generally observed as $H \to 0$. A remanent positive mag-
netization, or "trapped flux", is generally noted.

The preceding description of the hysteretic behavior of Type II
superconductors has been purposefully general, as the exact shape of the
curves will always be dependent on the composition of the superconductor,
its mechanical and metallurgical history (in terms of degree of cold
working, precipitates, dislocations, etc.), temperature and other variab-
les. The first problem which now confronts us is to determine whether a
reversible curve exists for each pair of irreversible curves -- a revers-
ible curve which will give values of H_{c_1}, H_{c_2} and H_c which will fit the
theory better than these quantities guessed from the irreversible forward
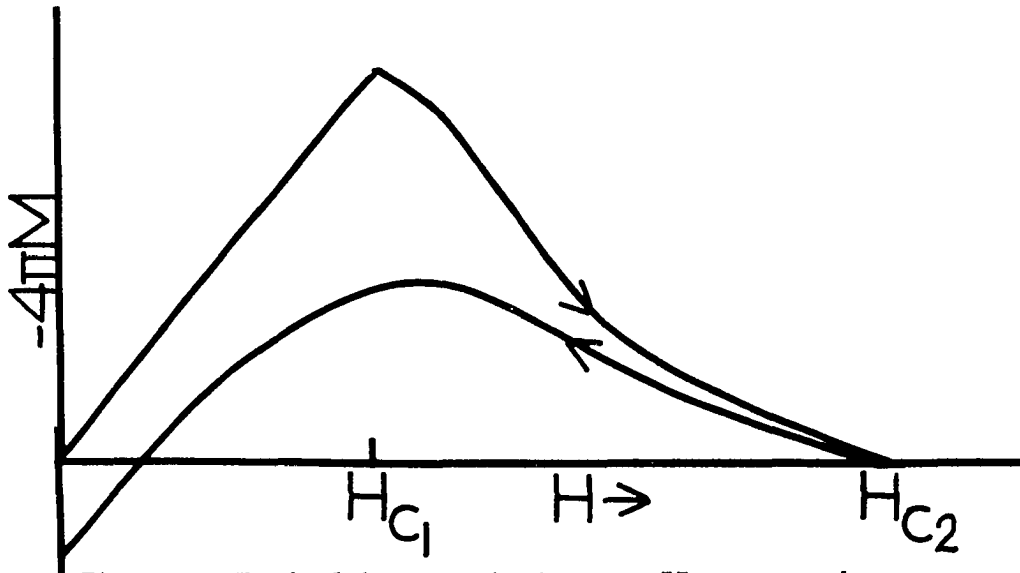
Fig. 11a. Typical hysteresis in Type II superconductors.
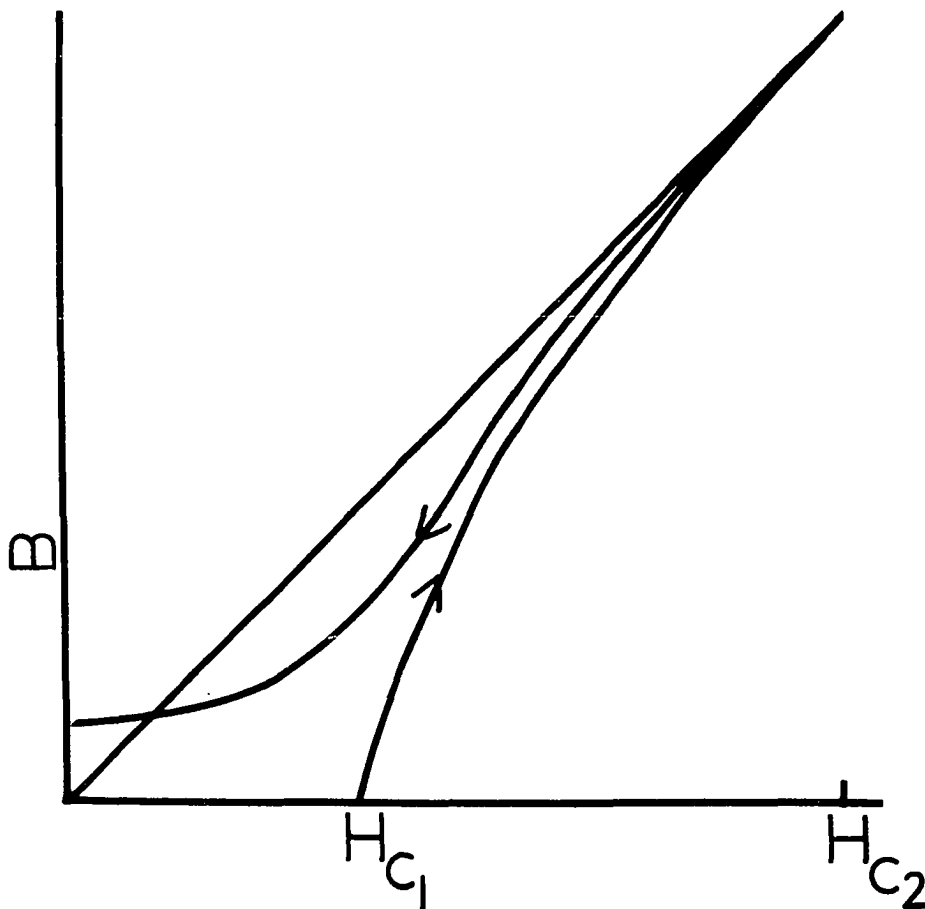
Fig. 11b. Magnetic flux as a function of applied field in Type II superconductors.

curve alone. The second problem is that of finding this reversible curve.

Dealing with the first problem, no theoretical basis presently exists to answer this question. However, a number of experimental studies have been made on this subject, the chief of which is Goedmoed's work on bundles of impure niobium wires. In this work, the field and/or the temperature was oscillated with an amplitude of about 100 Oe and/or 0.25 K, with the resultant magnetization falling between the forward and reverse magnetization curves. The authors suppose that this reversible curve is one of thermodynamic equilibrium (i.e., the true reversible curve) computed by Abrikosov (4). While there is no theoretical proof that these data are indeed the true reversible curve, there are a number of experimental considerations which lead to the conclusion that the curve found by Goedemoed et al (33) is a close approximation to it. We shall discuss their work in greater detail when a comparison with experiment of a hysteresis theory formulated in the present work is made.

The second problem, that of actually determining the reversible curve, is more difficult. Because of the physical nature of the fluxoid lattice in a Type II superconductor, drastic assumptions must be made in order to put the resulting equations in a tractable form. Abrikosov's (q.v.) classic paper derived the general form of the reversible curve for values of the Ginzburg-Landau parameter $\kappa \gg 1$. Furthermore, his work is based on the Ginsburg-Landau equations, which are, strictly speaking, defined only for temperatures close to T_c. However, in spite of these limitations we can compare the hysteresis theory in the present work with   Abrikosov's theory. For large values of κ, the derived curves are similar to those of Abrikosov.

It is useful to make a critical evaluation of the theories of

hysteresis in Type II superconductors which have been previously published.

This is done in the Appendix. The correlation of these theories and the

present one with Abrikosov's reversible curves will now be discussed.

A model for the reversible curve must be combined with a model for the

fluxoid-defect interaction in order to produce a set of hysteretic curves.

Presenting the Abrikosov reversible curves involves computation-

al difficulties. However, Koppe and Willebrand (KW) (38) devised an ap-

proximation to the Abrikosov theory by using the GL equations and bound-

ary conditions on the unit "cell" of a fluxoid (the derivatives of the

order parameter and magnetic field vanish). Reversible magnetization

curves were calculated using those conditions for different values of κ

and are shown in Fig. 12. However, a model of the fluxoid-defect inter-

action was not presented, so that hysteretic magnetization curves cannot

be computed.

The KW curves appear to agree with the Abrikosov theory for the

three regions of the latter's reversible magnetization curve for which

exact solutions can be found (36): $H \simeq H_{c_1}$, $H_{c_1} \ll H \ll H_{c_2}$, and $H \simeq H_{c_2}$.

These regions will now be discussed in detail.

Applied Field H near H_{c_2}

Here $4\pi M = (H - H_{c_2})/1.16(2\kappa_2^2 - 1)$ (5.1)

in the Abrikosov theory. The magnetization is thus linear near $H = H_{c_2}$.

Due to the linearity of the ad hoc reversible curves chosen in the

Campbell (37) and Silcox (39) models (discussed in the Appendix), both

models fulfill this criterion.
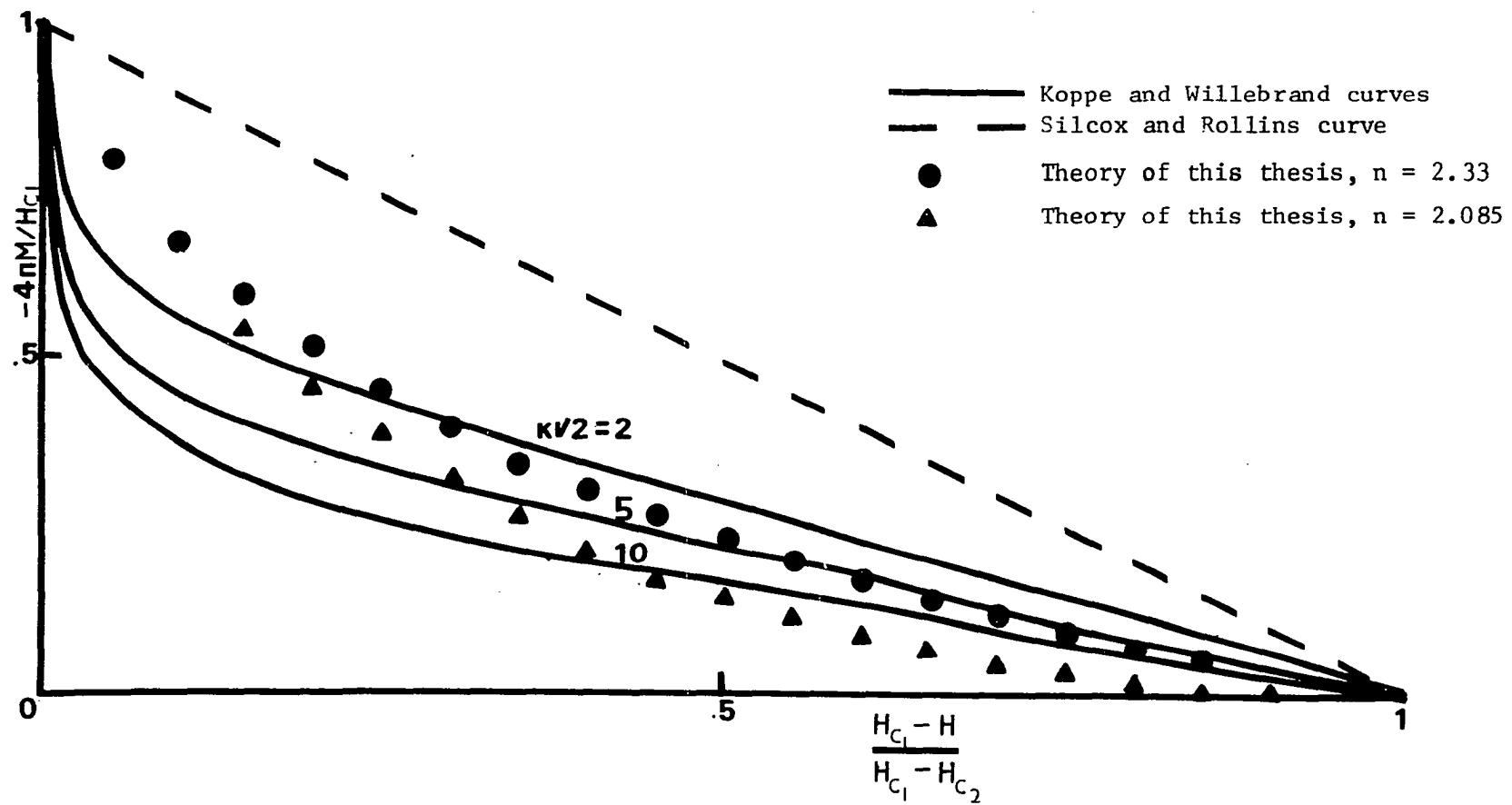
Fig. 12. Reversible magnetization curves of Koppe and Willebrand for different values of $\kappa\sqrt{2}$.

The Intermediate Region

Here $H_{c_1} \ll H \ll H_{c_2}$. This definition of the intermediate region is strictly applicable only to $\kappa \gtrsim 10$. For this region

$$4\pi M \propto \log (const./\sqrt{B}) \tag{5.2}$$

Since in the intermediate region $H \gg 4\pi M$,

$$4\pi M = K_1 \log (const./\sqrt{H + 4\pi M}) \simeq K_1 \log (const./\sqrt{H})$$

$$= K_2 - (K_1/2)\log H \tag{5.3}$$

where the K's are constants. The magnetization plotted versus the applied field on semi-logarithmic paper should produce a straight line.

Curves of the intermediate region for the Silcox and Campbell models are shown in Fig. 13. The parameters of each model were adjusted to produce $\kappa = 10$. κ was obtained from the equation

$$H_{c_2} = \sqrt{2}\kappa H_c \tag{5.4}$$

and H_c was obtained from the geometry of the reversible magnetization curves. Δ was arbitrarily chosen as 0.5 for the Campbell model; any other value would produce similar curves. The curves are normalized with respect to H_{c_1}, as shown. The reversible curves of the two models do not fall on a straight line on semi-logarithmic paper due to their linearity from $H_{c_1} < H < H_{c_2}$. The two models do not fulfill this criterion in the intermediate range, whereas the present theory obeys Eq. (5.3) over an appreciable range.

Applied Field H near H_{c_1}

Using Goodman's (40) expression for H in this region (derived from Abrikosov's exact expression),

$$H - H_{c_1} = \left(\frac{3\sqrt{2}\,\pi^2\,H_c}{4\kappa}\right)\left(\frac{H_c\,\sqrt{(2/3)}}{\pi\,\kappa(4\pi M + H)}\right)^{\frac{1}{4}} \exp - \left(\frac{4\pi H_c\,\sqrt{(2/3)}}{4\pi M + H}\right)^{\frac{1}{2}} \tag{5.5}$$
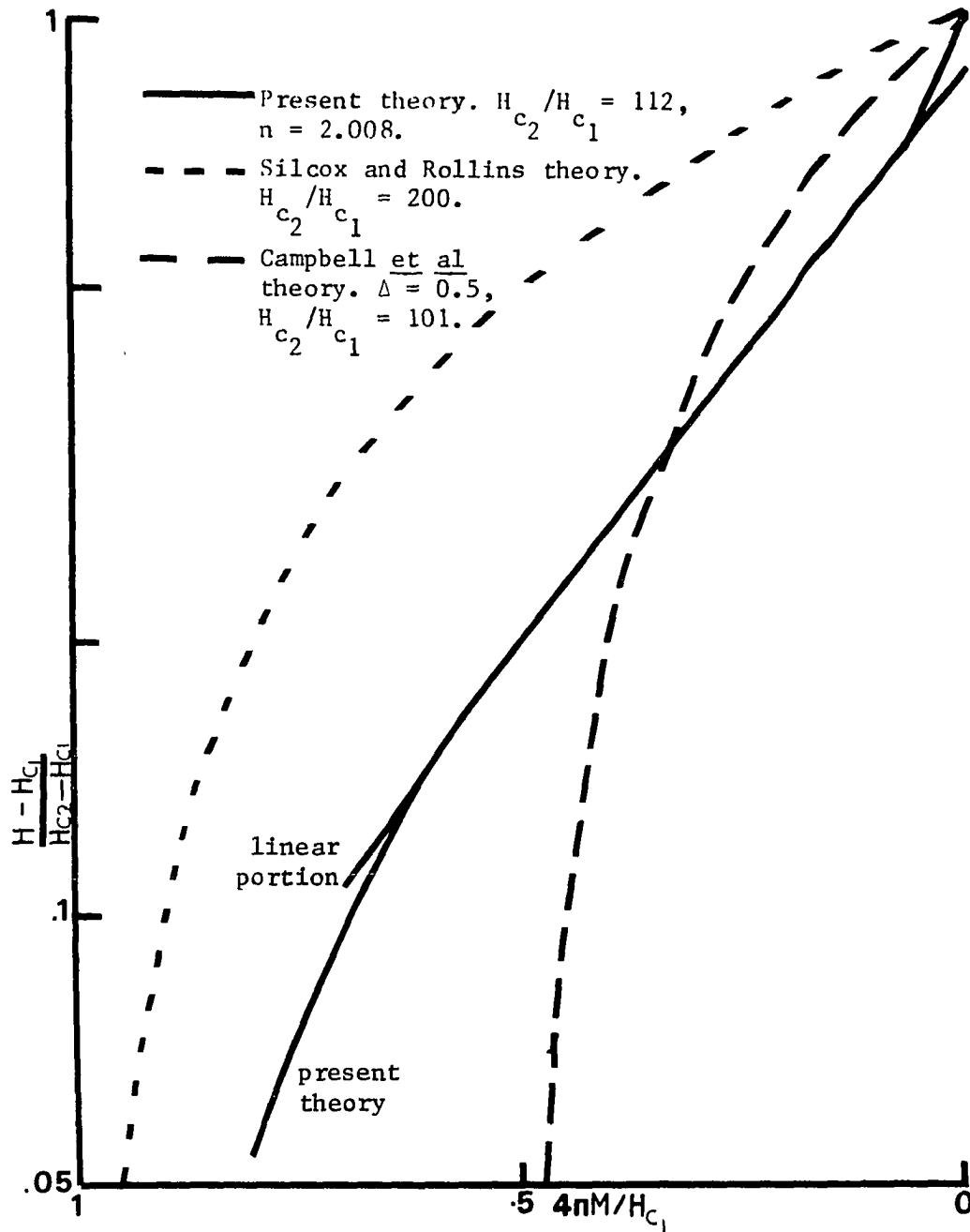
Fig. 13. Reversible magnetization curves for intermediate values of applied field. κ = 10.

The thermodynamic critical field H_c must still be specified. This may be done exactly by integrating Abrikosov's equations, which can only be done numerically. However, if we use the Harden and Arp (109) formula $\kappa = 0.717 \ (H_c/H_{c_1})^{1.68}$ with the condition $\kappa = 10$, $H_{c_1} \simeq 0.17 \ H_c$ is obtained. Substituting in Eq. (5.5),

$$H - 1 = 2.46(4\pi M + H)^{-\frac{1}{4}} \exp -\{6.05/(4\pi M + H)\}^{\frac{1}{2}} \quad (5.6)$$

where H and $4\pi M$ have been normalized with respect to H_{c_1}. The right hand side of Goodman's equation 4 (40) lacks a factor $\pi/2$, and this has been supplied in the above Eq. (5.5).

Eq. (5.6) has been plotted in Fig. 14. It possesses a vertical tangent at $H = H_{c_1}$, and decreases rapidly as H increases. The Silcox model is not at all similar to this curve. It decreases with a slope of 0.005 from its initial point. While the Campbell model bears some similarity, if another value of Δ had been chosen the inconsistencies with the Abrikosov theory might have been more apparent. Thus the Campbell model will not fit the Abrikosov curve closely unless the value of Δ is known in advance.

The Koppe curve of Fig. 12 is similar to the Abrikosov curve at $H \simeq H_{c_1}$, as expected.

In conclusion, we see that while the two models discussed meet the Abrikosov criterion for $H \simeq H_{c_2}$, they do not meet it in the other two regions of interest.

Present Theory

A theory has been devised which produces better agreement with experimental and theoretical work than those previously mentioned. In devising this theory, we needed (1) an irreversible magnetization curve
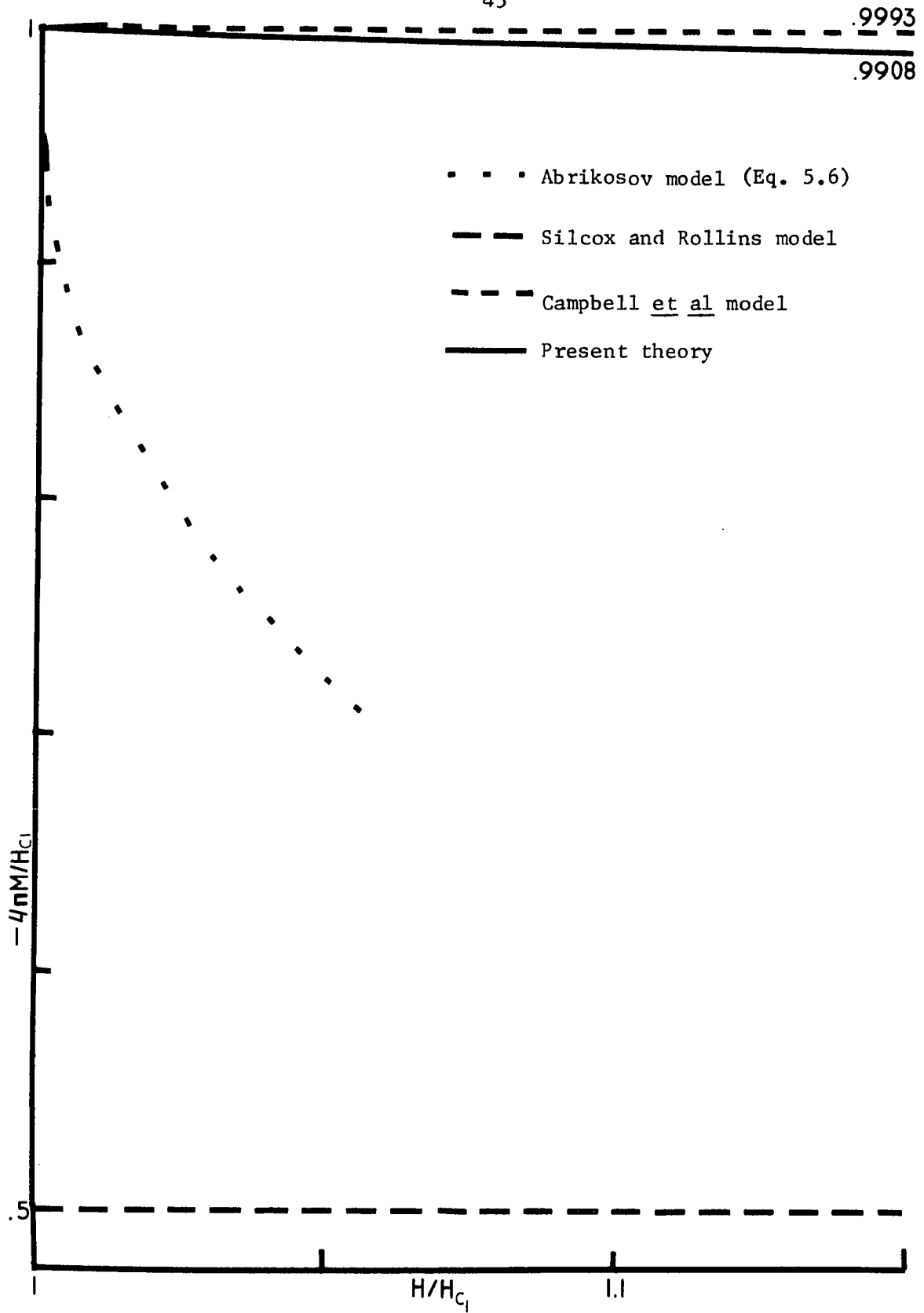
Fig. 14. Reversible magnetization curves for $H \approx H_{c_1}$. Same parameters as in Fig. 13 (κ = 10).

fitting data of both hard and Type II superconductors; (2) a revers-
ible magnetization curve which would (a) fit the three criteria mentioned
above, and (b) be derivable from the irreversible curve; (3) a theory
simple enough to be put into closed form.

The Silcox and Rollins approach (39) was used, with a major
modification, illustrated in Fig. 15.

Melville and Taylor (41) calculated the 'normalized' force
$-(a/F)(dF/da)$ between two fluxoids as a function of distance a/λ_L (where
λ_L is the London penetration depth) for both the Silcox and Rollins
and de Gennes (42) models. The Silcox and Rollins model deduces a force
relationship $F \propto a^{-3}$; the de Gennes model is $F \propto K_1(a)$, where K_1 is a
modified Bessel function of the first kind. The approximate range of
validity of each model is indicated by the solid lines. The distance
between fluxoids is a.

In a real superconductor, a form of the fluxoid-fluxoid inter-
action is needed which is valid over larger distances than the Silcox
and Rollins model, because contributions from next- and more distant
neighbors may be important in certain regions of the magnetization
curve, especially $H \simeq H_{c_2}$. The Silcox and Rollins model avoids this
problem by considering only nearest-neighbor interactions.

Given Fig. 15, a simple way of combining the two models would
be to take a rough average by drawing a straight line somewhere above
3 on the ordinate. Since fluxoids are presumably similar in all mater-
ials, the exact distance of this line above $-(a/F)(dF/da) = 3$ will be
governed by the type of superconductor under consideration.

Let us take $-(a/F)(dF/da) = K$, where $K \geq 3$. We shall see later
that theoretical considerations prevent the case $K < 3$. Integrating,
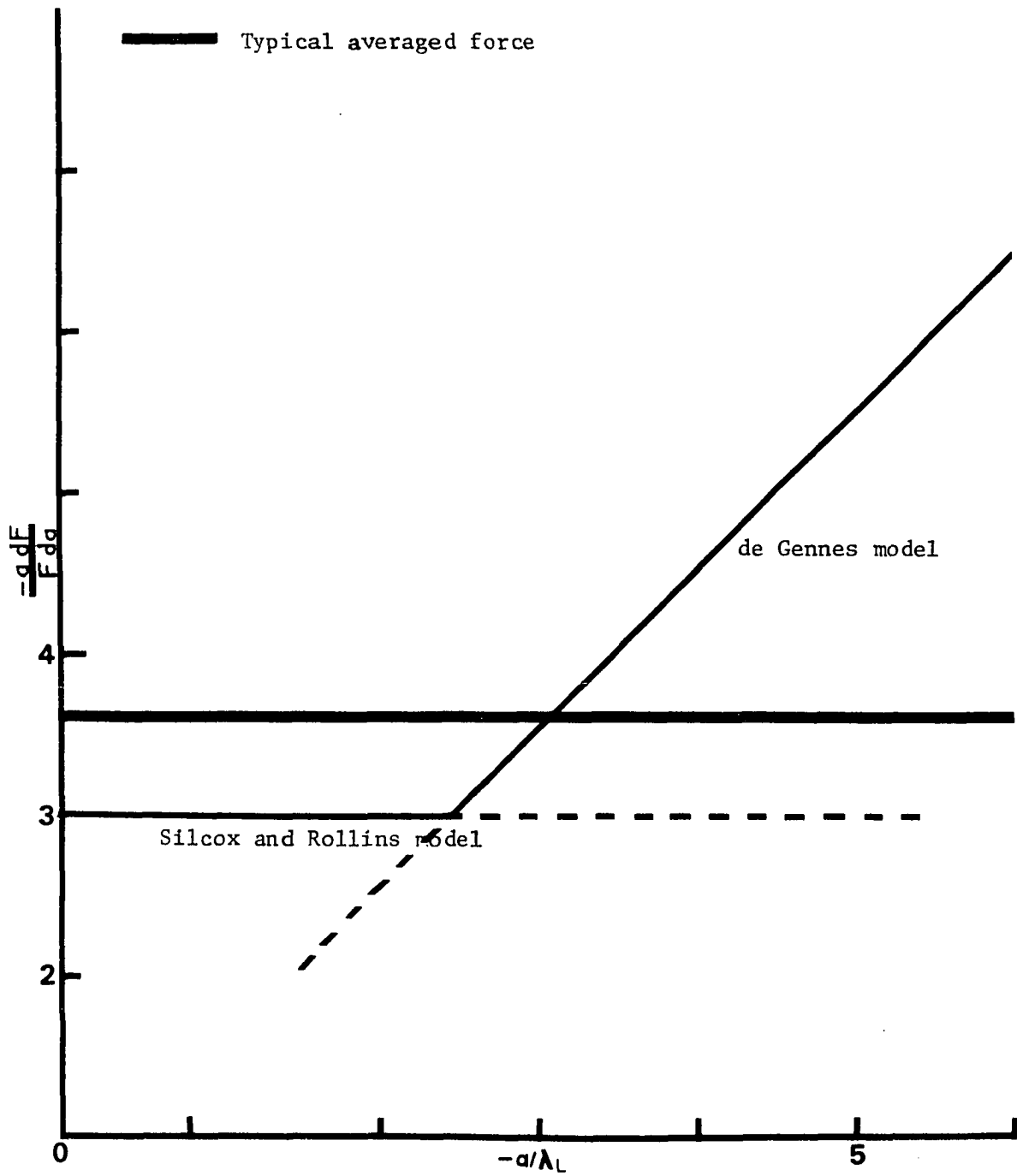
Fig. 15.(after Melville and Taylor). Normalized forces between fluxoids as a function of distance.

$$F = ca^{-K} \tag{5.7}$$

where c is a constant. Differentiating Eq. (5.7) to put it into the form of Eq. (A.49)(of the Appendix),

$$\frac{dF}{da} = -\frac{cK}{a^{K+1}} \tag{5.8}$$

If $K + 1 = 2n'$, we have $n' = 2$ in the Silcox model, and $n' \geq 2$ in the present model. The present model is developed along the lines of the Silcox model (outlined in the Appendix), except for the substitution $n' \rightarrow n$. In Eq. (A.50) the number of interacting fluxoids should probably be modified to > 6 in the present theory (since we are attempting to take account of larger numbers of interacting fluxoids), but this quantity in any case will be merged into a variable parameter. Substituting Eq. (5.8) into Eq. (A.51a),

$$da/dx = c_1 a^{2n'+1}$$

and

$$a^{-2n'} = c_2 x + c_3,$$

where the c's are constants, and x is the radial distance from the center of the superconducting cylinder. Using Eqs. (A.48) and (A.47),

$$B^{n'} = c_4 x + c_5 \tag{5.8a}$$

A reversible magnetization curve is now chosen. It can be selected so that it meets the three criteria noted above. Its choice is an _ad hoc_ assumption, of the same type as those of previous theories, and is independent of the procedure used to find Eq. (5.8a). The choice is

$$B = H_{c_2} \left(\frac{H - H_{c_1}}{H_{c_2} - H_{c_1}} \right)^{1/(n' - 1)} \tag{5.9}$$

The Silcox reversible curve was postulated to be $B = H_{c_2} \cdot \dfrac{H - H_{c_1}}{H_{c_2} - H_{c_1}}$, i.e., the two models are equivalent if $n' = 2$.

Before proceeding to discuss pinning effects, let us analyze the theory in light of the three criteria mentioned above.

$$H \text{ near } H_{c_2}$$

Using Eqs. (A.1) and (5.9), dropping primes, and letting $H_{c_2} = p$ and $H_{c_1} = 1$ for simplicity,

$$4\pi M = p\{(H - 1)/(p - 1)\}^{1/(n-1)} - H \qquad (5.10)$$

As $H \to p$, write $(H - 1)/(p - 1) = 1 - x$, where x is small. Then

$$4\pi M = p\left\{1 - \frac{x}{n-1} + \frac{1}{n-1}\left[\frac{1}{n-1} - 1\right](x^2/2) + \ldots\right\} - H$$

$$= (p - H)\left(1 - \{p/(n-1)(p-1)\}\right)$$

$$+ \frac{p(2-n)(p-H)^2}{2(n-1)^2(p-1)^2} + \ldots \qquad (5.11)$$

For $4\pi M$ to be linear in $p - H$, the quadratic term in $p - H$ (as well as higher order terms) must be negligible with respect to the linear term. The ratio of the quadratic to the linear term is

$$\frac{p(2-n)(p-H)}{2(n-1)(p-1)\{(n-1)(p-1) - p\}} \qquad (5.11a)$$

Let us investigate how close to H_{c_2} H has to be for the quadratic term to be negligible. We can define linearity as occurring if the ratio (Eq. 5.11a)) ≤ 0.1. While it is difficult to formulate a general rule linking n, p, and H, let us choose $p = 3$ for example. Then for $n = 2.1$, 2.2, and 2.3, the values of H at which linearity begins is 1.83, 2.52, and 2.77, respectively. To use a larger value of p, we may take Goedemoed's (33) data, for which is found $n = 2.08$ and $p = 7.6$. Linearity takes place at $H \geq 6.5$.

In general, there exist well-defined regions of linearity at $H \simeq H_{c_2}$. The first criterion is then satisfied.

$$H_{c_1} \ll H \ll H_{c_2}$$

While we cannot prove in general that the magnetization obeys

Eq. (5.3), a typical result is shown in Fig. 13. The parameters of the

reversible curve have been adjusted to yield $\kappa = 10$. The area under the

magnetization curve was found by using Eqs. (A.1a) and (5.9), yielding

$$|A| = -(p^2/2) + \{(n - 1)/n\}p(p - 1), \tag{5.12}$$

after taking into account the area of $-\frac{1}{2}$ for $0 < H < H_{c_1}$. The value of

κ was then determined from Eq. (5.4). We see that the slope is linear

over 60% of the magnetization curve, which puts the present theory in

agreement with Abrikosov's theory for this region.

$$H \simeq H_{c_1}$$

Calculations using the present theory for this region are shown

in Fig. 14, with the same parameters as in Fig. 13. We do not have agree-

ment with the vertical tangent at $H = H_{c_1}$, and the slope is considerab-

ly smaller than that of the Abrikosov theory. However, due to the slope

of the present theory being 12 and 24 times as great as the Silcox and

Campbell theories in this region, respectively, we may say that at least it

is in no greater disagreement with Abrikosov's work than the other two.

We see in Fig. 12 we get reasonably good agreement with Koppe's results

for various values of κ, i.e., the comparatively small initial slope of

the present theory tends to "catch up" with the Abrikosov-Koppe curves

as H is increased.

Now let us take account of the pinning effects in the theory.

The force F_p between a fluxoid and a pore pinning center varies as (45)

$$F_p \propto (H_{c_1}\phi_0/4\pi)\log(a/\xi_0) \tag{5.13}$$

where ξ_0 is the radius of the core of the fluxoid. The concept of a pore, a hollow sphere, is used because of the difficulty in discussing extended imperfections like dislocation networks.

Since the logarithm term in Eq. (5.13) varies slowly and is of the order of 1, Silcox writes the last equation as $F_p = H_{c_1}\phi_0/4\pi$. We shall do the same, because of the difficulty in integrating $\dfrac{da}{a^{2n+1}\log(a/\xi_0)}$.

Furthermore, other assumptions and approximations which have to be made about the pinning tend to render negligible the error in setting $\log(a/\xi_0) \simeq 1$. We assume, as Silcox does, a density of pinning strength ρ of the form $n\rho = P'$, where P' is a constant.

When $x = R$, the radius of the superconducting cylinder, B is given by Eq. (5.9). Substituting in Eq. (5.8a), and combining constants into β,

$$B = \{p^n\{(H-1)/(p-1)\}^{n/(n-1)} - \beta(R-x)\}^{1/n} \tag{5.14}$$

Substituting this in Eq. (A.1) and noting that $B = 0$ when

$$Q \equiv p\{(H-1)/(p-1)\}^{1/(n-1)} = \beta R^{1/n}, \tag{5.15}$$

$$4\pi M = -H + \{2nQ^{n+1}/(\beta R)^2(n+1)\}\{\beta R - (nQ^n/(2n+1))\},$$

$$0 \le Q \le \beta R^{1/n} \tag{5.16}$$

$$4\pi M = -H + \frac{2n}{(\beta R)^2(n+1)(2n+1)}\{Q^{n+1}\{\beta R(2n+1) - nQ^n\} + n(Q^n - R)^{(2n+1)/n}\},$$

$$\beta R^{1/n} \le Q \le p \tag{5.17}$$

In the reverse direction, the pinning force constant $\beta R \rightarrow -\beta R$, yielding

$$4\pi M = -H + \frac{2n}{(\beta R)^2(n+1)(2n+1)}\{n(Q^n+\beta R)^{(2n+1)/n} - Q^{n+1}\{\beta R(2n+1) + nQ^n\}\},$$

$$0 \le Q \le p \tag{5.18}$$

Graphs of these last equations for typical values of βR and n are

presented in Fig. 16. We will see that the plots of B and $4\pi M$ are fairly similar to those of Campbell and Silcox; B decreases in a roughly parabolic manner, and $4\pi M$ shows resemblance to experimental data. The prime difference lies in the shape of the reversible magnetization curve.

We are now in a position to compare all three models to an interesting set of experimental data compiled by Goedemoed (33). The magnetization curves, presented in Figs. 17 and 18, were obtained from bundles of impure Nb wire. The experimental aspects were discussed above. The GL parameter κ_1 (computed from Eq. (5.4)) is 2.37 (1.83) for the reversible (irreversible) curve; κ_2 (computed from Eq. (5.1)) is 2.43 (1.99) for the reversible (irreversible) curve.

In order to make the comparisons physically reasonable and not merely an exercise in curve fitting, we must impose some constraints. The major constraint imposed was that the slope of the reversible magnetization curve for each model be the same as that of the experimental data at $H \simeq H_{c_2}$. To a good approximation, this slope can be found by taking the average of the forward and reverse irreversible slopes, which are seldom very different. Thus the reversible slope at $H \simeq H_{c_2}$ is not needed for this determination. Goedemoed's experimental value of $H_{c_2} = 2500$ was taken as fixed in all calculations. Although these are not the only constraints which might be taken, they are physically reasonable. In general, we do not know the reversible curve for a given pair of irreversible curves. Our objective in comparing the theories is to vary their parameters to produce the best least-squares fit with the experimental irreversible curves. Theoretical reversible curves (a function of these parameters) will then be calculated and compared to the experimental reversible curve. As mentioned above, H_{c_2} and dM/dH at $H \rightarrow H_{c_2}$ are

53
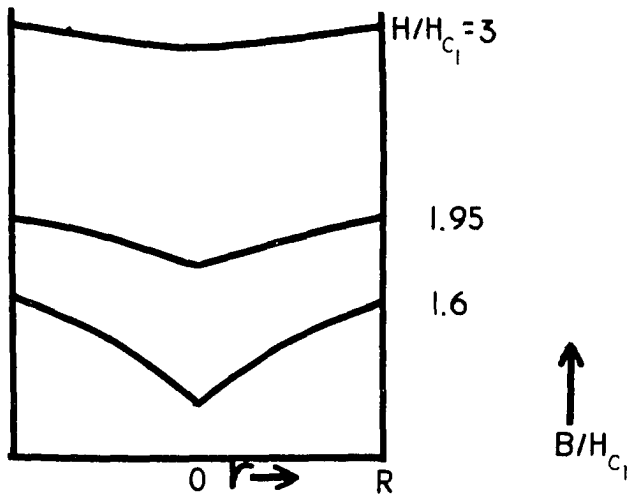
Fig. 16a. Plot of local
fields in present model
for increasing magnetic
field. $\beta R = 1$, $n = 2.2$
$H_{c_2}/H_{c_1} = 4$.
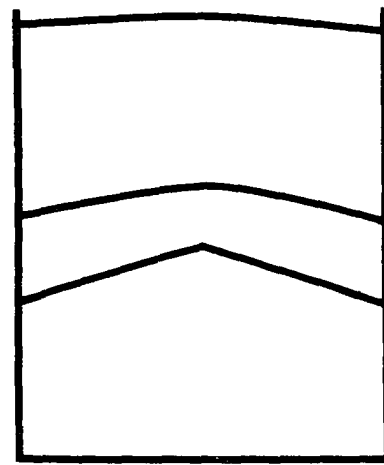
Fig. 16b. Plot of local
fields for decreasing
field. $\beta R = 1$, $n = 2.2$,
$H_{c_2}/H_{c_1} = 4$.
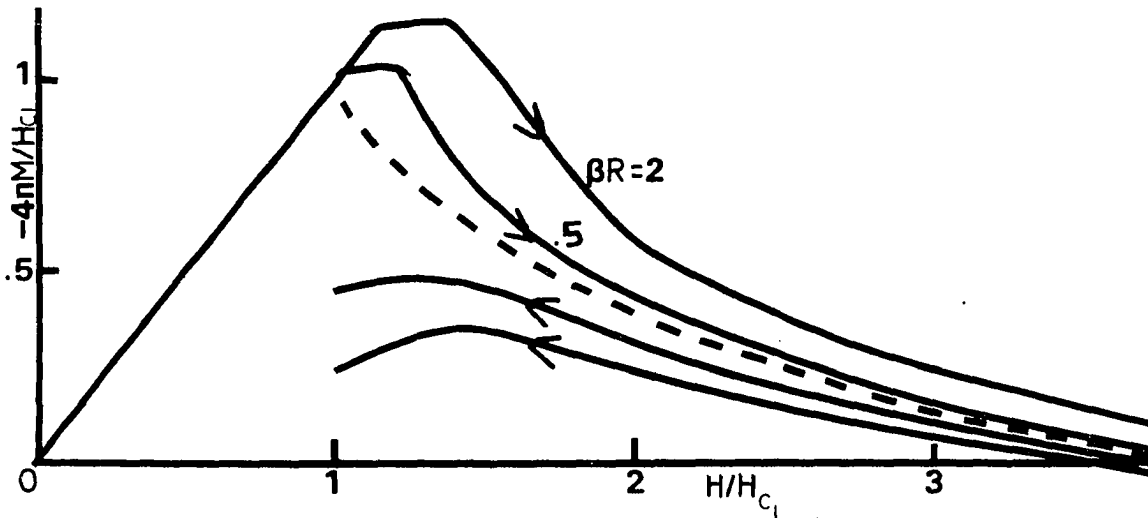
Fig. 16c. Magnetization as a function of applied field for present
model. $n = 2.2$, $H_{c_2}/H_{c_1} = 4$.

fixed.

In all models, the interval $H_{c_2} - H_{c_1}$ was divided into 27 points. The value of the parameters in each theory was found by minimizing the squares of the deviations of the theoretical points (both forward and reverse) from the 54 experimental points. For purposes of this computation, the quantity H_{c_1} was also treated as a variable parameter.

Results are shown in Fig. 17 and in Table 1. Because of the fixed quantities, the Silcox model yields H_{c_1} = 180 Oe, considerably different from the experimental value of 420 Oe. The deviations from the irreversible curves are also large, as seen in Fig. 18; the theoretical maximum of magnetization is only about 75% of the experimental value.

In the Campbell model, we can vary H_{c_1} as well as Δ and αR to produce the minimum deviation. However, the results are almost exactly the same as in the Silcox model. We have H_{c_1} = 210 Oe, which is 50% of the experimental value. The theoretical irreversible curves follow the Silcox model closely, and produce a least-squares deviation similar to it.

The present theory yields H_{c_1} = 330 Oe, considerably closer to the experimental value. In addition, the least squares deviation is an order of magnitude smaller than those of the other two theories, indicating much greater agreement with experimental data. Also, the values of H_c in both the reversible and irreversible computation is closer to the experimental data than the other two theories. Furthermore, the value of the magnetization in the present theory when $H = H_{c_2}$ is smallest. All three theories have a finite magnetization at this point, contrary to experiment.

We may reconsider the magnetization curves from a slightly different viewpoint. Suppose the value of H_{c_1} is known (420 Oe) and fixed.
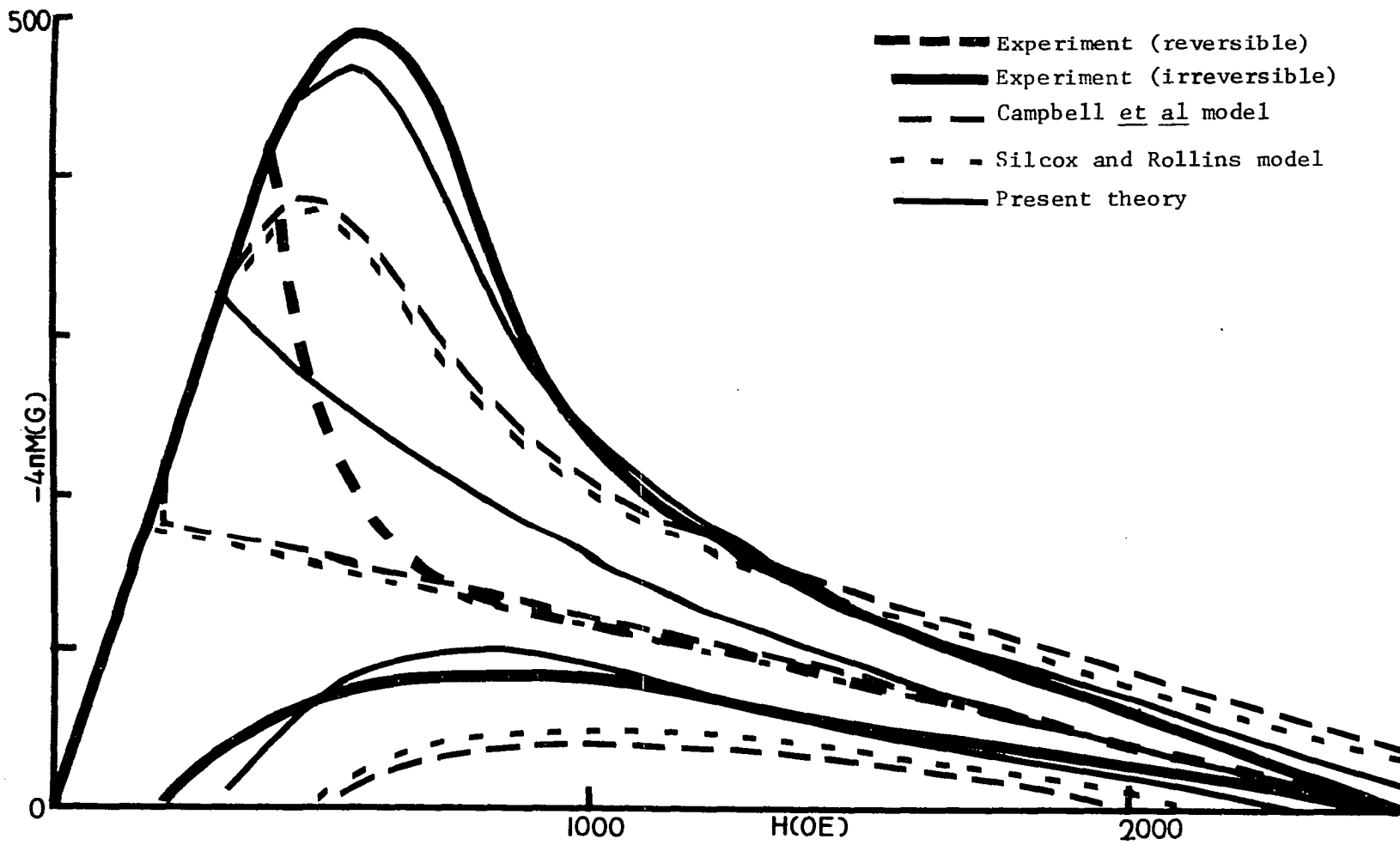
Fig. 17. Comparison of hysteresis models with experimental data. H_{c_2} and $\frac{dM}{dH}\Big|_{H_{c_2}}$ fixed.

TABLE 1

COMPARISON OF HYSTERESIS MODELS WITH EXPERIMENTAL DATA. H_{c_2} AND

$(dM/dH)_{rev.}$ AT $H \rightarrow H_{c_2}$ FIXED

	Experimental Data	Campbell Model	Silcox Model	Present Theory
Parameters	−	$\Delta = 0.14$ $\alpha R = 8.7$	$\beta R = 12.1$	$\beta R = 3.8$ $n = 2.08$
Sum of Squares of Deviations $(10^4\ G^2)$	−	15.9	15.4	1.43
H_{c_1} (Reversible)(Oe)	420	210	180	330
H_c (Reversible)(Oe)	745	680	675	778
H_c (Irreversible)(Oe)	968	940	935	977
$-4\pi M$ at $H = H_{c_2}$ (Irreversible) (G)	0	30	28	20

Then we may add this fixed point to the previous work and recompute the irreversible curves by the least squares method. The results are shown in Fig. 18 and Table 2.

Since the Silcox model will yield H_{c_1} = 180 Oe with the present data, its curves were not recomputed. However, the Campbell and present theory had the value H_{c_1} = 420 Oe substituted along with the previous fixed quantities. In Fig. 18, the reverse curve of the Campbell model lies entirely below the abscissa and is not shown. For clarity, neither reversible curve is shown.

As before, the present theory produces irreversible curves close to the data. We see from Table 2 that the sum of the deviations is about .15 that of the Campbell model. The value of H_c (irreversible) is closer to experiment, and the "residual" magnetization at $H = H_{c_2}$ is fairly small.

The results of these computations indicate that the present theory of hysteresis apparently can be fitted to experimental data to a good degree.

A question may arise at this point concerning the sensitivity of the present theory to the value of the pinning parameter βR. Any theory whose results change drastically with a parameter change tends to be suspect. As Table 3 bears out, this is not the case in the present theory.

One objection which might be raised against the present theory is its increased complexity. However, if we return to first principles, as Koppe (38) did, we find even greater complexity in the calculation of the reversible curve. Thus in order to bring about agreement with experimental data we must make some physical assumptions, which have been done.

Because of this increased complexity, it may appear, at first, more
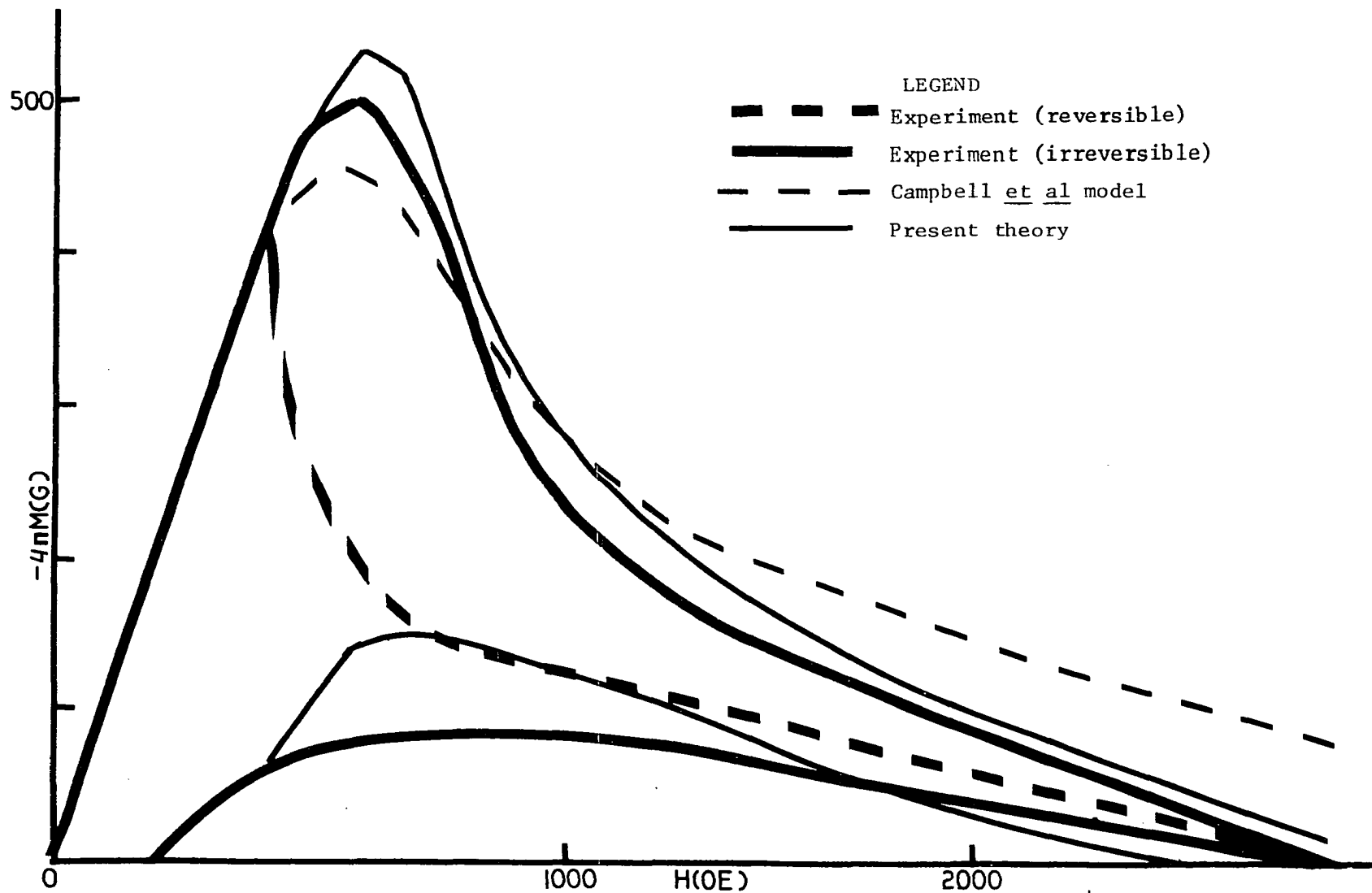
Fig. 18. Comparison of hysteresis models with experimental data. H_{c_1}, H_{c_2} and $\left.\frac{dM}{dH}\right|_{H_{c_2}}$ fixed.

TABLE 2

COMPARISON OF HYSTERESIS MODELS WITH EXPERIMENTAL DATA. H_{c_1}, H_{c_2} AND

$(dM/dH)_{rev.}$ AT $H \to H_{c_2}$ FIXED

	Experimental Data	Campbell Model	Present Theory
Parameters	-	$\Delta = 0.62$ $\alpha R = 2.6$	$n = 2.13$ $\beta R = 2.4$
H_c(Irreversible)(Oe)	968	1040	1015
Sum of Squares of Deviations (10^4 G^2)	-	34.6	4.8
$-4\pi M$ at $H = H_{c_2}$ (Irreversible)(G)	0	80	20

TABLE 3

VARIATION OF SUM OF LEAST SQUARES DEVIATIONS WITH PARAMETER βR IN
PRESENT THEORY

Sum of Least Squares Deviations (Arbitrary Units)	βR
0.1456	3.80
.1451	3.82
.1443	3.84
.1431	3.86
.1437	3.88

difficult to correlate theory with experiment. However, the addition of simple physical rules allows calculation of the relevant parameters easily.

Let us take the slope s of the reversible magnetization curve near H_{c_2} to be approximately midway between those of the two irreversible curves. Differentiating Eq. (5.10),

$$s = \{p/(p - 1)(n - 1)\}\{(H - 1)/(p - 1)\}^{\{(2-n)/(n-1)\}} - 1$$

(5.19)

As deduced from the discussion following Eq. (5.11a), if $H \gtrsim 0.9p$ the slope of the magnetization will be close to linear. If we set $H = 0.9p$ in the above equation, we obtain a relationship between s (experimentally derivable), p and n, shown in Fig. 19. We thus have a relationship between p and n.

To obtain βR, we see from Eq. (5.18) that on the reverse magnetization curve,

$$4\pi M_{reverse} = \{2n^2/(n + 1)(2n + 1)\}(\beta R)^{1/n} - 1$$

when $H = H_{c_1}$, due to the fact that $Q = 0$ at that point. We can use this equation to find βR, assuming that n has been found. The information is shown in Fig. 20. The magnetization is not very sensitive to n, and βR can be easily estimated to within about 10%, sufficient for most purposes.

While it would be useful to compare proposed internal field distributions with theory, comparatively little has been published on this subject to date. de Botton and Merenda (43) showed these distributions for Nb-Zr alloys; they were fairly similar to those in Figs. A.5, A.6, and 16. However, only a limited amount of data was shown and no extensive correlation of theory with experiment is possible. Cline et al (44) also
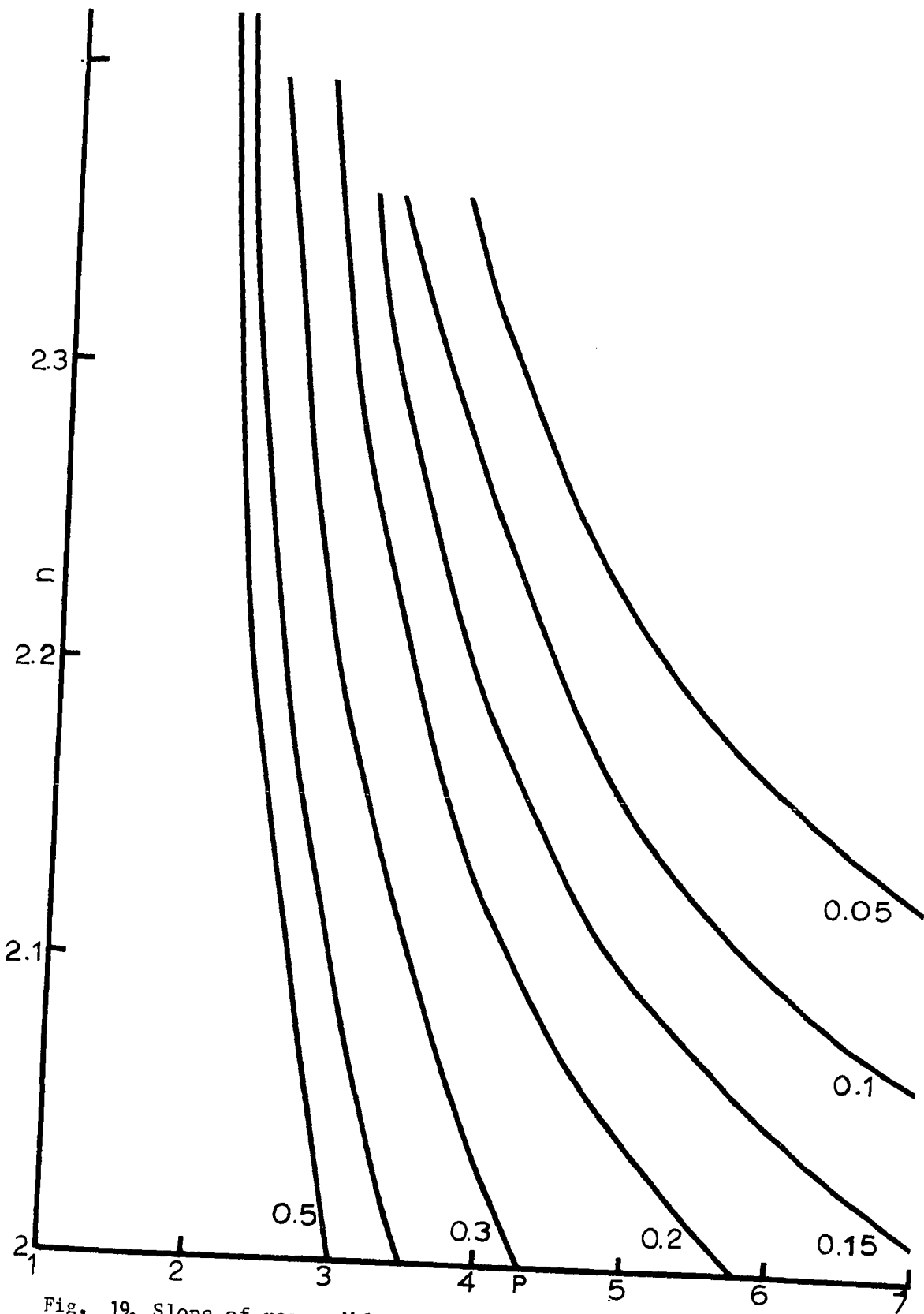
Fig. 19. Slope of reversible curve of magnetization as a function of n and p. The value of the slope at H ≃ .9p is listed beside each curve.
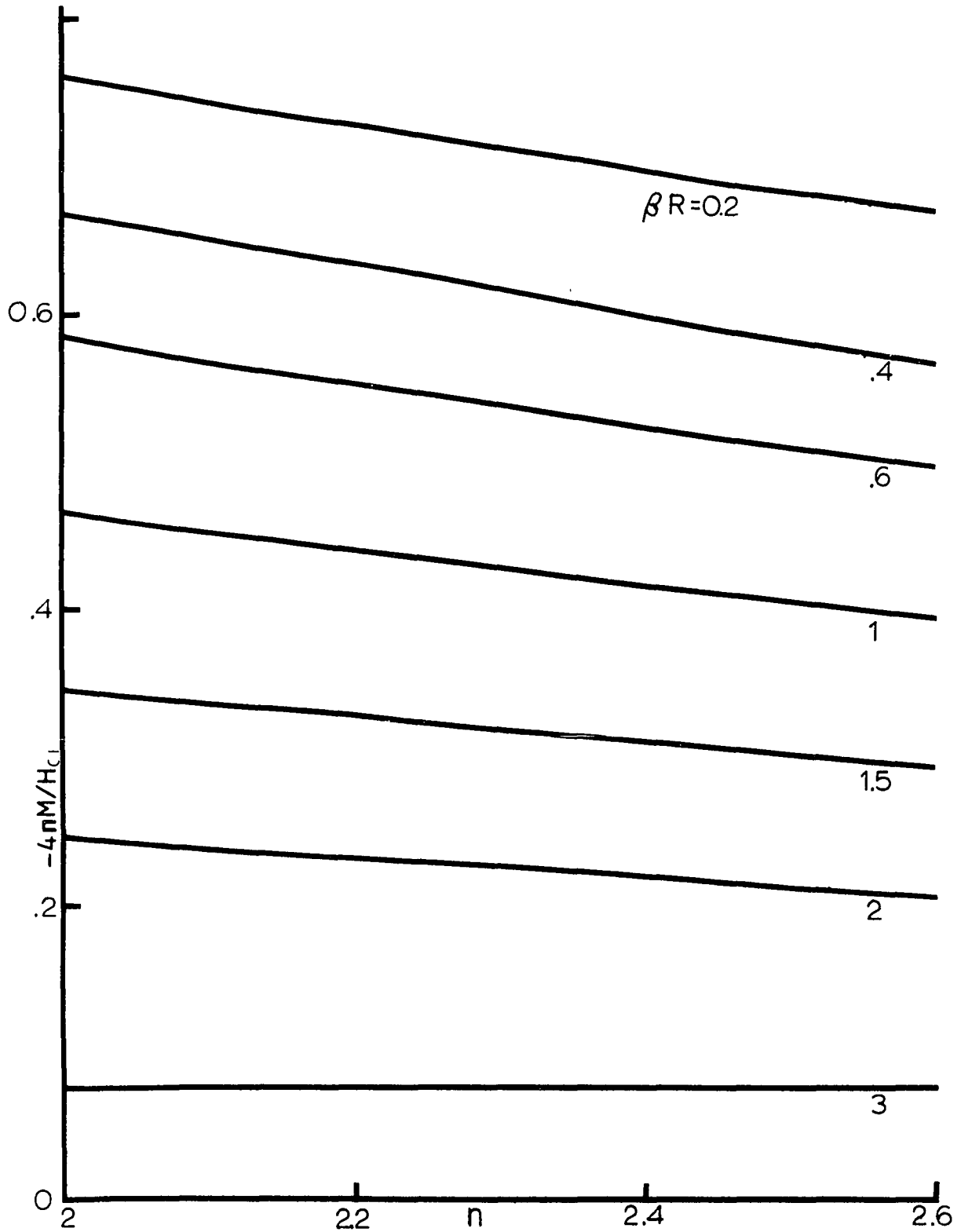
Fig. 20. Magnetization at $H = H_{c_1}$ on reverse curve as a function of βR and n.

presented some data on Nb samples.

The following problems still address themselves to the present theory: (1) The region below $H = H_{c_1}$ on the reverse curve must be described. This may be done in conjunction with the experimental data. (2) The parameter n should be characterized in terms of microscopic quantities. We may obtain n in terms of the GL parameter κ and H_{c_2}/H_{c_1} (=p) simply. We take advantage of the fact that Eqs. (5.1) and (5.19) are applicable as $H \rightarrow H_{c_2}$. For simplicity, let $H = p$ (i.e., $H = H_{c_2}$) in Eq. (5.19). This will change the value of s, the slope, only slightly. If we differentiate Eq. (5.1) with respect to H and equate the slopes,

$$1 - \frac{1}{(n-1)(p-1)} = \frac{1}{1.16(2\kappa^2 - 1)}$$

and

$$\frac{1}{n-1} = \{(H_{c_2}/H_{c_1}) - 1\}\{1 - \{1/1.16(2\kappa^2 - 1)\}\}$$

The determination of κ in terms of microscopic metallurgical quantities has been achieved only to a limited extent. The problem for n should prove equally difficult.

Summary

We have reviewed the most promising extant theories of hysteretic magnetization curves in the light of experimental data. A new theory has been presented which agrees closely with the data.

CHAPTER VI

RESULTS AND DISCUSSION: PRIMARY SUPERCONDUCTING PROPERTIES

In order to discuss the results in a meaningful manner, we shall group the experimental data into sections. Livingston and Schadler (14) grouped the properties of superconductors into 3 sections: primary, secondary, and tertiary. Primary properties were supposedly structure-insensitive, like T_c and H_o. These are related to the Debye temperature θ_D (through Eq. (2.2) and the relation $\hbar\omega_D/2\pi \simeq k\theta_D$), γ, and the electron-electron interaction parameter V. However, as has been noted, the hysteretic behavior of the sample will govern the value of H_o, since the apparent value of H_o must be adjusted for hysteretic effects.

Livingston and Schadler placed hysteretic effects in the tertiary category, as being sensitive to inhomogeneities. These will also alter values of H_{c_1}, which along with H_{c_2} has been placed in the secondary category as showing sensitivity to the electron mean free path ℓ.

To avoid, in this chapter, the problems of this categorization, we shall discuss first those properties which are non-hysteretic, like T_c and ρ_n, the residual resistivity. We shall then take account of the hysteresis in finding H_o. In the next chapter, we shall consider what Livingston and Schadler take to be the secondary superconducting properties.

Fermi Surface and Metallurgical Effects

Prior to discussing the actual experimental results, consider some aspects of the physics of these alloys as determined by other investigators. Although the Fermi surface for In approximates a sphere, it is close to the Brillouin zone faces in certain directions. When electrons are added (or subtracted, for Cd alloys), the result is usually changes in the degree of contact or overlapping with these zone boundaries. It has been shown (59) that the effects of Fermi surface-Brillouin zone interactions can bring about changes in the lattice parameters and lattice structure. The effect has been studied exhaustively in the dilute In-Cd system (67), but only up to the tetragonal-cubic transformation, i.e., about 5 at. % Cd. The Fermi surface of In has not been explored for higher concentrations of Cd, the concentrations in which we are interested.

Higgins and Kaehn (60) state that pure In is intermediate between the weak-coupling superconductors, for which the BCS model is used, and the strong-coupling superconductors (like Pb and Hg), for which the theory breaks down. The effect of this assertion will be seen in later discussion of data.

While no microscopic examination of the alloys was done, the small segregation coefficient of In alloys guarantees their uniformity when they solidify (66) in the single phase regions.

Debye Temperature θ_D

Because the interaction responsible for superconductivity is electron-phonon, the Debye temperature θ_D enters into calculations through an interaction cut-off at an average phonon energy $\hbar\omega_D/2\pi \simeq k\theta_D$ (see Eq. (2.2)).

Phillips et al (61) found θ_D =(110.1 - 2/at. % Cd) K for up to 5

at. % Cd. Their value for pure In is in agreement with the accepted value

of 111.3 K. However, this work does not cover the present region of

interest (> 5 at. % Cd). The rate of change of the Debye temperature with

concentration may be estimated by using the Lindemann melting rule (62).

This rule is based on the calculation of the rms displacement of

each atom from its equilibrium site as a function of θ_D and as a frac-

tion of the radius cell. A solid will melt when this fraction attains a

standard value. The Debye temperature may thus be written as a function

of melting temperature and atomic radius, and is

$$\theta_D \propto T_m^{\frac{1}{2}} W^{-5/6} D^{1/3} , \qquad (6.1)$$

where T_m is the (solidus) melting temperature, W is the mean atomic

weight, and D is the density.

If we use the concentration-solidus temperature gradient from

Fig. 3, and Eqs. (3.1) and (3.2),

$$\theta_D \simeq 111(1 - 1.24 \times 10^{-5} A),$$

where the proportionality constant has been chosen to agree with the

correct value of pure In. This constant will change little with phase

(119). Variable A is the atomic percent Cd. This result indicates that

$(d\theta_D/dA) \simeq 0.0014$, in contrast with the value of 0.02 found by Phillips

et al. Since we do not have data on our region of interest, we shall

compromise the difference by writing

$$\theta_D = 110 - 1/at. \% Cd, \qquad 0 < A < 0.16 \qquad (6.2)$$

In any case, since the value of θ_D enters logarithmically into

finding N(0)V in Eq. (2.2), a small error in its estimation should be

negligible.

Residual Resistivity

The residual resistivity ρ_n as found by the inductance method is shown in Fig. 21 and tabulated in Table 4. In the former are shown values found by Fischer (26). Although the latter's data yields resistivities somewhat higher, this may be due to the fact that apparently a 4-point resistive technique was used and, as has been pointed out, inductive superconductivity measurements are often more reliable (63). Furthermore the samples in Fischer's work were agitated for only a few minutes, with the resultant possibility of inhomogeneities. This might account for the higher resistivities found. The typical magnetization curves shown in Fischer's article indicate a higher hysteresis than in the present work, and thus greater inhomogeneity.

The resistivity at 77 K was also measured. In general, the results follow le Chatelier's rule: the resistivity varies linearly with concentration in a solid solution (64). It may also be noted that the resistivity drops sharply in the 15.95 at. % Cd. samples; this is most likely due to more than one component being present in the alloy, as this composition closely approaches the solvus line (see Fig. 3).

The electronic mean free path ℓ can be found from the resistivity. For any material, the term $\rho_n \ell$ is a constant independent of temperature, for low temperatures (65). Since this quantity has not been determined for our alloys, we use that of pure In. $\rho_n \ell$ can be measured by the anomalous skin effect. However, the results in the literature differ with each other by a factor of up to 2. Dheer (65) found that

$$1/\rho_n \ell = (18.0 \pm 1.1) \times 10^{10} \ \Omega^{-1} \ cm^{-2}. \text{ Thus}$$

$$1/\ell \quad = (18.0 \pm 1.1) \times 10^{10} \ \Omega^{-1} \ cm^{-2} \ \rho_n. \quad (6.3)$$
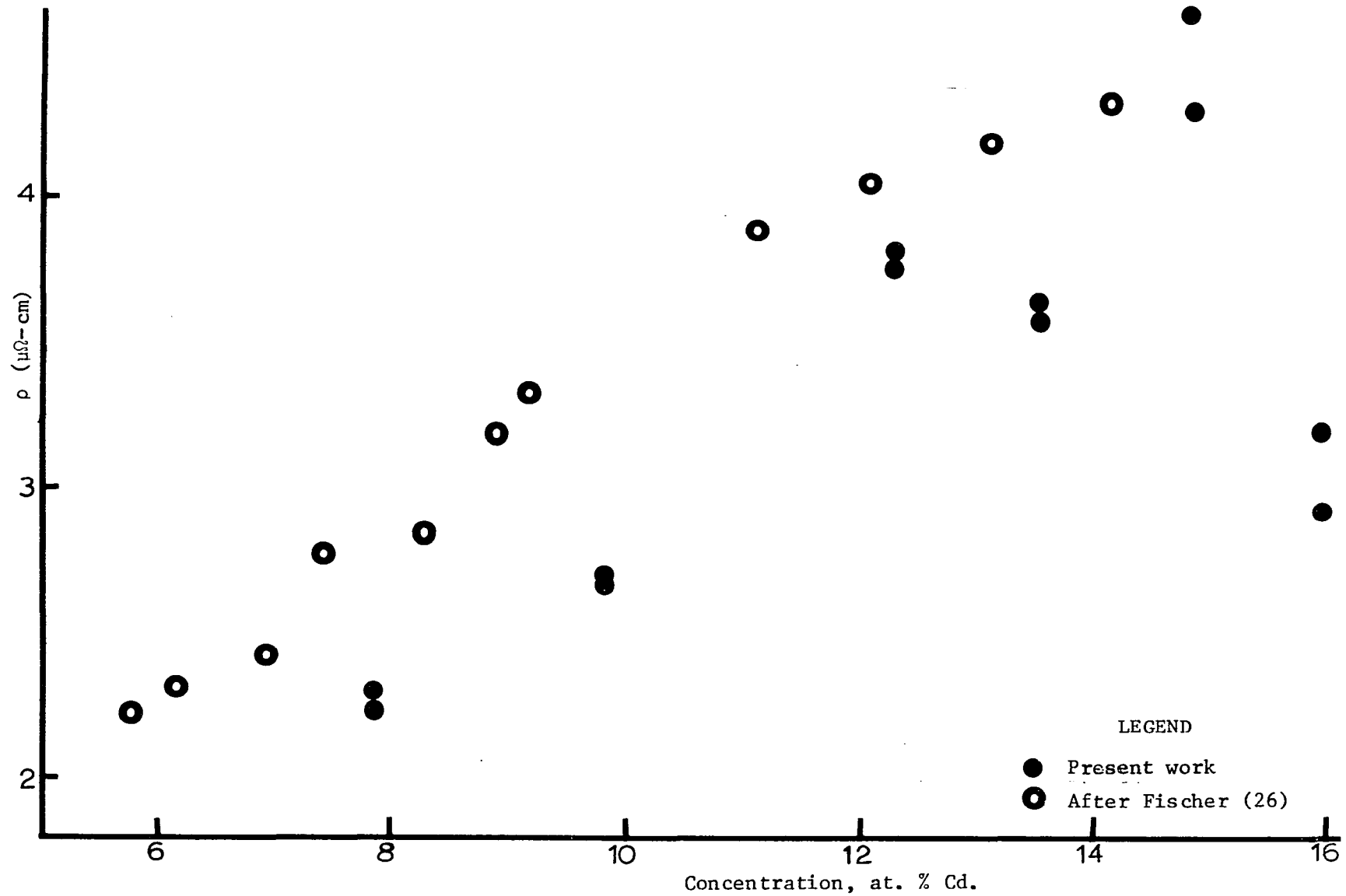
Fig. 21. Residual resistivity in In-Cd alloys

TABLE 4

SUPERCONDUCTIVITY IN THE IN-CD SYSTEM: PREPARATION OF SAMPLES AND PRIMARY PROPERTIES

Sample No.	Concentration (at. % Cd)	Annealing time (days)	Rotation time (min.)	ρ_n (4.2 K) ($\mu\Omega$-cm)	ρ_n (77 K) ($\mu\Omega$-cm)	ℓ (4.2 K) (Eq. 6.3) (Angstrom)	T_c (K)
99*$_{7.8}$	7.84	33	80	2.31	4.56	241	3.4839
103$_{7.8}$	7.83	27	80	2.24	4.13	249	3.4964
94$_{9.8}$	9.81	47	60	2.66	4.45	209	3.2216
102$_{9.8}$	9.81	26	70	2.66	4.37	209	3.1880
91$_{12.3}$	12.27	17	60	3.75	5.29	148	2.8724
97$_{12.3}$	12.25	21	60	3.79	6.34	147	2.9184
100$_{13.5}$	13.49	33	90	3.61	5.10	154	2.8988
101$_{13.5}$	13.48	32	90	3.58	5.57	155	2.9434
104$_{14.7}$	14.74	21	60	4.60	6.49	121	2.9938
107$_{14.7}$	14.74	29	60	4.29	6.44	130	2.9926
BJ7$_{16.0}$	15.95	16	90	2.95	5.59	189	2.907
BJ8$_{16.0}$	15.95	5.5	150	3.22	5.57	173	2.887

* -- Subscripts on this and subsequent tables indicate Cd concentration in atomic percent.

TABLE 5

SUPERCONDUCTIVITY IN THE IN-CD SYSTEM: THERMODYNAMIC CRITICAL FIELD

Sample No.	ΔT_c (K)	θ_D (K)	N(0)V	λ (after McMillan)	H_o (irreversible) (Oe)	D_o (irrev.)	Number of points
$99_{7.8}$	0.0207	102.2	0.285	0.796	295.2 ± 3.4	$+0.0200 \pm 0.0094$	6
$103_{7.8}$	.0163	102.2	.285	.797	284.8 ± 4.7	$+ .0477 \pm .0137$	6
$94_{9.8}$	.0333	100.2	.281	.774	231.2 ± 3.2	$- .0627 \pm .0117$	4
$102_{9.8}$	.0060	100.2	.280	.745	251.1 ± 5.8	$- .0347 \pm .0200$	6
$91_{12.3}$	.0170	97.7	.274	.741	251.5 ± 8.0	$- .0756 \pm .0274$	5
$97_{12.3}$	.0605	97.7	.275	.752	257.5 ± 2.5	$- .0241 \pm .0080$	5
$100_{13.5}$	.0058	96.5	.276	.752	265.8 ± 6.0	$- .0184 \pm .0188$	5
$101_{13.5}$	.0320	96.5	.276	.759	257.7 ± 2.4	$- .0268 \pm .0084$	5
$104_{14.7}$	.0305	95.3	.278	.767	229.0 ± 5.2	$- .0712 \pm .0204$	5
$107_{14.7}$	.0140	95.3	.278	.767	233.4 ± 1.7	$- .0039 \pm .0048$	3
$BJ7_{16.0}$	.030	94.0	.277	.763	242.6 ± 2.1	$- .0330 \pm .0073$	5
$BJ8_{16.0}$	.030	94.0	.277	.760	229.3 ± 7.4	$- .0559 \pm .0275$	5

TABLE 6

SUPERCONDUCTIVITY IN THE IN-CD SYSTEM: REVERSIBLE THERMODYNAMIC CRITICAL FIELD

Sample No.	H_o (reversible) (Oe)	D_o (rev.)	γ (irrev.) (erg-cm^{-3}-K^{-2})	γ (rev.) (erg-cm^{-3}-K^{-2})	N(0) (irrev.) (10^{23} states ev^{-1} cm^{-3})
$99_{7.8}$	255.5 ± 2.0	$- 0.0130 \pm 0.0064$	1221 ± 28	914 ± 14	0.156
$103_{7.8}$	250.4 ± 6.6	$+ .0375 \pm .0221$	1128 ± 37	872 ± 46	.144
$94_{9.8}$	$233.7 \pm 4.6*$	$+ .0026 \pm .0217$	876 ± 24	895 ± 35	.112
$102_{9.8}$	230.0 ± 3.9	$- .0165 \pm .0146$	1055 ± 49	885 ± 30	.135
$91_{12.3}$	234.8 ± 6.8	$- .0810 \pm .0253$	1303 ± 83	1136 ± 66	.166
$97_{12.3}$	242.9 ± 3.0	$- .0017 \pm .0102$	1323 ± 26	1178 ± 29	.169
$100_{13.5}$	233.8 ± 8.5	$- .0419 \pm .0306$	1429 ± 64	1106 ± 80	.182
$101_{13.5}$	231.0 ± 1.7	$- .0406 \pm .0067$	1303 ± 24	1047 ± 15	.166
$104_{14.7}$	228.8 ± 6.4	$- .0271 \pm .0232$	995 ± 45	993 ± 56	.127
$107_{14.7}$	221.9 ± 3.4	$- .0261 \pm .0164$	1034 ± 15	935 ± 29	.132
BJ7 $_{16.0}$	226.1 ± 7.6	$- .0057 \pm .0270$	1184 ± 20	1028 ± 69	.151
BJ8 $_{16.0}$	214.0 ± 7.1	$- .0691 \pm .0290$	1072 ± 69	934 ± 62	.137

* -- To determine the reversible value of H_o for sample 94, 6 points were used.

TABLE 7

SUPERCONDUCTIVITY IN THE IN-CD SYSTEM: GORKOV PARAMETER κ_4

Sample No.	N(0) (rev.) $(10^{23}$ states $ev^{-1}-cm^{-3})$	V (irrev.) $(10^{-23}$ ev-$cm^3)$	V (rev.) $(10^{-23}$ ev-$cm^3)$	κ_4 (irrev.)	κ_4 (rev.)	ρ (irrev.) Eq. (6.8)
$99_{7.8}$	0.117	1.83	2.44	0.662 ± 0.025	0.587 ± 0.020	10.8 ± 0.5
$103_{7.8}$	.112	1.98	2.54	$.629 \pm .026$	$.559 \pm .028$	10.2 ± 0.5
$94_{9.8}$	.115	2.50	2.44	$.657 \pm .026$	$.662 \pm .030$	10.7 ± 0.5
$102_{9.8}$	.113	2.07	2.48	$.714 \pm .035$	$.658 \pm .028$	11.8 ± 0.7
$91_{12.3}$	.145	1.65	1.89	$1.082 \pm .063$	$1.012 \pm .057$	18.6 ± 1.2
$97_{12.3}$	.151	1.63	1.82	$1.101 \pm .041$	$1.024 \pm .042$	19.0 ± 0.8
$100_{13.5}$	.141	1.52	1.95	$1.091 \pm .054$	$.995 \pm .060$	18.8 ± 1.0
$101_{13.5}$	.134	1.66	2.06	$1.036 \pm .038$	$.934 \pm .032$	17.7 ± 0.7
$104_{14.7}$	.127	2.19	2.19	$1.154 \pm .057$	$1.154 \pm .063$	19.9 ± 1.1
$107_{14.7}$	.119	2.10	2.34	$1.098 \pm .039$	$1.052 \pm .045$	18.9 ± 0.7
$BJ7_{16.0}$	.131	1.83	2.11	$.826 \pm .029$	$.775 \pm .045$	13.9 ± 0.5
$BJ8_{16.0}$	.119	2.02	2.33	$.856 \pm .048$	$.802 \pm .047$	14.5 ± 0.9

TABLE 8

SUPERCONDUCTIVITY IN THE IN-CD SYSTEM: COHERENCE LENGTH AND FERMI VELOCITY

Sample No.	ρ (rev.) Eq. (6.8)	ξ_o (irrev.) (Angstrom)	ξ_o (rev.) (Angstrom)	v_F (irrev.) (10^8 cm/sec)	v_F (rev.) (10^8 cm/sec)
99 $_{7.8}$	9.3 ± 0.4	2600 ± 360	2240 ± 290	0.75	0.65
103 $_{7.8}$	8.8 ± 0.5	2540 ± 360	2190 ± 320	.74	..63
94 $_{9.8}$	10.8 ± 0.6	2230 ± 310	2260 ± 330	.57	.61
102 $_{9.8}$	10.7 ± 0.5	2470 ± 370	2240 ± 310	.65	.60
91 $_{12.3}$	17.3 ± 1.1	2750 ± 430	2560 ± 400	.66	.61
97 $_{12.3}$	17.5 ± 0.8	2790 ± 370	2570 ± 350	.68	.62
100 $_{13.5}$	17.0 ± 1.1	2900 ± 420	2620 ± 410	.70	.63
101 $_{13.5}$	15.8 ± 0.6	2740 ± 360	2450 ± 320	.68	.60
104 $_{14.7}$	19.9 ± 1.2	2410 ± 350	2410 ± 360	.60	.60
107 $_{14.7}$	18.1 ± 0.9	2460 ± 310	2350 ± 330	.61	.59
BJ7 $_{16.0}$	12.9 ± 0.9	2630 ± 330	2440 ± 390	.63	.59
BJ8 $_{16.0}$	13.4 ± 0.9	2510 ± 380	2320 ± 370	.60	.56

TABLE 9

SUPERCONDUCTIVITY IN THE IN-CD SYSTEM: EXACT EXPRESSION FOR γ'

Sample No.	γ' (irrev.) (Eq. (6.13)) (erg-cm^{-3} - K^{-2})	γ' (rev.) (Eq. (6.13)) (erg - cm^{-3} - K^{-2})
$99_{7.8}$	1319 ± 73	877 ± 30
$103_{7.8}$	1329 ± 111	988 ± 130
$94_{9.8}$	733 ± 44	975 ± 110
$102_{9.8}$	952 ± 94	840 ± 66
$91_{12.3}$	1052 ± 119	905 ± 109
$97_{12.3}$	1231 ± 53	1171 ± 67
$100_{13.5}$	1350 ± 136	977 ± 153
$101_{13.5}$	1201 ± 50	929 ± 31
$104_{14.7}$	812 ± 79	914 ± 113
$107_{14.7}$	1021 ± 31	864 ± 68
$BJ7_{16.0}$	1071 ± 41	871 ± 121
$BJ8_{16.0}$	1095 ± 151	768 ± 109

Values of the mean free path are shown in Table 4. The value of $1/\rho_n \ell$ chosen is about 5% less than the theoretical value.

While this value can certainly vary with alloying, it is close to the average value of $17.3 \times 10^{-10} \, \Omega^{-1} \, cm^{-2}$ found by Delvecchio and Lindenfeld for four dilute In-Bi alloys (76), by specific heat measurements. We may thus assume that the value of $1/\rho_n \ell$ is probably close to the quoted value for the present alloys.

Furthermore, while the order of magnitude of ℓ/ξ_o is an important quantity, the exact value of ℓ is not needed for computations.

Critical Temperature T_c

The critical temperatures were measured by the previously mentioned technique, and results are shown in Fig. 22 and Table 4. The bars on the results do not indicate the usual limits of experimental error, but rather the width of the transition ΔT_c defined previously.

The results are also compared to those of Merriam (67) and Fischer (26). We see that the transition widths are narrower in the present work than in Merriam's. This indicates that the present samples were probably more homogeneous. The transition widths of Fischer were not given.

In general, the agreement with previous data is good. T_c decreases fairly linearly from the fcc-fct phase boundary to about 12 at.% Cd, and then remains approximately constant. The present results in the latter region are somewhat lower than those of Merriam, but this may be due to the improved homogeneity.

Before discussing the temperature variation, a note on the transition width is in order. Goodman (68), noting the statistical fluctu-

LEGEND

Present work

After Merriam (67)

After Fischer (26)

T_c (K)

Concentration, at. % Cd
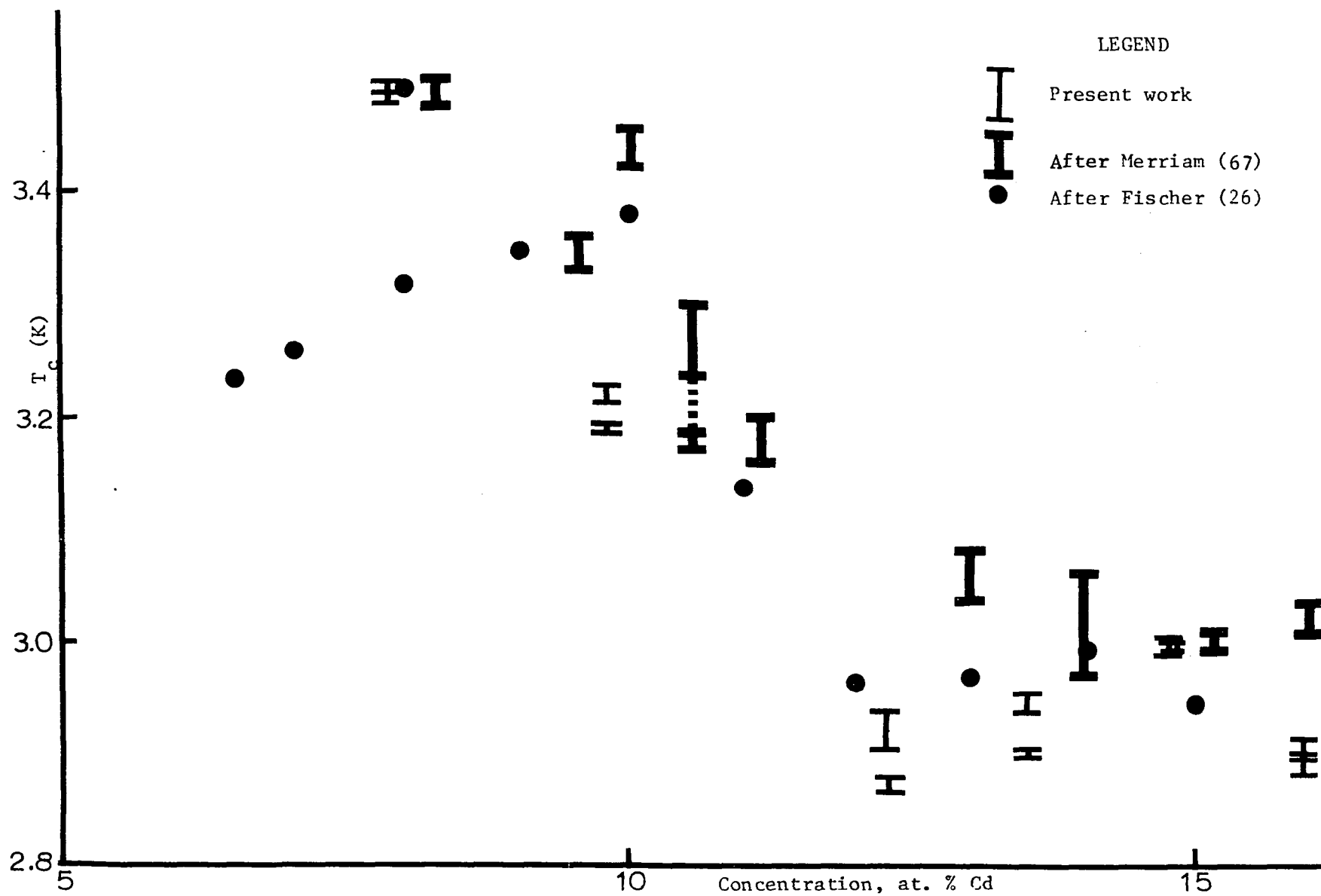
Fig. 22. Critical Temperatures of In-Cd alloys

ations in the energies of the superconducting regions, found that

$$\Delta T_c = 1.79 \times 10^4 \; k \; T_c^{5/2} \; (\rho_n \; \gamma/V)^{3/2} \; c_n^{-1} \qquad (6.4)$$

where k is the Boltzmann constant, γ is the coefficient of the electronic specific heat, and c_n is the specific heat per unit volume in the normal state. Goodman's formula has been modified to take account of the present larger definition of the transition width (i.e., from 10% - 90% of the total change in magnetization). Eq. (6.4) applies only to zero field, but the fields used in determining T_c are very small.

Since the magnitude of ΔT_c appears to be governed more by sample preparation than by concentration in our samples, only an order-of-magnitude calculation will be performed. It will be seen later that $\gamma/V \simeq 1.2$ mj cm^{-3} deg^{-2}. The molar volume of pure In is $114.8/7.3 \simeq 16$ cm^3. The specific heat c_n is not known for the present samples. However, for pure In, $c_n \simeq 70$ mj mole^{-1} deg^{-1} (57), and it changes little for dilute alloys of In (22). Substituting these values and the values of T_c and ρ_n from Table 4, we obtain $\Delta T_c \simeq 0.01$ K, which is in good agreement with the experimental results.

We may assume that this width is a natural lower boundary, as the transition widths of Merriam are larger (by a factor of about 7). ΔT_c may be larger in the present work due to the small magnetic field applied.

If we use Eq. (2.2), we may obtain the interaction strength $N(0)V$. Values are shown in Table 5. As mentioned previously, these alloys are borderline between a weak-coupling superconductor, for which $N(0)V \simeq 0.25$, and a strong-coupling superconductor, for which the BCS theory may not hold in all respects. The values of $N(0)V$ are close to

that of pure In (0.30), and vary only slightly over the range of con-
centration. There is an apparent minimum around 12 at.% Cd. We see that
even though θ_D is not known perfectly, its variation will make only a
slight change in the interaction strength.

Let us now consider the variation of T_c with concentration. Mar-
kowitz and Kadanoff (MK) (70) discussed the change in T_c with alloying
in terms of an "anisotropy effect", dominant in very   dilute alloys,
and a "valence effect", dominant in higher concentrations. However, as
Merriam has pointed out (67), problems arise as the concentrations be-
come relatively high, as is the case in the present work. This is shown
by making a "Seraphim Plot" (71), in which $\Delta T_c/c$ is plotted versus c,
where c is the concentration of the solute, and now ΔT_c is the change
in transition temperature of the alloy as compared to that of the pure
metal. If the MK theory is valid, this plot should produce a straight
line on semi-logarithmic paper.

However, due to the sharp variations in T_c shown in Fig. 23, we
do not obtain this, indicating that the MK formula is invalid in this
region of concentration.

This may be due to the assumption that the average effective
velocity $\bar{v}_F$ at the Fermi surface is not changed by alloying. Since
In has been shown to have Brillouin zone-Fermi surface overlapping
at fairly low concentrations of Cd (67), this situation may repeat it-
self at higher concentrations and make invalid the above assumption.

In general, we must conclude that while the variation in T_c is
apparently understood for very dilute alloys, this is not the case for
higher concentrations. Merriam et al (63) came to the same conclusions

about Hg-In systems.

Recently, McMillan (72) formulated a theory of T_c which employs a Coulomb pseudopotential μ^* and an electron-phonon coupling parameter λ. In principle, if these two are known, the critical temperature may be found. While the theory was formulated for strong-coupling super-conductors, it has been shown (73) that it reduces to the weak-coupling limit if λ is small. We shall use this theory to find values of λ, which is used in a renormalization of the density of states $N(0)$ by a factor $(1 + \lambda)$.

We must first obtain μ^* from the isotope shift. Since this has not been determined for In, we shall use the formula of Morel and Anderson (74), which works well for intermediate-coupling superconductors like Sn. This yields an isotope exponent of 0.435 for all samples in Table 5, close to the typical value of 0.50. Then

$$\mu^* \simeq 0.36\{ \ln(\theta_D/1.45 \; T_c) \}^{-1} \tag{6.5}$$

The value of μ^* is used in the McMillan equation for λ, and this is shown in Table 5. We see that the values are fairly uniform, although there is a slight decrease towards the middle of the concentration range. The values of λ are somewhat higher than $\lambda = 0.69$ calculated for pure In by McMillan. Kubota et al (79) also showed that λ varies only slowly with composition in Ta-Nb alloys.

Thermodynamic Field H_c

The field H_c is found from the area under the magnetization curve, as mentioned above. In general, H_c varies in a parabolic manner with

temperature. However, Sheahen (75) showed, in an approximation to a

proposed exact equation, that small corrections to the parabola may be

added as follows for non-transition metal superconductors:

$$H_c/H_o = 1 - (T/T_c)^2 - D_o \sin \{ \pi(T/T_c)^2 \} \qquad (6.6)$$

where H_o is the thermodynamic field at T = 0 K, and D_o is the maximum

deviation from a parabola for the particular superconductor. H_o was com-

puted by a least-squares methods from experiments in which $(T/T_c)^2 \leq 0.5$

(i.e., using primarily those values of H_c close to H_o), and results are

presented in Tables 5 and 6. The parameter D_o was also computed.

Up to the present, we have been using the (forward) irreversible

curves in the computation of H_o. If we use the hysteretic theory of

Chapter V to determine the probable reversible curves, we obtain some-

what different results. Because of the large amount of data, the least-

squares analysis used in Chapter V was not used. Instead, curves similar

to the data were computed and they were adjusted by hand to fit part-

icular cases. It is estimated that the errors in this procedure should

not be more than a few percent in any of the superconducting variables.

To determine the curves, the procedure used in obtaining Fig. 17 was fol-

lowed: H_{c_2}, $\left.\dfrac{dM}{dH}\right|_{H_{c_2}}$ were held as fixed, and H_{c_1} was variable. This

generally produced a value of H_{c_1} smaller than that previously found.

A planimeter was used to find the ratio of reversible to irreversible

areas.

The values of H_o found in these two ways are shown in Fig. 23.

Both curves indicate a maximum of H_o near the center of the fcc phase
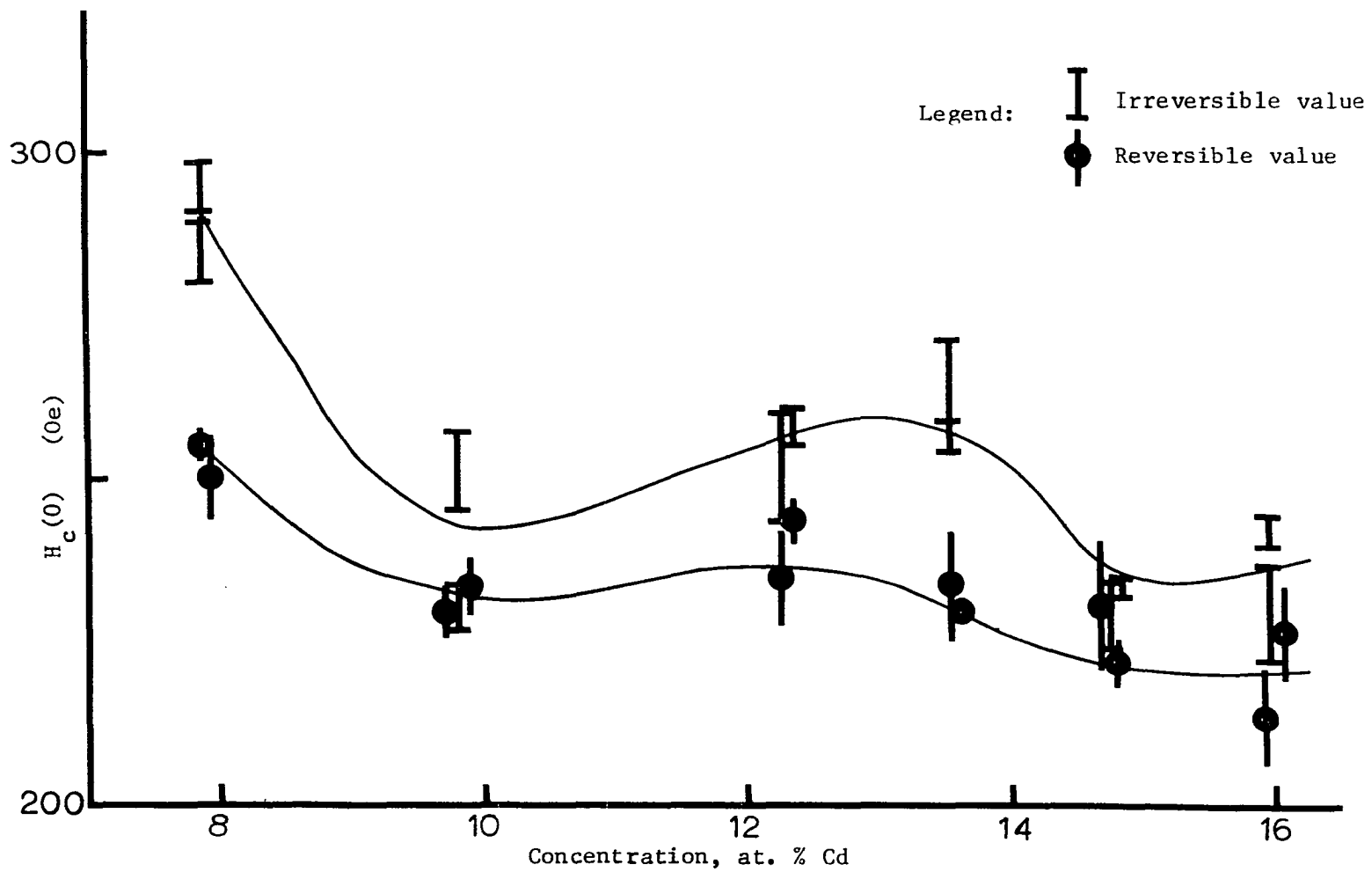
Fig. 23. Thermodynamic critical field H_c at $T = 0$ for In–Cd system, for irreversible and reversible curves.

81

(at around 13 at. % Cd), but the reversible value of H_o tends to be more constant. This result agrees strongly with the work of Dubeck et al (32) who found that the scheme they used to find a reversible curve from the irreversible curves tended to even out the irregularities of H_o versus concentration in Pb-In alloys.

In the BCS model, the electronic coefficient of specific heat is

$$\gamma = 0.17 \ (H_o/T_c)^2 \tag{6.6a}$$

Computed coefficients are shown in Table 6. The standard deviations were computed only from those of H_o, as any error in T_c would be negligible. The values of γ computed for the reversible curves tend to be less erratic than those for the irreversible curves. γ for pure In is 1088 erg $cm^{-3} \ K^{-2}$ (84). While there are substantial changes in the value of γ, it should be recalled that γ is proportional to the density of states $N(0)$ at the Fermi surface. It has been shown (60) that this density may change significantly for low concentrations of Cd in In; it may continue to do so at higher concentrations. Large changes in γ have been shown in other materials with changes in concentration (78) (82).

In the free electron model of solids,

$$\gamma = (2/3)\pi^2 \ N(0) \ k^2 \tag{6.7}$$

This model has been used for In-Cd alloys (117). $N(0)$ may be found from Eq. (6.7) and is presented in Tables 6 and 7.

Using the values of $N(0)V$ shown in Table 5, V, the net interaction energy between electrons, may be found. Results are shown in Table 7. Since $\delta N(0)/N(0) = \delta V/V = \delta\gamma/\gamma$, where δ indicates the standard error, they are not shown. While the $N(0)$ versus concentration curves are not linear, Merriam (67) points out that these curves generally have much

structure. Because of the relative constancy of $N(0)V$, the same comments would apply to V. However, the exact physical interpretation of $N(0)$ and V should be approached with caution (118).

The value of V for pure In is 2.1×10^{-23} ev - cm^3 (85). Little has been done on the variation of V with alloying, although Gayley et al (77) deduced that the changes in T_c they observed were due to changes in V with alloying, and Hulm et al (83) also found that V could vary with concentration.

The values of $N(0)$ (and thus V) may be altered by considering the enhancement of γ by the electron-phonon interaction, as discussed by McMillan (noted above). This will add a factor of $(1 + \lambda)$ to the right hand side of Eq. (6.7), with the consequent change in $N(0)$. This decreases $N(0)$ by a factor of about 1.8 and increases V by this factor. However, due to the slight changes in λ with concentration, the relative values of $N(0)$ and V with concentration will change only a small amount.

The value of κ_4 (from Eq. (2.9)) may now be determined. This quantity is independent of temperature due to the independence of γ and ρ_n. To find κ_4, we must have the value of κ_o for pure In, which is 0.062 (76). Since the statistical and systematic error of ρ_n are not known (but are expected to be small, on experimental and theoretical grounds), a standard deviation of $\pm 3\%$ has been arbitrarily assigned to this quantity, to be used in the computation of the standard error of κ_4.

The values of κ_4 are shown in Table 7. In general, they increase initially with concentration, and level off around 12 at. % Cd. The values for κ_4 for the reversible curves tend to be lower than those for the irreversible curves. It will be seen later that the trend indicated by κ_4 is repeated in the other GL parameters.

We can now use the results of Gorkov (80) to determine an impurity

parameter ρ from the equations

$$\kappa_o/\kappa_4 \equiv \chi(\rho)$$

$$\chi(\rho) = \frac{8}{7\zeta(3)\ \rho}\left[\ \frac{\pi^2}{8}\ -\frac{1}{2\ \rho}\{\psi(\tfrac{1}{2} + \tfrac{\rho}{2}) - \psi(\tfrac{1}{2})\}\right] \qquad (6.8)$$

where $\zeta(x)$ is the Riemann zeta function, and $\psi(x)$ is the digamma function.

Eqs. (6.8) are used to find ρ from the values of κ_o and κ_4. Results are

presented in Tables 7 and 8. The standard error in ρ is found from the

fact that for the values of ρ we are dealing with, $\chi(\rho) \propto (1/\rho)$ almost

exactly. It should be noted (76) that this analysis depends strongly on

the value of κ_o.

Now $$\rho \equiv \xi_o/\ell \qquad (6.9)$$

where ξ_o is the BCS (or intrinsic) coherence length of the BCS super-

conducting wavefunctions. Using the values of ℓ determined from Eq. (6.3),

ξ_o was calculated and presented in Table 8.

Using other BCS assumptions,

$$\xi_o = 0.18\ \hbar\ v_F/k\ T_c \qquad (6.10)$$

The electron velocity at the Fermi surface v_F may thus be found using

Eq. (6.10) and the previously computed values of ξ_o. Results are pre-

sented in Table 8.

The electronic coefficient of specific heat (see Eq. (6.6a)) may

be calculated in a thermodynamically exact manner, rather than using

the BCS model. We then have (87)

$$\gamma' = (-1/4\pi)(H_o/T_c)^2 \left(h\ \frac{d^2h}{dt^2}\bigg|_{t\ =\ 0} \right) \qquad (6.11)$$

where $h = H_c/H_o$. To evaluate the derivative properly, we use Sheahen's

(75) exact expression for $h(t)$ (from which Eq. (6.6) is derived):

$$h + D_o \sin \pi h = 1 - t^2 \tag{6.12}$$

Making use of Eq. (6.12) and noting that $\left.\dfrac{dh}{dt}\right|_{t = 0} = 0$, upon substitution in Eq. (6.11) we find

$$\gamma' = \gamma_{BCS}/(1 - \pi D_o) \tag{6.13}$$

where γ_{BCS} is the electronic coefficient of specific heat computed with the BCS assumptions, from Eq. (6.6a). The thermodynamically exact coefficient γ' is tabulated in Table 9. The values of γ' are smaller than γ_{BCS}, except for a few samples with low Cd concentration.

Because of the uncertainty in D_o, the standard error in γ' will be greater than that in γ ($\equiv \gamma_{BCS}$). We shall not discuss the coefficient γ' further in this chapter, except to note that there is still a maximum around the region of 13 at. % Cd, and that γ' computed from the reversible curves tends to have little variation with concentration. Using the BCS formula Eq. (6.6a) produces values of γ which tend to be more erratic than those of Eq. (6.12).

Summary

In this chapter, we have discussed the primary characteristics of the superconducting samples as a function of concentration. Certain quantities like the Debye temperature must be estimated. However, quantities like H_o and T_c are known to a good degree of accuracy. In connection with the former quantity, the hysteresis theory described previously was used to determine a "reversible" H_o.

From the known quantities, plus an estimate of the mean free path from the measured residual resistivity, other superconducting parameters may be found. Many of them show a maximum around 10 - 12 at. % Cd., which may be due to BZ-Fermi surface interactions, as described above.

CHAPTER VII

RESULTS AND DISCUSSION: SECONDARY PROPERTIES

In this chapter we shall discuss the superconducting properties

and parameters which do not depend on T_c and H_o, i.e., H_{c_1} and H_{c_2}, and

the parameters κ_1, κ_2, etc., which can be derived from them.

Let us first consider H_{c_1}, the point of initial field penetra-

tion. There is a dichotomy in the literature with regard to its def-

inition with respect to the magnetization curves. Usui et al (88), Kub-

ota et al (79), and Ogasawara et al (89) defined H_{c_1} as the field

where the perfect diamagnetic line intersects the descending magnetiz-

ation curve, extrapolated to low fields. Ikushima (78) defined H_{c_1} as

the point of maximum magnetization.

These authors were all working with hard superconductors with

high κ and well-defined magnetization curves. Working with soft super-

conductors, Dubeck et al (32) and Farrell et al (90) defined H_{c_1} as

the point of first departure from perfect diamagnetism. For samples of

finite length (implying some rounding near the maximum of magnetization)

this definition will yield a different value of H_{c_1} from the preceding

definition.

In the present work, rounding of the magnetization curve near

H_{c_1} was observed, due probably to non-equilibrium behavior, the geo-

metry of the sample, possible slight inhomogeneities in the sample,

and the tapping method used. The former definition of H_{c_1} was used, which usually meant that H_{c_1} was in fact close to the maximum of magnetization.

When the reversible curves were plotted according to the hysteresis theory in Chapter V, it was found that H_{c_1} defined by this hysteresis method coincided with the point of first departure from perfect diamagnetism, or even fell before it. It may be recalled that Goedemoed's (33) data indicated that the "reversible" H_{c_1} fell before the first departure from linearity.

The Abrikosov theory predicts a well-defined H_{c_1} with a vertical drop from the line of perfect diamagnetism. Obviously, metallurgical and geometrical considerations tend to blur out this region; a study of these effects would be useful. However, we shall at present only take note of the definition employed in Abrikosov's work.

A second consideration is the variation of H_{c_1} with temperature. H_{c_1} follows a roughly parabolic relationship with $T/T_c = t$. However, as in the discussion of H_c, deviations from this occur. The authors mentioned above attempted to take account of this by expanding $H_{c_1}(t)$ in a sum of powers of t^2: e.g., $H_{c_1} = H_{c_1}(0)(1 - a_1 t^2)$ or $H_{c_1}(0)\{1 - a_2 t^2 - (1 - a_3)t^4\}$, where the a_n are constants. However, it would be consistent with the previously assumed relationship between H_c and t (Eq. (6.6)) to write

$$H_{c_1}(t)/H_{c_1}(0) = 1 - (T/T_c)^2 - D_{o_1} \sin \pi(T/T_c)^2 \qquad (7.1)$$

The quantity D_{o_1} will again be a measure of the deviation of H_{c_1} from parabolicity as a function of temperature.

The experimental definition of H_{c_2} is less open to experimental

question than that of H_{c_1} : it is the point where the magnetization vanishes. Both the theoretical and experimental curves are straight lines at $H \simeq H_{c_2}$, so the determination of this point is straightforward. However, for most of the present samples there was a small but measurable negative magnetization past this point. This magnetization gradually diminished with increasing fields. The effect has been seen in the work of other authors (91), and presumably is related to the finite size of the samples.

Care was taken to ensure that this effect did not obscure the determination of the correct H_{c_2}.

As in the case of H_{c_1}, various writers have constructed polynomials to describe a temperature dependence of H_{c_2}. For consistency with the previous definitions, we write

$$H_{c_2}(t)/H_{c_2}(0) = 1 - (T/T_c)^2 - D_{o_2} \sin \pi (T/T_c)^2 \qquad (7.2)$$

To find the parameters in Eqs. (7.1) and (7.2), we shall use all the data in the present work. This usually is 8 or more temperatures for each alloy concentration, approximately equally spaced between T_c and 1.1 K, the lowest achievable temperature.

Results are presented in Tables 10 and 11, and Figs. 24 and 25. The differences in the number of points for each set of data are due to the fact that a small number of points were erratic. A number of conclusions may be drawn from the data. We see that the value of $H_{c_1}(0)$ (found by the least squares method from Eq. (7.1)) for both the reversible and irreversible curves drops sharply with concentration. However, we do see a slight rise in the two samples with the highest concentration, indicating that these samples may contain more than one phase,

TABLE 10

LOWER CRITICAL FIELD $H_{c_1}(0)$

Sample No.	$H_{c_1}(0)$ (irrev.) (Oe)	D_{o_1} (irrev.)	Number of points	$H_{c_1}(0)$ (rev.) (Oe)	D_{o_1} (rev.)	Number of points
$99_{7.8}$	259 ± 4	$+\ 0.008 \pm 0.012$	7	199 ± 4	$-\ 0.042 \pm 0.015$	7
$103_{7.8}$	267 ± 10	$+\ 0.094 \pm .027$	9	198 ± 6	$+\ .046 \pm .019$	9
$94_{9.8}$	213 ± 9	$+\ 0.102 \pm .033$	9	174 ± 7	$+\ .044 \pm .028$	9
$102_{9.8}$	205 ± 4	$-\ 0.022 \pm .014$	8	161 ± 5	$-\ .042 \pm .020$	8
$91_{12.3}$	160 ± 9	$-\ 0.171 \pm .038$	8	130 ± 7	$-\ .167 \pm .066$	7
$97_{12.3}$	162 ± 12	$-\ 0.158 \pm .050$	8	135 ± 7	$-\ .110 \pm .037$	7
$100_{13.5}$	168 ± 9	$-\ 0.129 \pm .031$	9	124 ± 4	$-\ .159 \pm .024$	8
$101_{13.5}$	168 ± 7	$-\ 0.065 \pm .027$	8	136 ± 5	$-\ .064 \pm .020$	8
$104_{14.7}$	144 ± 12	$-\ 0.027 \pm .043$	9	106 ± 10	$-\ .155 \pm .063$	9
$107_{14.7}$	142 ± 14	$-\ 0.017 \pm .056$	5	106 ± 13	$-\ .142 \pm .090$	5
$BJ7_{16.0}$	156 ± 5	$-\ 0.088 \pm .018$	8	120 ± 7	$-\ .078 \pm .033$	8
$BJ8_{16.0}$	164 ± 7	$-\ 0.009 \pm .022$	8	119 ± 2	$-\ .089 \pm .012$	8

69

TABLE 11

UPPER CRITICAL FIELD $H_{c_2}(0)$

Sample No.	$H_{c_2}(0)$ (Oe)	D_{o_2}	Number of points	$H'_c(0)$ (irrev.) (Oe)	D'_o (irrev.)	$H'_c(0)$ (rev.) (Oe)
$99_{7.8}$	369 ± 3	+ 0.046 ± 0.005	7	295 ± 3	+ 0.018 ± 0.007	257 ± 2
$103_{7.8}$	359 ± 3	+ .037 ± .006	9	288 ± 4	+ .059 ± .012	249 ± 5
$94_{9.8}$	409 ± 4	+ .046 ± .008	10	257 ± 6	− .030 ± .016	229 ± 3
$102_{9.8}$	381 ± 3	+ .036 ± .004	8	256 ± 5	− .011 ± .012	232 ± 3
$91_{12.3}$	486 ± 41	− .183 ± .064	7	231 ± 14	− .170 ± .045	211 ± 16
$97_{12.3}$	428 ± 51	− .218 ± .091	8	217 ± 21	− .206 ± .071	196 ± 22
$100_{13.5}$	448 ± 50	− .203 ± .079	9	237 ± 12	− .139 ± .033	204 ± 13
$101_{13.5}$	460 ± 27	− .127 ± .040	8	242 ± 11	− .089 ± .029	213 ± 11
$104_{14.7}$	474 ± 25	− .169 ± .037	10	212 ± 16	− .143 ± .050	196 ± 17
$107_{14.7}$	486 ± 49	− .145 ± .073	5	203 ± 16	− .130 ± .056	190 ± 17
$BJ7_{16.0}$	467 ± 27	+ .014 ± .030	8	238 ± 11	− .047 ± .026	216 ± 11
$BJ8_{16.0}$	424 ± 37	− .098 ± .055	8	214 ± 15	− .132 ± .045	197 ± 14

TABLE 12

GINZBURG–LANDAU PARAMETER κ_1 AT $T = T_c$

Sample No.	D'_o (rev.)	$\kappa_1(T_c)$ (irrev.)	$\kappa_1(T_c)$ (rev.)	ρ^*_n (rev.) ($\mu\Omega$-cm)	ρ^* Eq. (7.8)	y Eq. (7.10) (irrev.)	y Eq. (7.10) (rev.)
$99_{7.8}$	$-\ 0.007 \pm 0.005$	0.82	0.87	2.95	14.7	1.025	1.008
$103_{7.8}$	$+\ .040 \pm\ .016$	0.94	1.03	3.69	17.7	0.949	0.981
$94_{9.8}$	$-\ .012 \pm\ .009$	0.89	1.06	4.30	18.2	1.007	1.020
$102_{9.8}$	$-\ .007 \pm\ .007$	0.91	1.02	3.77	17.5	1.003	0.993
$91_{12.3}$	$-\ .202 \pm\ .057$	1.63	1.40	4.69	24.2	0.973	0.918
$97_{12.3}$	$-\ .230 \pm\ .085$	1.58	1.36	4.51	23.5	0.985	0.905
$100_{13.5}$	$-\ .190 \pm\ .045$	2.08	1.73	5.63	30.4	0.977	0.954
$101_{13.5}$	$-\ .125 \pm\ .036$	1.61	1.54	5.21	26.9	0.989	0.919
$104_{14.7}$	$-\ .181 \pm\ .060$	1.86	1.57	6.10	27.4	0.997	0.950
$107_{14.7}$	$-\ .170 \pm\ .067$	1.84	1.54	5.85	26.9	0.982	0.919
$BJ7_{16.0}$	$-\ .048 \pm\ .028$	1.24	1.36	4.79	23.5	1.000	1.000
$BJ8_{16.0}$	$-\ .161 \pm\ .049$	1.19	1.09	4.02	18.8	0.990	1.004

TABLE 13

PENETRATION DEPTH AND ENERGY GAP

| Sample No.	$\lambda(0)$ Eq. (7.11) (irrev.) (Angstrom)	$\lambda(0)$ Eq. (7.11) (rev.) (Angstrom)	$\xi(0)$ Eq. (7.12) (Angstrom)	$2\Delta(0)/kT_c$ (rev.)	$h^*(0)$ (rev.)
$99_{7.8}$	840 ± 10	960 ± 10	945 ± 4	3.59 ± 0.03	0.68
$103_{7.8}$	845 ± 15	980 ± 25	960 ± 4	3.31 ± .13	.57
$94_{9.8}$	1010 ± 25	1130 ± 20	900 ± 4	3.51 ± .12	.67
$102_{9.8}$	980 ± 20	1080 ± 15	930 ± 4	3.61 ± .08	.66
$91_{12.3}$	1225 ± 125	1345 ± 155	825 ± 35	3.94 ± .12	.60
$97_{12.3}$	1225 ± 190	1355 ± 230	880 ± 52	3.53 ± .06	.53
$100_{13.5}$	1150 ± 120	1335 ± 160	860 ± 48	3.74 ± .16	.45
$101_{13.5}$	1140 ± 85	1295 ± 105	845 ± 25	3.74 ± .03	.53
$104_{14.7}$	1325 ± 135	1425 ± 160	835 ± 22	3.67 ± .12	.54
$107_{14.7}$	1400 ± 185	1490 ± 210	825 ± 42	3.66 ± .09	.58
$BJ7_{16.0}$	1170 ± 85	1285 ± 100	840 ± 24	3.55 ± .15	.62
$BJ8_{16.0}$	1240 ± 140	1345 ± 155	880 ± 38	3.88 ± .15	.74
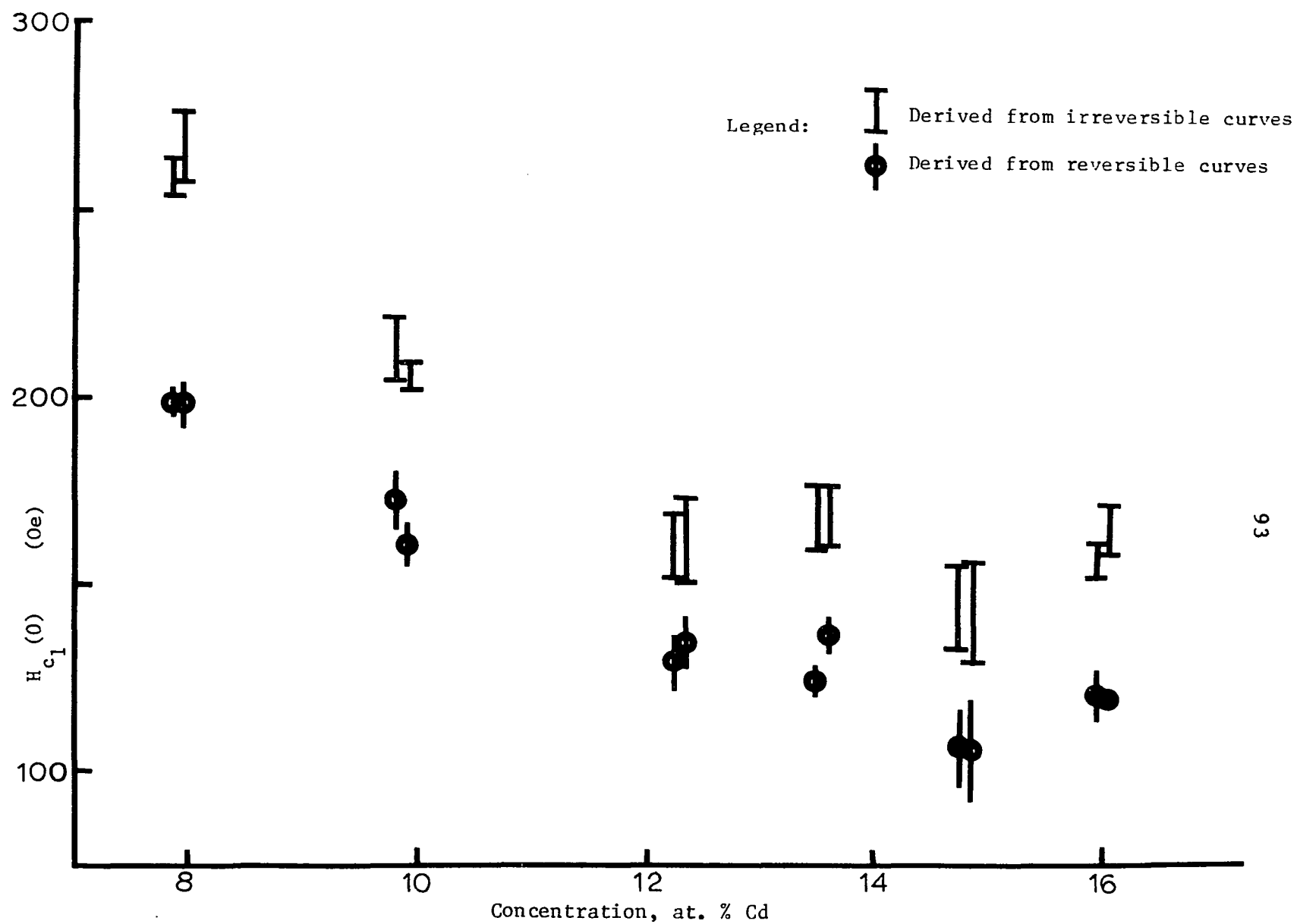
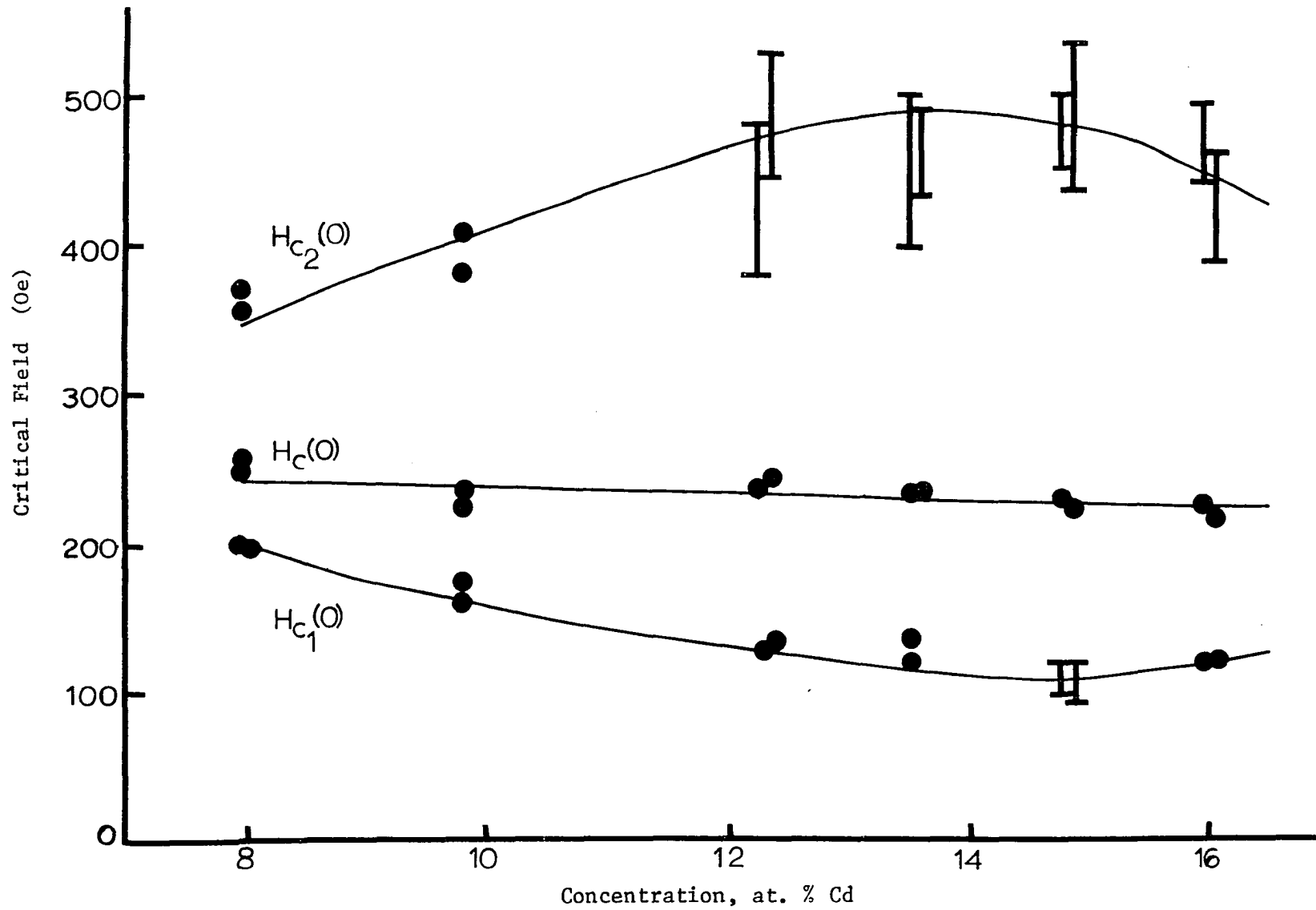Fig. 24. $H_{c_1}(0)$ as a function of concentration for irreversible and reversible curves.

93

Fig. 25. Critical fields at T = 0 for In-Cd alloys (derived from reversible curves). The bars indicate standard deviations. The standard deviations for the dotted points are too small to be indicated.

as noted above. The difference in $H_{c_1}(0)$ between the reversible and irreversible cases is greatest at lowest concentrations, and decreases with increasing concentration.

The pattern described above is repeated in Fig. 25. Since we shall show later that the results obtained from the irreversible curves tend to be inconsistent with theory, we shall dwell primarily on the data obtained from the reversible curves.

Fig. 25 is very similar to Fig. 20 of Livingston and Schadler (14), in that the critical fields tend to converge at both a high and a low concentration end of a metallurgical phase to a Type I behavior: i.e., $H_{c_1}(0) \rightarrow H_{c_2}(0) \rightarrow H_c(0)$ at these concentrations of two mutually soluble superconductors. The physical basis for this is that at the low concentration end of a phase, the material starts to display Type I characteristics; at the high end, precipitation of the solute tends to eliminate the Type II characteristics and reversion to primarily Type I behavior follows.

As mentioned in the previous chapter, the data reach a maximum in the region of 10 - 12 at. % Cd. This phenomenon will be repeated in the parameters which will be discussed below.

Ginzburg-Landau Parameter κ_1

In order to consider the temperature and concentration variation of $\kappa_1(t)$, we shall need to normalize this parameter. This is done by finding $\kappa_1(T_c)$, and comparing values of $\kappa_1(T)/\kappa_1(T_c)$. From the definition $H_{c_2} = \sqrt{2} \, \kappa_1 \, H_c$, we find upon differentiation

$$\kappa_1(1) = \frac{(dH_{c_2}/dt)\big|_{t=1}}{\sqrt{2} \, (dH_c/dt)\big|_{t=1}} \qquad (7.3)$$

If we use Eq. (6.12) and its analogy for H_{c_2} (Eq. (7.2)), we obtain

$$\kappa_1(1) = \frac{H_{c_2}(0)(1 + D_o'\pi)}{2\,H_c'(0)(1 + D_{o_2}\pi)} \qquad (7.4)$$

The quantities $H_c'(0)$ and D_o' are primed. They refer to the values of $H_c(0)$ and D_o obtained by using the thermodynamic critical field data from the entire range of t, not only $t^2 \leq 0.5$, as was the case in the computation of $H_c(0)$ and D_o. Sheahen (75) pointed out that extrapolation to find $H_c(0)$ using high values of t solely have not been reliable, and it was decided to use all the data to minimize the standard error. $H_c'(0)$ and D_o' were computed by the least-squares method. It is found that $H_c'(0)$ differs little from $H_c(0)$, as shown in Table 10.

$\kappa_1(T_c)$ as computed by Eq. (7.4) is presented in Table 12 and Fig. 26. The values of $\kappa_1(T_c)$ for the reversible and irreversible curves are similar in their variation with concentration.

By definition (93),

$$\kappa_1(T_c) \equiv \kappa_4 \qquad (7.5)$$

As mentioned above, κ_4 is independent of temperature. As shown in Fig. 26, the two parameters (as found by Eqs. (7.4) and (2.9)) are not equal for any value of concentration. The reason for this discrepancy is not immediately obvious. The substitution of Fischer's resistivity data (26) for those of the present work does not eliminate the difference. Using the alternative definition of γ, mentioned in Chapter VI, only increases $(\kappa_1 - \kappa_4)$ further.

Dubeck et al (32) have noted $(\kappa_1 - \kappa_4) \neq 0$ for Pb-In alloys. Farrell et al (90) also note a difference between κ_1 and κ_4 for Pb-In alloys. These authors treated the residual resistance ρ_n as a para-
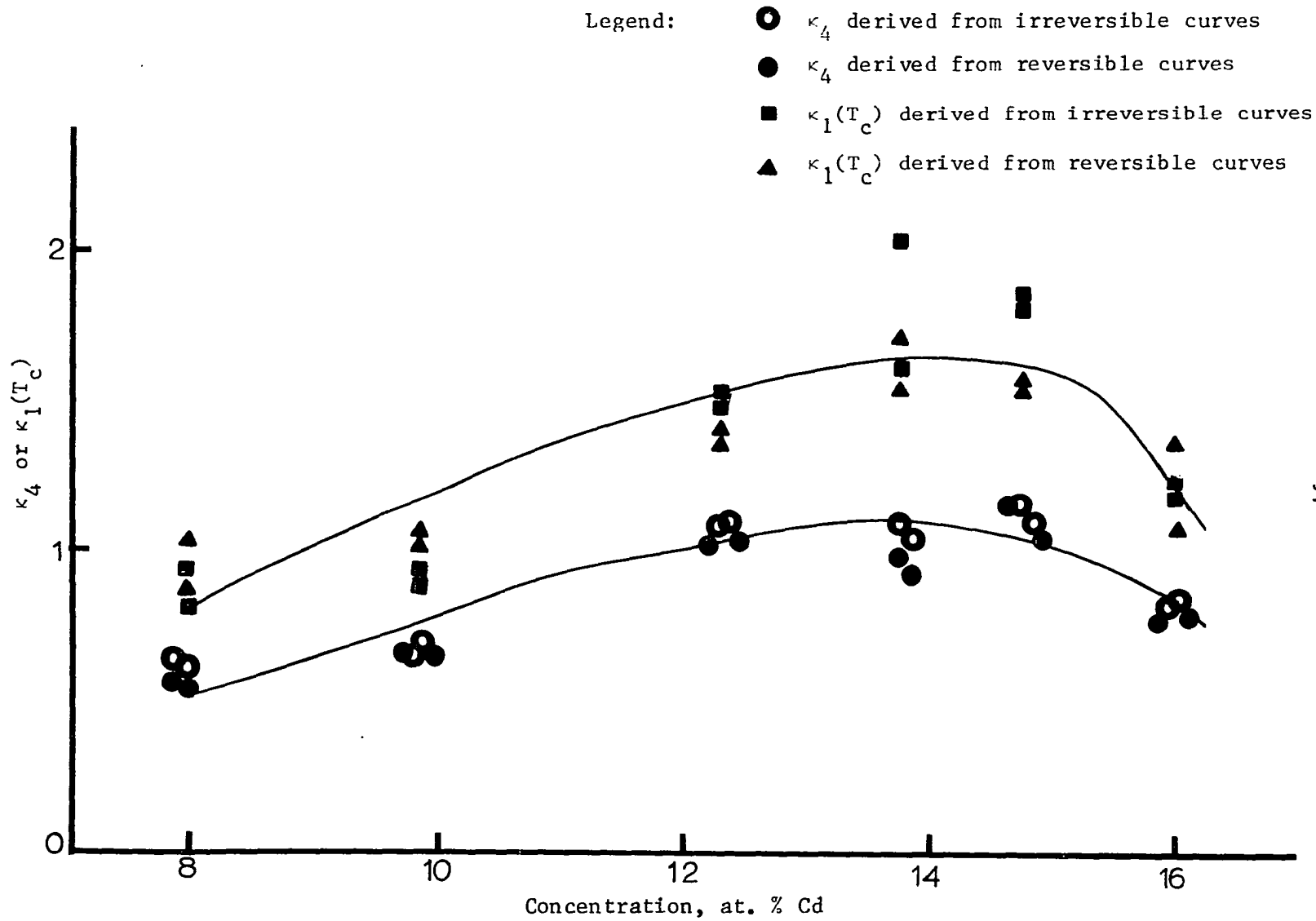
Fig. 26. κ_4 and $\kappa_1(T_c)$ as a function of concentration.

meter by requiring it to fit the two equations

$$\rho * \kappa_o / \kappa_4 = \rho * \chi(\rho *) = 8.85 \times 10^{-3} \gamma^{\frac{1}{2}} \rho_n^* / \kappa_1$$

$$\rho * = 8.85 \times 10^{-3} \gamma^{\frac{1}{2}} \rho_n^* / \kappa_o$$

(7.6)

where ρ_n^* is the now adjustable residual resistivity, and $\rho *$ is the now adjustable Gorkov impurity parameter. The purpose of the computation is to set $\kappa_1 = \kappa_4$ (as is explicitly shown in the first of Eqs. (7.6)). ρ_n^* is adjusted to make the values of $\rho *$ of each equation equal. The values of ρ_n^* and $\rho *$ are shown in Table 12 for the reversible case. γ was obtained from Table 6.

The adjusted values of ρ and ρ_n are in every case larger than the measured value. They show approximately the same variation with concentration as the measured values, however. Furthermore, the adjusted values of residual resistance are greater than Fischer's values for all except the highest concentrations, as shown in Fig. 21 and Table 12.

Thus, while the method described above may have some validity in reconciling the differences between κ_1 and κ_4, it must be used with caution. As previously mentioned in Chapter VI, the entire procedure is highly dependent on the value of κ_o chosen.

In Fig. 27, ρ_n^* is plotted as a function of $\kappa_1(T_c)$. The least-squares intercept is at $\kappa_1(T_c) = 0.049$, close to the expected value of 0.062. The linearity is worth noting, since if we set $\kappa_1(T_c) = \kappa_4$, $\kappa_1(T_c)$ should vary linearly with the residual resistivity (from Eq. (2.9)) if γ is constant. The Farrell procedure may then be equivalent to setting γ constant, which may not be the case experimentally.

While there appear to be differences between κ_1 and κ_4 among non-transition metal superconductors, Hechler et al (93) found agree-
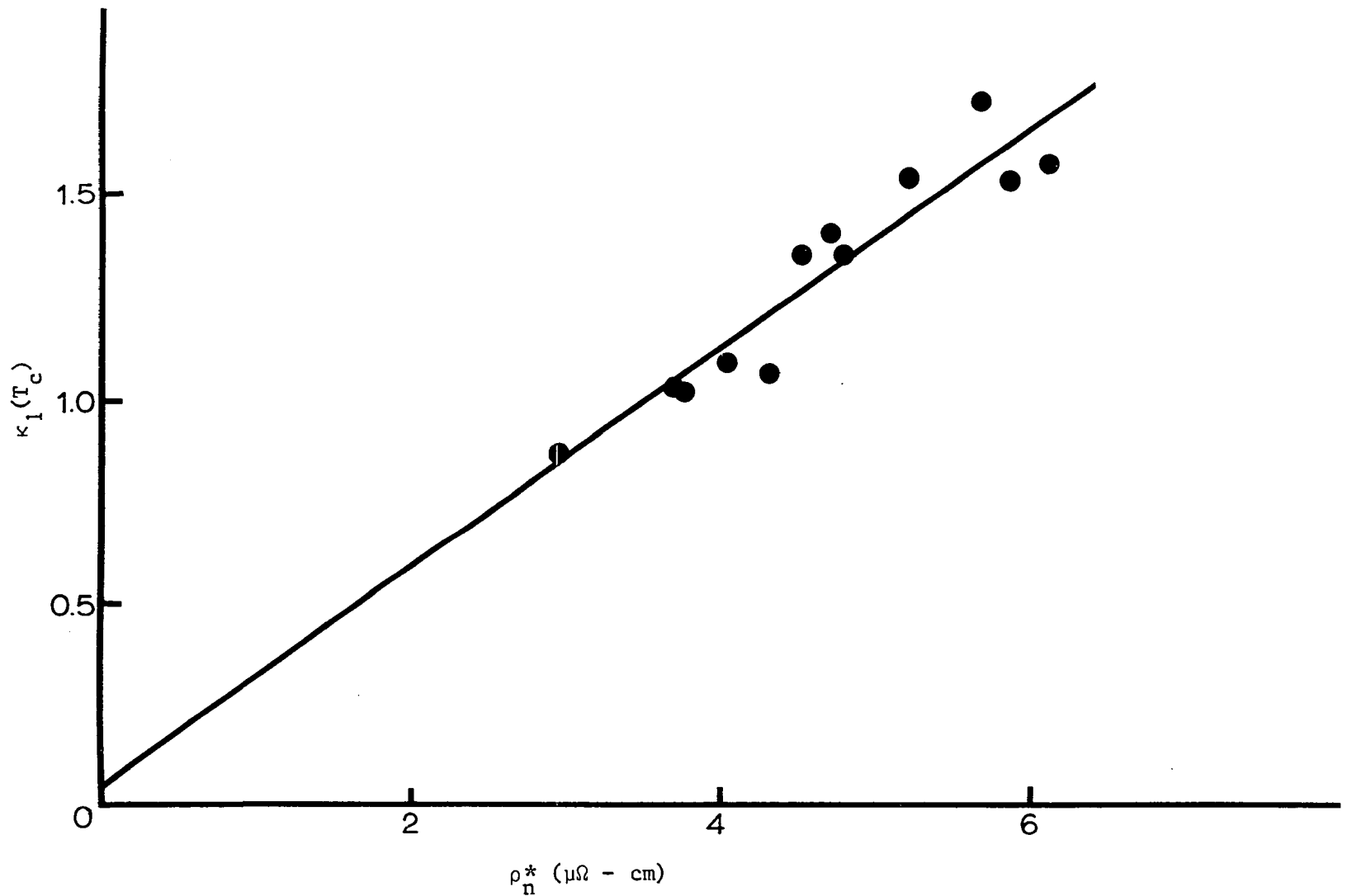
Fig. 27. ρ_n^* as a function of $\kappa_1(T_c)$.

ment between the two to within 10% for Nb alloys.

As previously mentioned, Eilenberger (81) has derived the theoretical basis of κ_1 and κ_2 as a function of the impurity parameter ρ and reduced temperature t. Let us now consider some aspects of the theory.

Fig. 28 shows the GL parameter κ_1 at 0 K $\{\kappa_1(0) = H_{c_2}(0)/\sqrt{2} H_c(0)\}$ plotted versus the impurity parameter ρ. $\kappa_1(0)$ has been normalized by dividing by $\kappa_1(T_c)$. Line A is the calculation of Helfand and Werthamer (94), and lines B and C are the calculations by Eilenberger for different values of the quantity ℓ_{tr}/ℓ. B corresponds to a value of 1.0, and C to 2.0. ℓ_{tr}/ℓ is proportional to the anisotropy of the impurity scattering. For example, if $\ell_{tr}/\ell = 1$, isotropic scattering from impurity atoms takes place. Most of the points derived from the reversible curve lie close to the Eilenberger curves (although a higher ratio of ℓ_{tr}/ℓ would probably fit the points better), and those points derived from the irreversible curves are more scattered.

To put this on a more quantitative basis, the average values of $\kappa_1(0)/\kappa_1(T_c)$ were calculated for both the reversible and irreversible cases. These were, respectively, 1.12 ± 0.12 and 0.98 ± 0.18. This indicates a higher scatter in the irreversible case, as well as a lower (and unphysical) value of $\kappa_1(0)/\kappa_1(T_c)$ as compared to the reversible case. The average value for the reversible case falls slightly below the line labelled C in Fig. 28.

For comparison, we have shown the data of Culbert et al (95) for $\kappa_1(0.2)/\kappa_1(T_c)$ in Pb-In alloys. A calculation using the assump-
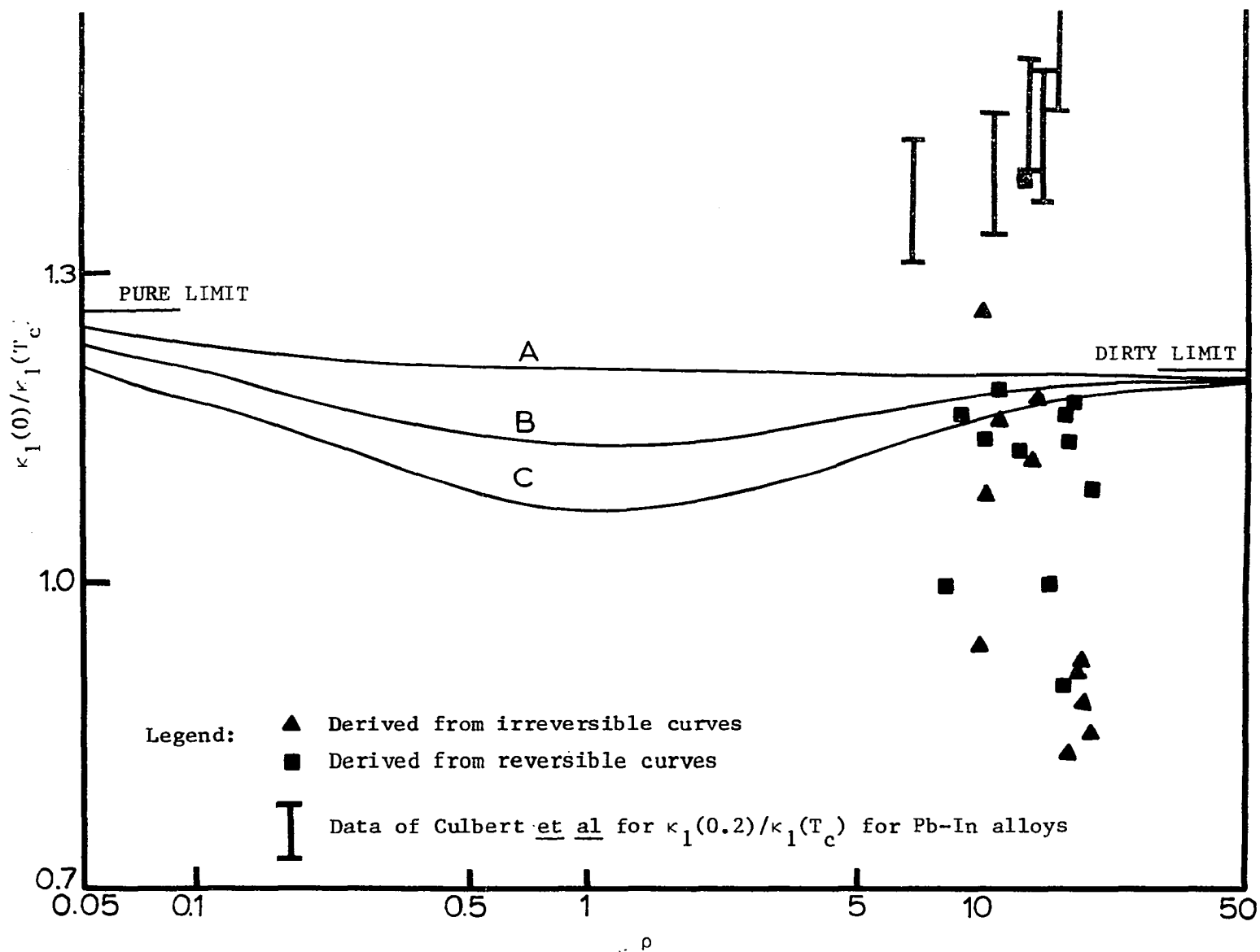
Fig. 28. Reduced Ginzburg-Landau parameter κ_1 at 0 K versus impurity parameter ρ.
$$\kappa_1(0) = H_{c_2}(0)/\sqrt{2}\,H_c(0).$$

tions used in deriving Eq. (7.3) shows that this quantity equals

$\kappa_1(0)/\kappa_1(T_c)$ to within a few percent. This set of data does not agree

well with the Eilenberger theory. Culbert et al ascribe the difference

to strong-coupling effects in their alloys, noting that the Eilenberger

theory is based on weak coupling. The scatter in the Culbert data is

less than in the present work.

Usui et al (88) also found substantial differences from the

Eilenberger theory in pure vanadium. Again, this may be due to strong

coupling effects in the material.

Now consider the variation of κ_1 with temperature. The Eilenber-

ger theory discusses $\kappa_1(T_c)$ as a function of ρ and ℓ_{tr}/ℓ. Fig. 29 shows

the results of the theory for the pure limit ($\rho = 0$) and the "dirty"

limit ($\rho \to \infty$). The theory depends only to a slight extent on the ratio

ℓ_{tr}/ℓ; in view of the results of Fig. 28, ℓ_{tr}/ℓ was arbitrarily chosen

as 2.0.

Since it would take considerable space to present all the ex-

perimental data, only representative samples were chosen. The most ob-

vious result is that the points derived from the irreversible curves

tend to be considerably more erratic than those derived from the revers-

ible curves. For example, in sample $91_{12.3}$ the former points are not

represented because they fall below $\kappa_1(T)/\kappa_1(T_c) = 1$. This pattern will

be repeated in the discussion of κ_2.

Due to the scatter of even the reversible data, it is difficult

to determine an appropriate value of ρ from the data. However, the data

are roughly as comparable in correlation to the Eilenberger theory as

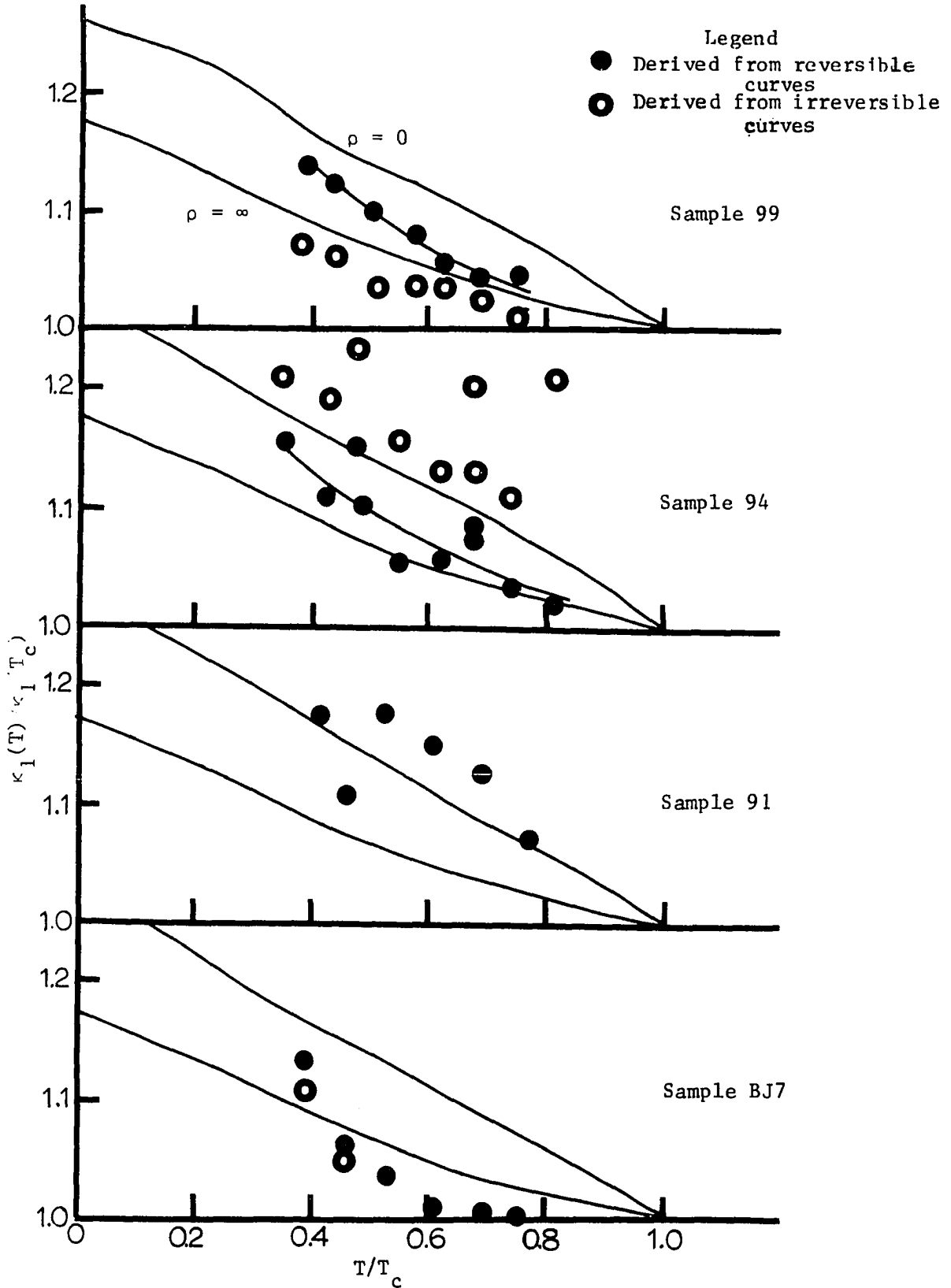that of Usui et al (88), Trojnar (96), and Fischer (26). Ikushima and

Fig. 29. $\kappa_1(T)$ as a function of temperature. $\kappa_1 = H_{c_2}/\sqrt{2}\,H_c$.

Mizusaki (66) found considerably higher values of $\kappa_1(T)/\kappa_1(T_c)$ than the predictions of the theory for most of their Nb-Ta alloys.

In summary, we find discrepancies between κ_1 and κ_4, which may be resolved using the Farrell (90) technique. The data for the present alloys agree only partially with the Eilenberger theory.

Ginzburg-Landau Parameter κ_2

It has been shown that (97)

$$\kappa_2(T_c) = \kappa_1(T_c) \tag{7.7}$$

where κ_2 is defined by Eq. (2.7): $-4\pi(dM/dH) = \{1.16(2\kappa_2^2 - 1)^{-1}\}$. Since the experimental values of κ_2 change comparatively little in the present alloys, we shall accept Eq. (7.7) as the normalizing factor for $\kappa_2(T)$.

Eilenberger's (81) work also includes the variation of $\kappa_2/\kappa_1(T_c)$ with temperature and impurity parameter. As noted in Fig. 30, the value of $\kappa_2/\kappa_1(T_c)$ as $T \to 0$ is considerably larger than $\kappa_1/\kappa_1(T_c)$ (see Fig. 29), for the pure limit ($\rho = 0$). However, most experimental data is taken in the dirty limit, where $\kappa_2(T) \simeq \kappa_1(T)$ fairly closely. This point will be discussed later.

In discussing Fig. 30, we note first that the scale for the ordinate of the penultimate section is twice that of the others. The bulk of the comments on Fig. 29 are applicable here as well. While the data points cannot be used to determine ρ, they generally fall in the region of high ρ, as would be expected physically.

In the light of the two preceding graphs, it seems apparent that obtaining the GL parameters from the fitted reversible curves is more accurate physically than obtaining them from the raw irreversible curves,
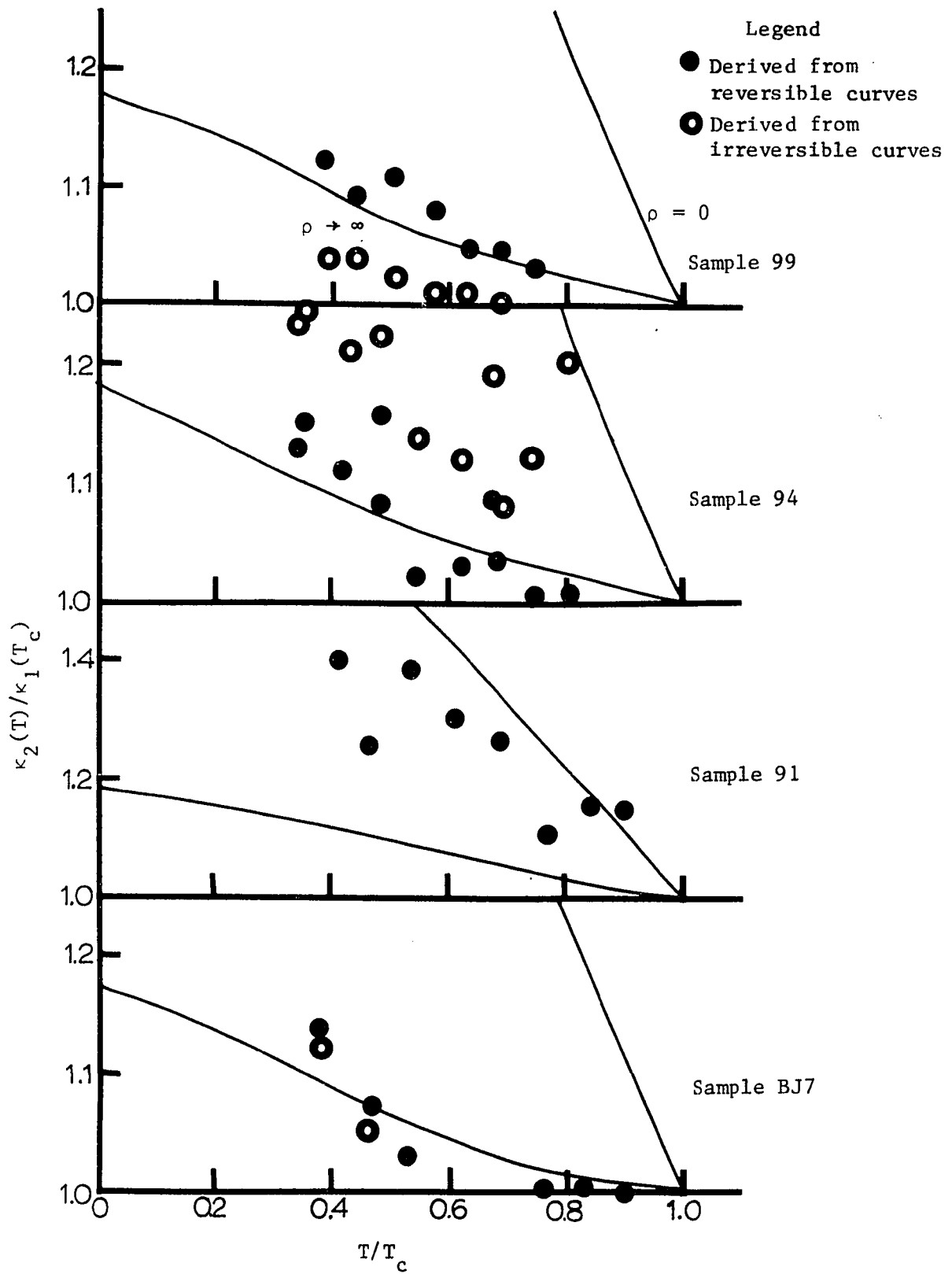
Fig. 30. $\kappa_2(T)$ as a function of temperature

as has been done in the past.

The relative magnitude of $\kappa_2(T)$ with respect to $\kappa_1(T)$ has been disputed. Recently, Evetts and Wade (98) found that $\kappa_2 > 0.92\,\kappa_1$ in Pb-Bi and Pb-In alloys, for all temperatures. However, Zoller and Dillinger (22) found that κ_2 is about 7 - 8% less than κ_1 in an In-Pb alloy. The two statements are consistent only if $\kappa_2 = 0.92\,\kappa_1$. It has been also shown theoretically (99) that $\kappa_2(t) = \kappa_1(t)$ to within 2% for all values of t.

An examination of Figs. 29 and 30 will show that for the present alloys, $\kappa_2(t) \simeq \kappa_1(t)$. To put the matter on a more quantitative basis, we define

$$y^2 = (1/n) \int_{}^{n} \left| \kappa_1(t)/\kappa_2(t) \right|^2 \qquad (7.8)$$

where n is the number of data points. This procedure ensures the normalization of y. In Eq. (7.8), the summation is over all temperatures for a given sample. Results are presented in Table 12 and Fig. 31.

An interesting phenomenon may be observed in the data. The normalized value of $\kappa_1(t)/\kappa_2(t)$ ($\equiv y$) is close to 1 at both ends of the fcc phase we are discussing, for data derived from both the reversible and irreversible curves. The quantity $y_{irrev.}$ declines negligibly from 1.0 at the center of the fcc phase. The decline is within the theoretical 2 - 3% mentioned by Saint-James (99). However, we see a large decline in $y_{rev.}$ at the center of the phase.

Part of the data of Fig. 31 is presented for representative samples in Fig. 32. The results are in substantial agreement with those of the former graph. For low Cd concentrations, the ratio κ_1/κ_2 is within a few percent of 1.0 for both irreversible and reversible data, for
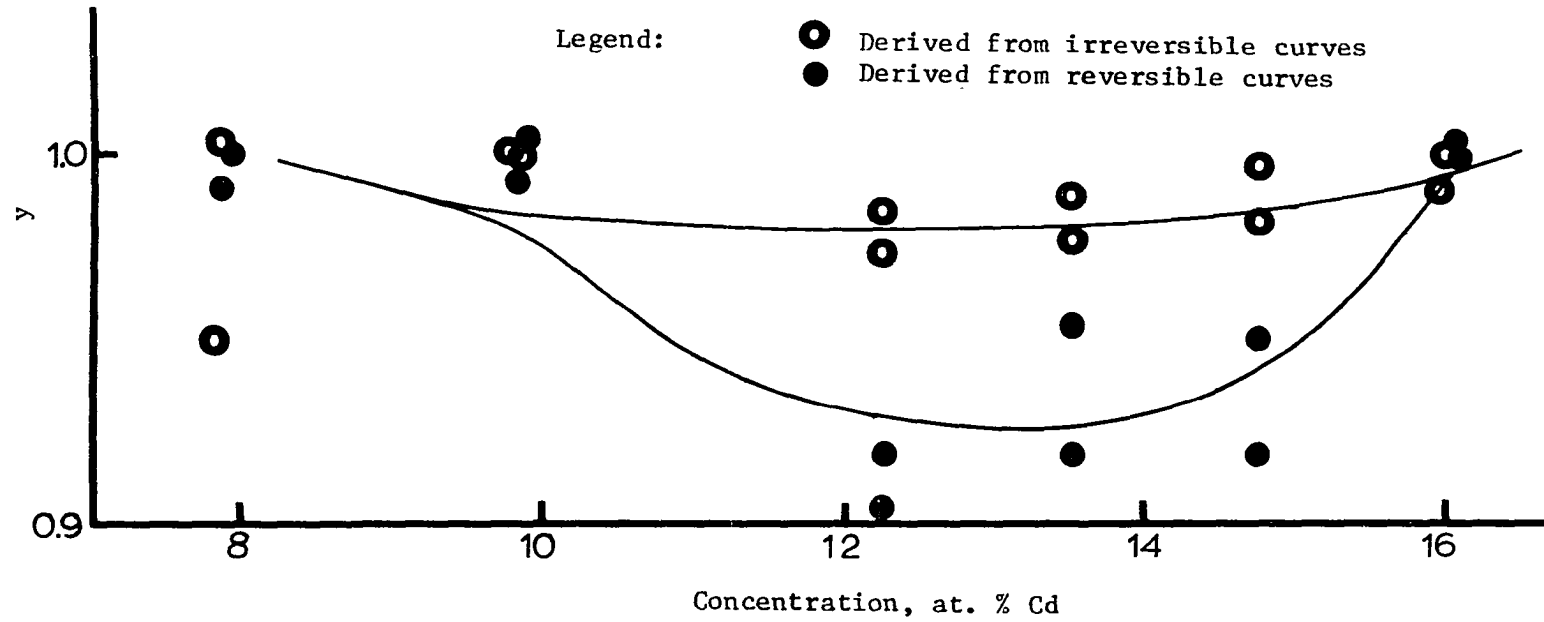
Fig. 31. Normalized value of $\kappa_1(T)/\kappa_2(T)$ as a function of concentration
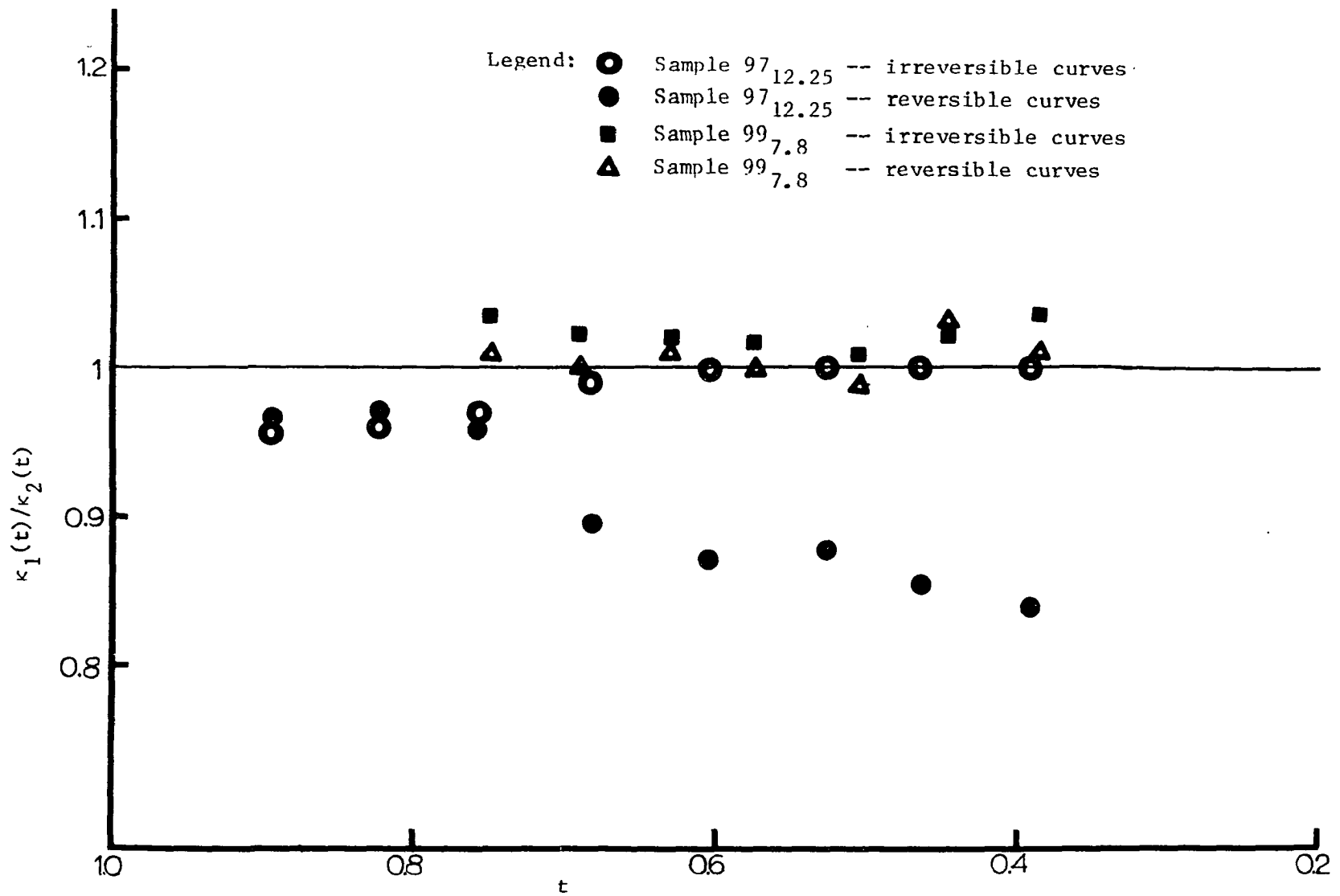
Fig. 32. $\kappa_1(t)/\kappa_2(t)$ as a function of t.

all values of t. However, for the middle range of concentrations (illustrated by sample $97_{12.25}$), the irreversible values of the ratio tend to remain close to 1.0, whereas the reversible values diminish with t. The latter case will produce a value of y < 1.0, shown in Fig. 31.

This behavior may be the explanation of the divergent results noted in the literature. If the irreversible data is used, then (assuming y is a valid measure of the averaged behavior of κ_1/κ_2) the data agrees with the theoretical conclusions of Saint-James (99). However, the reversible data (at a Cd concentration of about 12 - 14 at. %) agree with the data of Zoller and Dillinger (22), and, to a lesser extent, that of Evetts and Wade (98). Thus we see that the use of irreversible curves can lead to large differences.

The precise reason for the difference in behavior of the normalized ratio y within one phase must await an extended metallurgical investigation. However, we have previously noted the changes in many superconducting parameters in the center of the fcc phase as compared to the extreme limits, and this phenomenon is apparently another.

To summarize, for the reversible curves we have $\kappa_2(t) \simeq \kappa_1(t)$ for both ends of the fcc phase, and $\kappa_2(t) \gtrsim \kappa_1(t)$ at the center. We have $\kappa_2(t) \simeq \kappa_1(t)$ for all concentrations for the irreversible curves. The ratio κ_1/κ_2 will thus be close to or less than 1.0 depending on the degree of irreversibility, accounting for the contradictory results in the literature.

Penetration Depth λ

The penetration depth of the magnetic field in Type II super-

conductors, $\lambda(t)$, was shown to be (2)

$$H_{c_2}(t) = 4\pi \, \lambda^2(t) \, H_c^2(t)/\phi_o \qquad (7.9)$$

The penetration depth at 0 K may be calculated from this and

is presented in Table 13 and Fig. 33. We see that the maximum pene-

tration depth at 0 K is around 13 - 14 at. % Cd.

The penetration depth $\lambda(t)$ can also be calculated for $t \neq 0$.

The Gorter-Casimir (100) two-fluid model of superconductivity predicts

$$\lambda(t) = \lambda(0)(1 - t^4)^{-\frac{1}{2}} \qquad (7.10)$$

This prediction is borne out in Fig. 34. The data from only two samples

are shown for clarity of presentation. However, all samples showed the

same general behavior. At low temperatures $(\{1 - t^4\}^{-\frac{1}{2}} \leq 1.1)$, $\lambda(t)$

shows a negative deviation from the above relationship. This has been

explained by BCS theory (101).

The coherence range ξ, a measure of the distance to which a

perturbation in the order parameter spreads from its center, is given

by (102)

$$\xi(t) = \{\phi_o/2\pi \, H_{c_2}(t)\}^{\frac{1}{2}} \qquad (7.11)$$

The coherence range at 0 K may be calculated and is shown in Table 13

and Fig. 33. The table indicates a change in slope around 12 at. % Cd,

although this is not apparent in the graph due to the scale employed.

Energy Gap $\Delta(0)$

The energy gap at 0 K, $\Delta(0)$, is given by the BCS expression (115)

$$2 \, \Delta(0)/kT_c = \{2\pi \, H_c^2(0)/3\gamma \, T_c^2\}^{\frac{1}{2}} \qquad (7.12)$$

This equation applies, strictly speaking, only to superconductors of

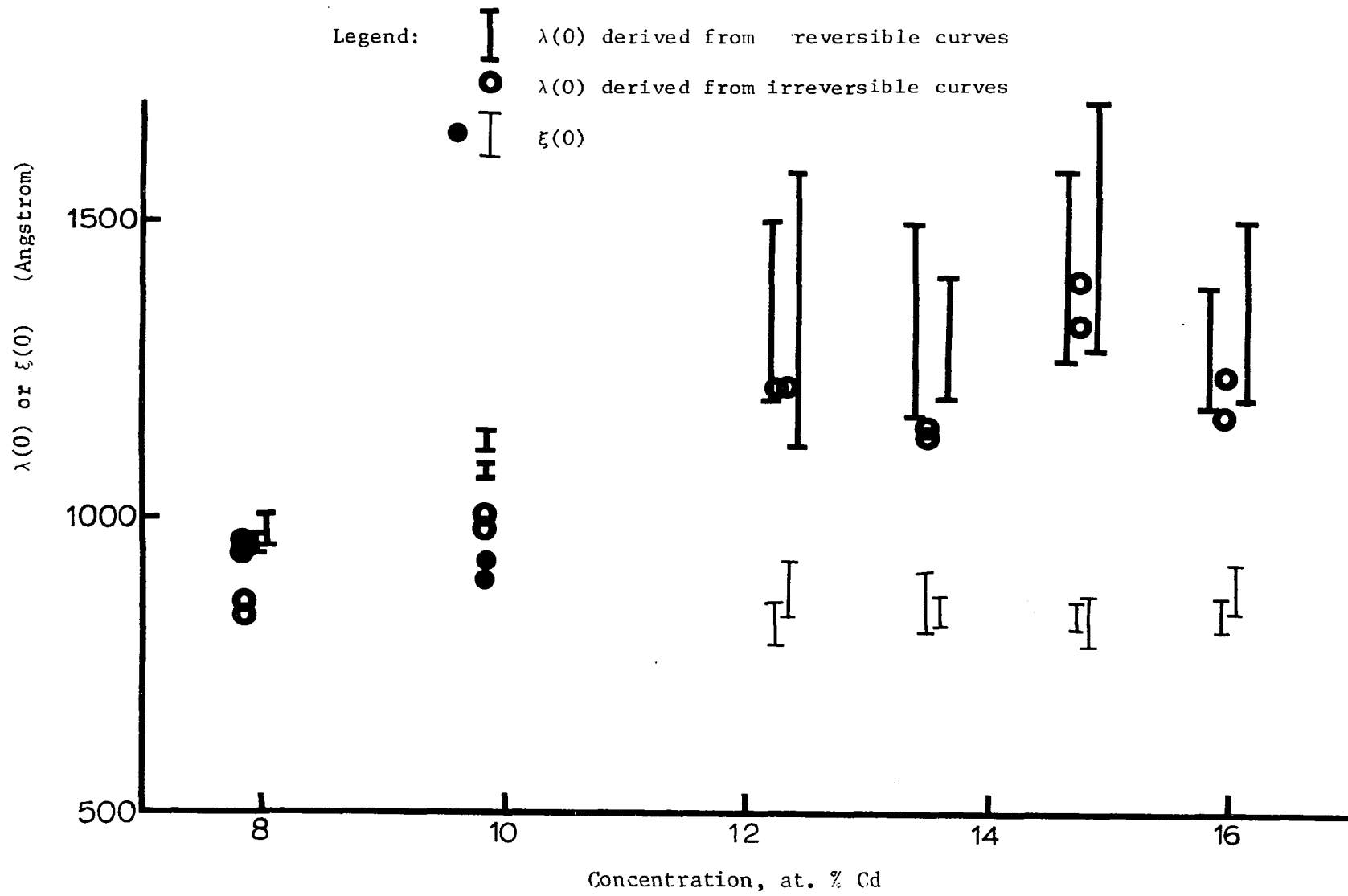very low coupling strength $N(0)V$. However, it is derived from the same

Fig. 33. Penetration depth λ and coherence range ξ at T = 0 K as a function of concentration.
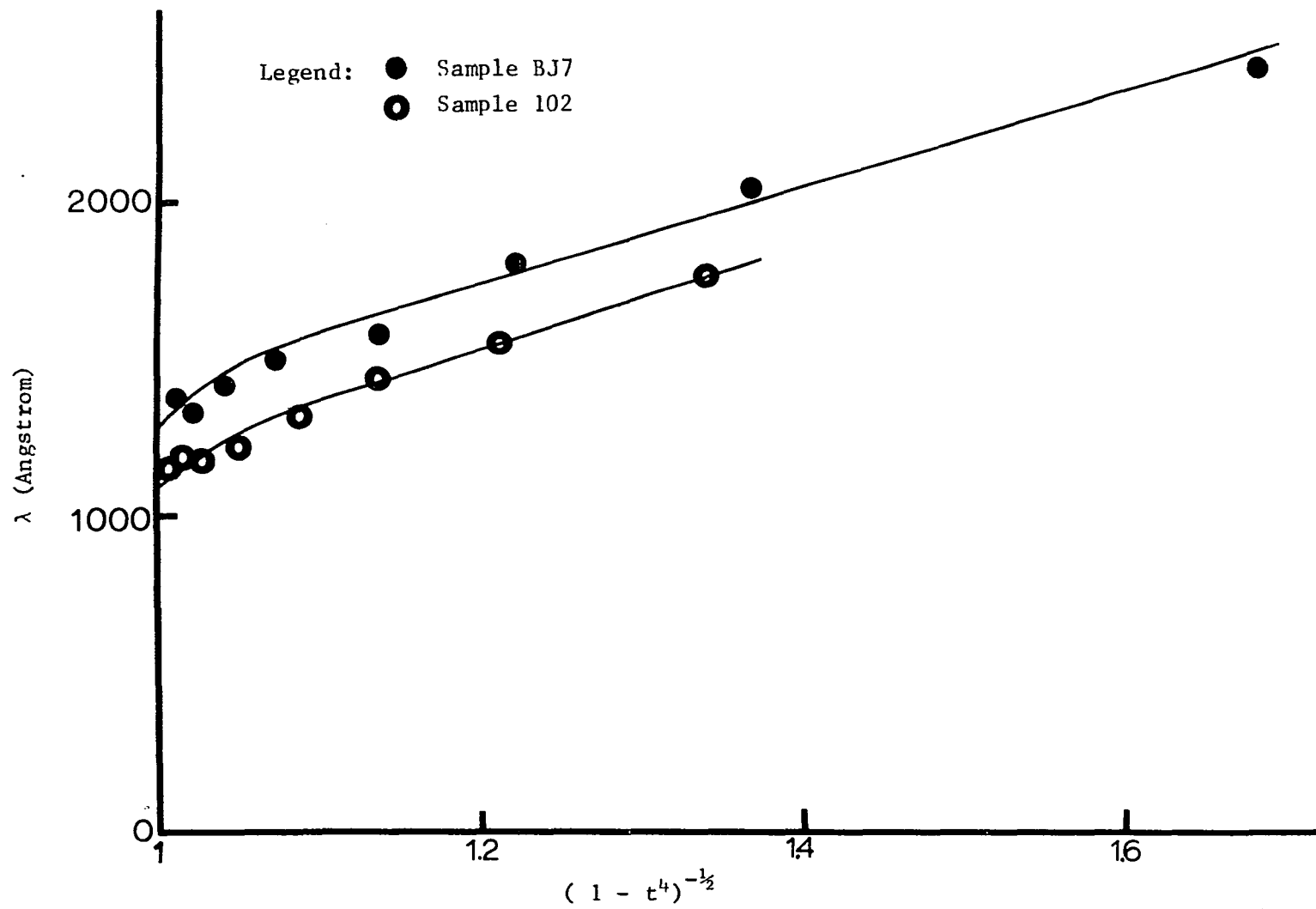
Fig. 34. Penetration depth λ as a function of Gorter-Casimir parameter $(1 - t^4)^{-\frac{1}{2}}$.

assumptions used in deriving Eq. (2.2). Since the latter equation has been used to find the values of $N(0)V$ in alloys (which often have stronger coupling than pure elements), Eq. (7.12) will be used to find values of the reduced energy gap (the left hand side of Eq. (7.13)) in the present alloys.

If the BCS relation $\gamma^{\frac{1}{2}} = 0.41\ H_c(0)/T_c$ (Eq. 6.6a)) is used in Eq. (7.12), we obtain

$$2\ \Delta(0)/k\ T_c = 3.52 \tag{7.13}$$

However, if the thermodynamically derived relationship for γ as contained in Eq. (6.11) and (6.13) is used,

$$2\ \Delta(0)/k\ T_c = 3.52(1 - D_0\pi)^{\frac{1}{2}} \tag{7.14}$$

Values of the reduced energy gap found by using D_0 in Table 5 are shown in Table 13. Most of the points are above the BCS value of 3.52. If this is a real effect, the explanation is suggested by the work of Swihart et al (92), who calculated the ratio $2\ \Delta(0)/k\ T_c$ for realistic phonon spectra of strong-coupling superconductors, and found increases of up to 35% for Hg, for example. If the discussion following Eq. (6.4) is recalled, in which it was pointed out that these alloys were midway between weak- and strong-coupling superconductors, this fact will explain the increase in the ratio $2\ \Delta(0)/k\ T_c$. In fact, if the original equations of the BCS theory modified for medium-coupling superconductors are used (116), these superconductors will have a theoretical value of the reduced energy gap higher than weak-coupling superconductors. However, this increase cannot as yet be put on a quantitative basis.

Helfand-Werthamer Parameter h*

Helfand and Werthamer (H-W)(94) have defined a parameter

$$h^*(t) = -H_{c_2}(t)/(dH_{c_2}(t)/dt)\big|_{t = 1} \qquad (7.15)$$

If Eq. (7.2) is substituted into Eq. (7.15) and rearranged,

$$h^*(t) = 0.5\ H_{c_2}(t)/(1 - \pi\ D_{o_2})H_{c_2}(0) \qquad (7.16)$$

This quantity has a slope of -1 at t = 1. Typical results for alloys with low concentrations of Cd are shown in Fig. 35. The values of D_{o_2} from Table 11 were used. The agreement with the H-W curves are only fair; as in the discussion of the Eilenberger theory, the value of ρ cannot be determined from the data. However, the data lie on the high ρ side.

As the concentration of Cd rises, the variation of $H_{c_2}(t)$ with temperature changes and thus the shape of h*(t) also changes. The value of h*(t) is close to the H-W curves for t → 1 and is below the curves for t → 0. The situation may be summarized by the presentation of h*(0) in Table 13. The agreement with the calculated curves is poor for the higher concentrations of Cd, since the H-W theory requires h*(0) = 0.73. However, other authors (107) also find disagreement with the theory. The reason for the discrepancy between theory and experiment may be due to a correlation between h*(0) and the electron-phonon coupling strength λ as discussed by Werthamer and McMillan (108), as h*(0) can be shown to roughly increase with λ (from Table 5).

Upper Critical Field H_{c_2}

The problems involved in finding H_{c_2} exactly have been discussed above. In this section only typical results are presented, as $H_{c_2}(t = 0)$
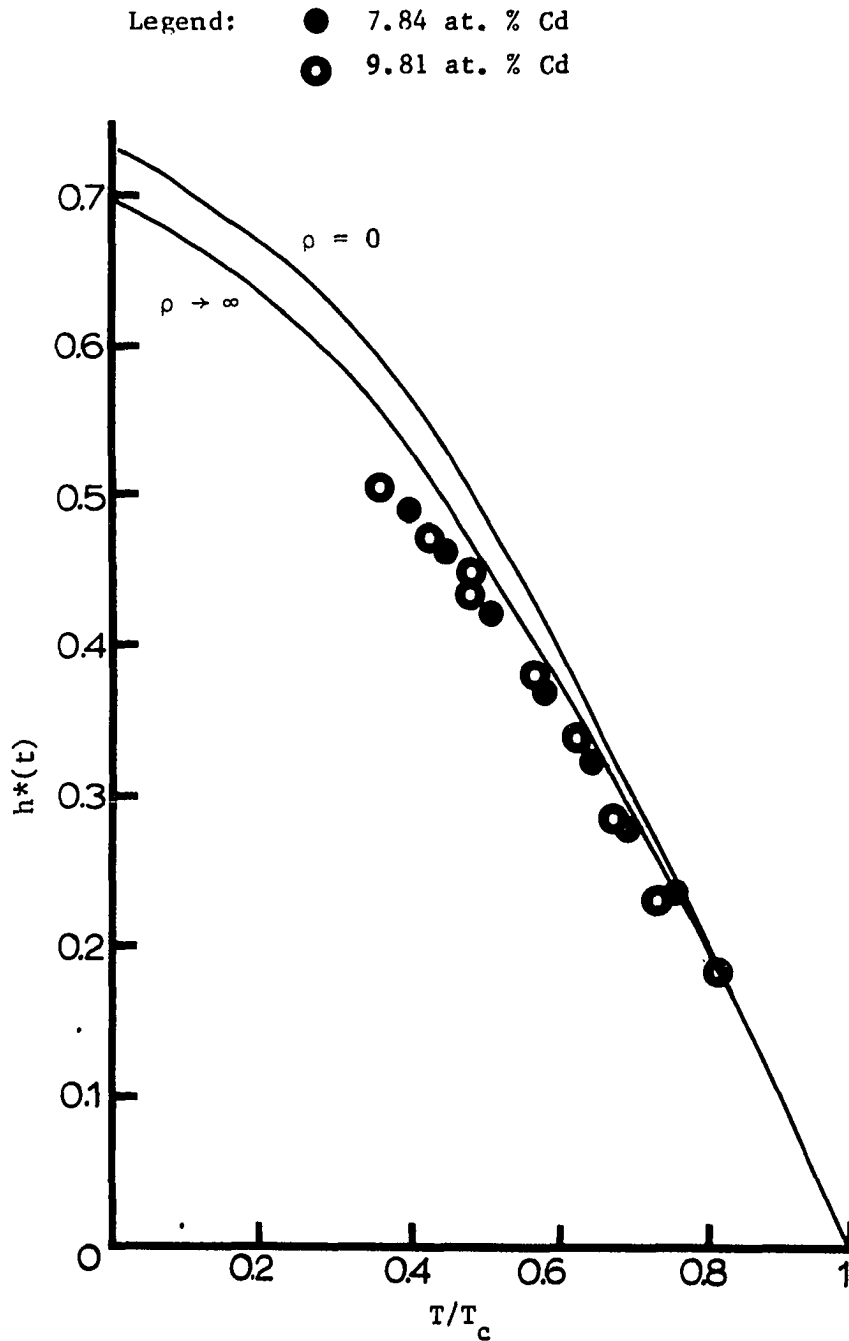
115

Fig. 35. Helfand-Werthamer parameter h*(t) as a
function of t.

and H_{c_2} (t = 1) may be easily calculated, from Eq. (7.2) and a least-squares method. Typical results are shown in Fig. 36.

One difference between the behavior of H_{c_2}(t) for alloys of low Cd concentration and of high Cd concentration may be observed. The former points go linearly to zero as t → 1, whereas the latter points are non-linear in this vicinity. However, from limited data collected at t ≥ 0.9, and of course from theory as well, H_{c_2}(t) → 0 as t → 1. This behavior provides a "kink" in the ordinarily fairly straight line of H_{c_2}(t) versus t^2. The discussion may be put on a more quantitative basis by considering D_{o_2} of Eq. (7.2). This quantity is small and positive for the four alloys with the lowest Cd concentration, and is large and negative for the eight alloys with higher Cd concentration (with one exception).

The reason for this behavior is unknown, although Ogasawara et al (89) have displayed graphs of H_{c_2}(t) versus t^2 (for Nb-Ta alloys) which appeared to be made up of two connecting straight lines. Since the alloys with higher Cd concentrations are less stable metallurgically (due to their phase diagram), one possibility might be a non-fcc phase in these alloys which dominates the superconducting characteristic near t = 1. There is little chance that the temperature measurement was at fault, as the measured T_c agrees quite closely with those of Merriam (see Fig. 22).

Lower Critical Field H_{c_1}

As previously mentioned, the problem of irreversibility enters into the determination of H_{c_1}. In Fig. 37, only the variation of H_{c_1}(t)
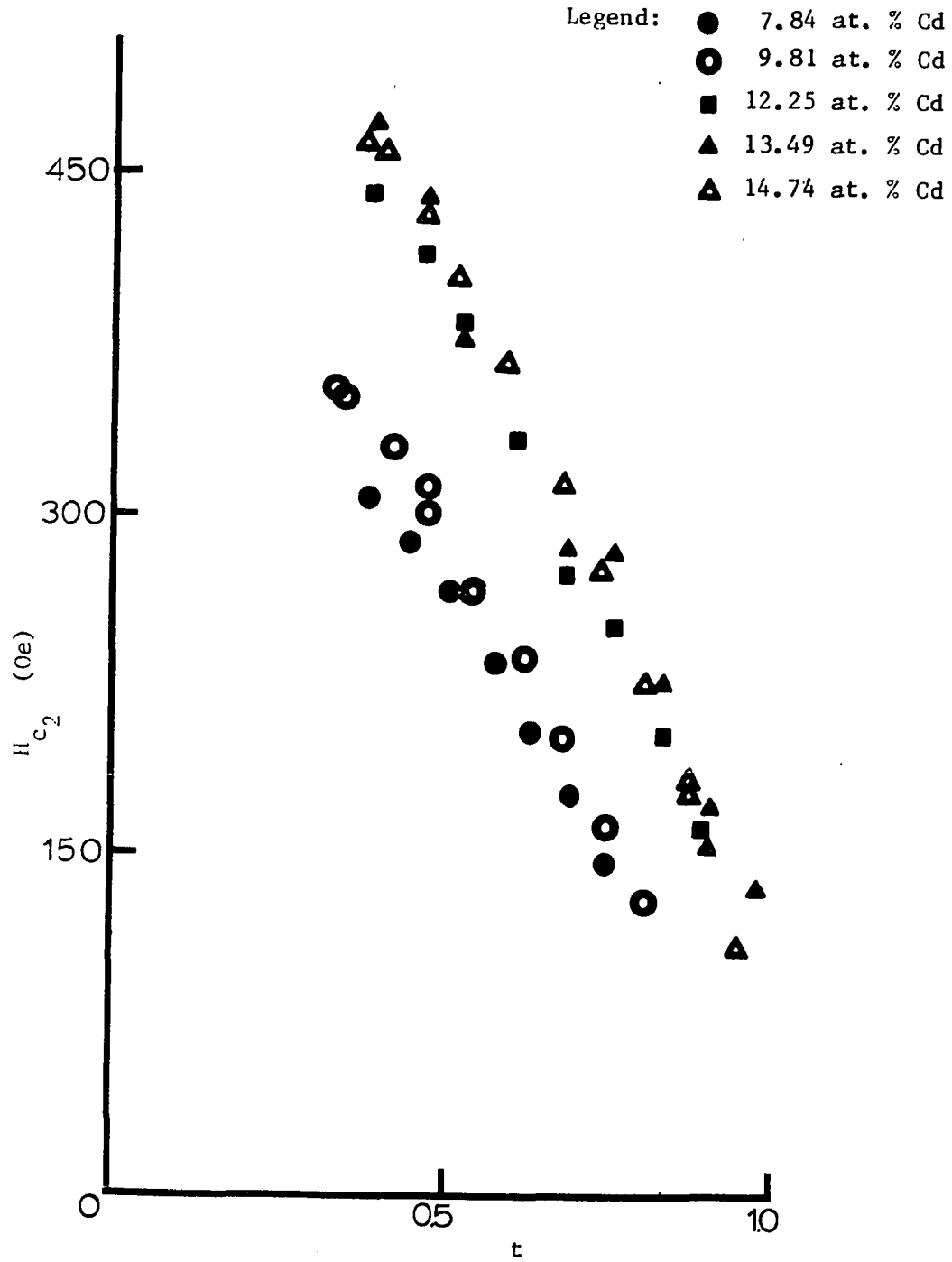
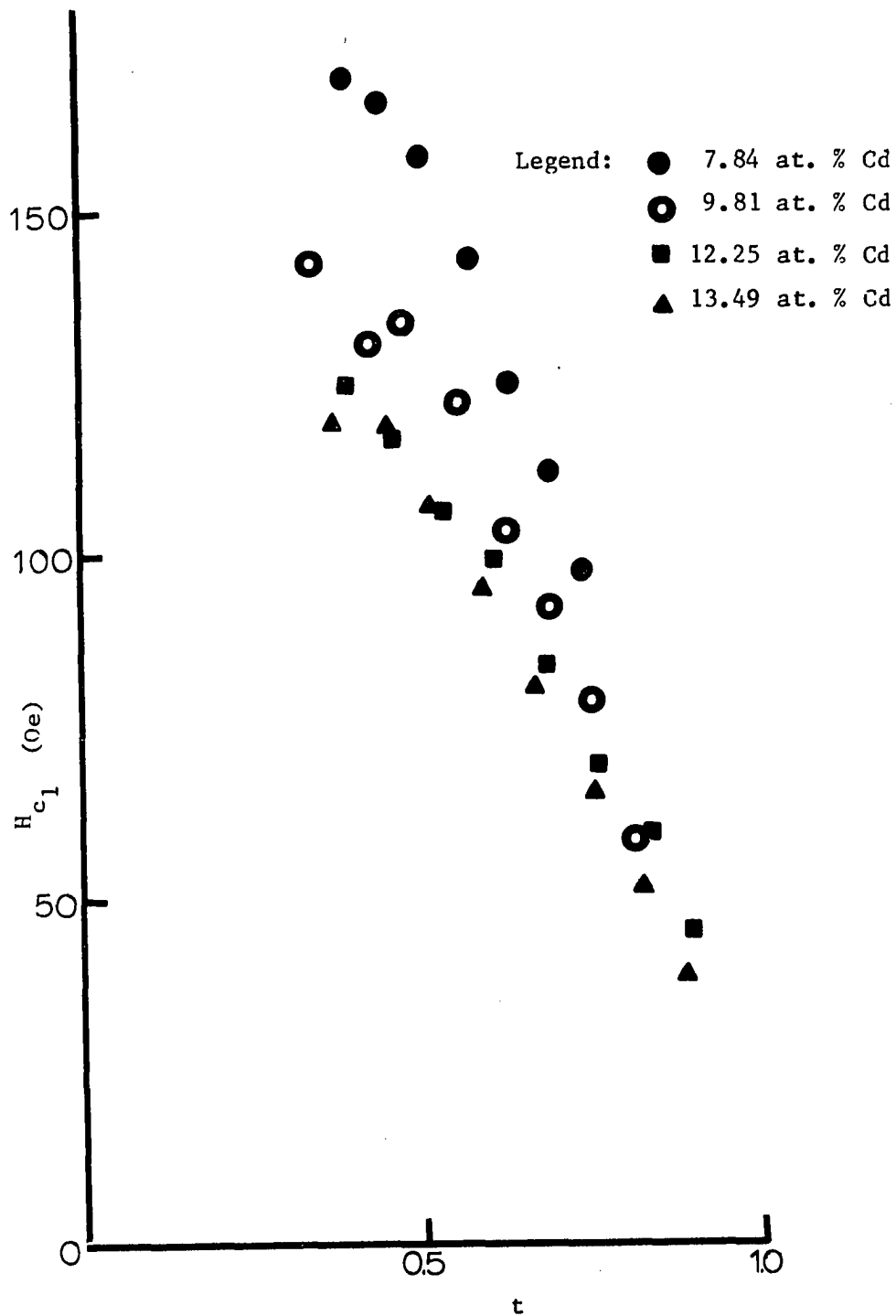Fig. 36. Upper critical field H_{c_2} as a function of reduced temperature t.

Fig. 37. Lower critical field H_{c_1} as a function

of reduced temperature t (derived from
reversible curves).

as found by the method described in Chapter V is shown.

As might be expected from Fig. 25, where $H_{c_1}(0)$ is found to vary little with concentration above 10 at. % Cd, similar results are found in Fig. 37. The values of $H_{c_1}(t)$ lie fairly close for most concentrations above 10 at. % Cd.

As in Fig. 36, non-linearity occurs at higher concentrations of Cd as $t \to 1$; however, it is considerably smaller in magnitude as compared to $H_{c_2}(t)$. Since the measured quantities $H_{c_2}(t)$ and $H_{c_1}(t)$ are related by the GL parameters, presumably the discussion in the previous section is applicable. $H_{c_1}(t)$ in the light of the GL parameter κ_3 will be discussed shortly.

Ginzburg-Landau Parameter κ_3

Harden and Arp (109) suggested another Ginzburg-Landau parameter κ_3, relating H_{c_1} and H_c. The relationship may be put into the form

$$\kappa_3(t) = 0.717 \{H_c(t)/H_{c_1}(t)\}^{1.68} \tag{7.17}$$

The relationship may be derived from the original GL differential equations as presented by Abrikosov (4), in terms of an isolated normal filament, and was found by numerical integration of the equations. The region of temperature over which Eq. (7.17) is valid is unknown. Ogasawara et al (89) assumed that $\kappa_1(t) \simeq \kappa_3(t)$ for all t, and calculated values of $H_{c_1}(t)$, using experimental values of $H_c(t)$ and $\kappa_1(t)$. A similar plot is shown in Fig. 38. The values of $H_c(t)$ were obtained from the reversible curves.

The values of $H_{c_1}(t)$ calculated from Eq. (7.17) and its accompanying assumptions produce $H_{c_1}(t)$ slightly higher than the experimental
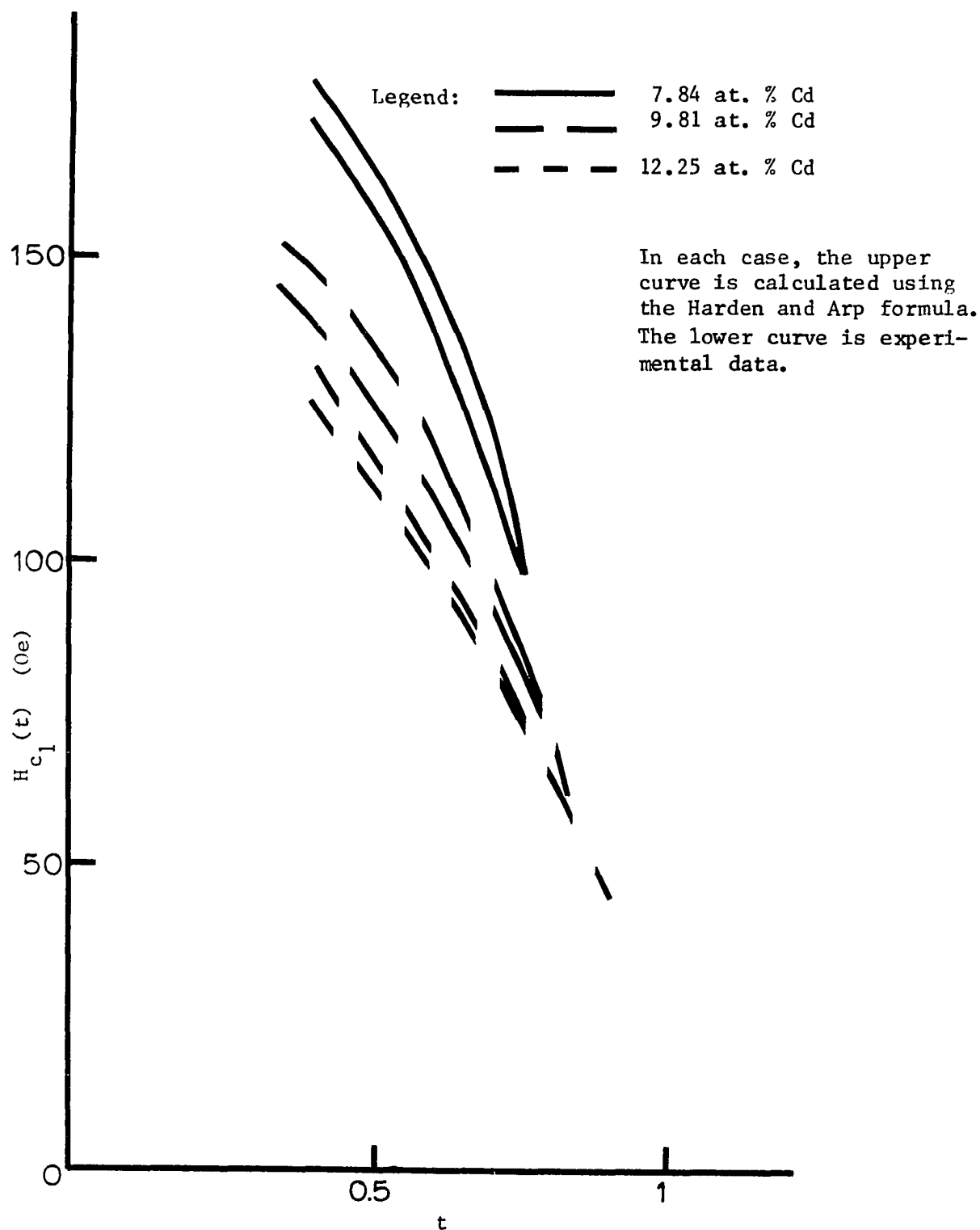
Fig. 38. Experimental and theoretical dependence of critical field H_{c_1} (t). Theoretical dependence is calculated using Harden and Arp theory and $\kappa_1 \simeq \kappa_3$.

value. Furthermore, this increase tends to disappear as $t \to 1$. This is in line with the conclusions of Eastham (110), who stated that the Harden and Arp formulation was valid primarily near $T = T_c$.

Fig. 38 shows that the difference between the theoretical and experimental values of $H_{c_1}(t)$ are also probably related to composition and thus the impurity parameter ρ. Neumann and Tewordt (111) constructed a modification of κ_3 valid to order $(1 - t)$ for various values of ρ. However, the corrections introduced by ρ are only of the order of a few percent. The formulation of $\kappa_3(t)$ for all values of t and ρ remains to be accomplished.

Evetts and Wade (98) found that their values of $H_{c_1}(t)$ fitted by the above procedure were lower than the experimental values in Pb-In alloys. However, their differences were considerably larger than in the present work, ranging up to 28%.

The apparent coincidence of the experimental value of $H_{c_1}(t)$ and that calculated by Eq. (7.17) as $t \to 1$ bears out the prediction of Serin that $\kappa_3(1) = \kappa_2(1) = \kappa_1(1)$ (112). Serin subsequently predicted (p. 936) that for dirty superconductors, which the present samples are,

$$\kappa_3 > \kappa_1 \simeq \kappa_2 \qquad (7.18)$$

which is borne out in all the present samples, as deduced from Fig. 38. Thus the work of Evetts and Wade apparently does not agree with Eq. (7.18).

The results of Fig. 38 are not borne out with respect to Serin's first prediction at $t \to 1$, noted above, if data from the irreversible curves are used. This point is illustrated in Fig. 39. For the four
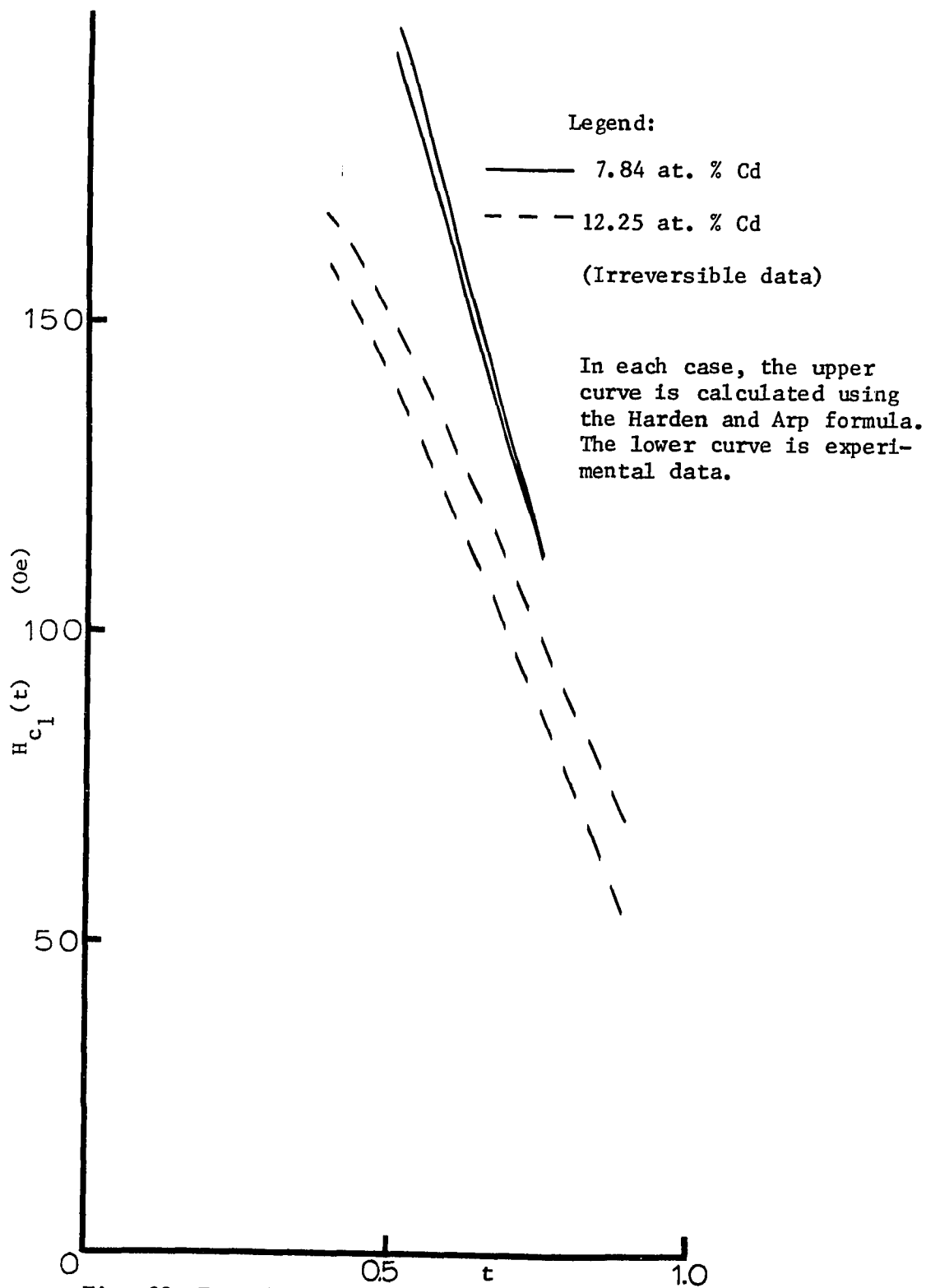
Fig. 39. Experimental and theoretical dependence of crit-
itical field H_{c_1} (t) for irreversible data. Theoretical de-
pendence calculated using Harden and Arp formula and $\kappa_1 \simeq \kappa_3$.

samples lowest in Cd concentration, the variation of theoretical and experimental values of H_{c_1} follows that of Fig. 38. However, for all samples with higher Cd concentrations, the theoretical (derived from Eq. (7.17)) and experimental values of H_{c_1} do not converge as $t \to 1$. This behavior is illustrated by the sample with 12.25 at % Cd. Thus again the irreversible data provides results inconsistent with theory.

Eq. (7.18) may be illustrated by means of Fig. 40. The relationship of κ_1 and κ_2 has already been discussed, so these data are not presented here. For this representative sample $\kappa_3 > \kappa_1$ for both the reversible and irreversible curves. The non-linear phenomenon mentioned in the discussion of $H_{c_2}(t)$ can be noticed here as it tends to increase the value of $\kappa_3(t)/\kappa_1(t)$ as $t \to 1$. This phenomenon is much less pronounced for the reversible data.

It should be noted that the above results show that the procedure used in finding $H_{c_1}(t)$ (i.e., that outlined in Chapter V) appears to be valid to within a few percent.

An approximation to the variation of $\kappa_3(t)$ with t can be made from the present work, for low values of $\kappa_1(T_c)$. Maki (9) has performed this work for $\kappa_1(T_c) \gg 1$ theoretically. Representative results are shown in Fig. 41.

A least-squares straight line was drawn through each of the set of data points for simplicity, although as mentioned above $\kappa_3(t)$ has yet to be determined in general theoretically. However, the intercept at $t = 1$ is very close to 1, in accordance with Serin's predictions. Furthermore, the value of $\kappa_3(T_c)/\kappa_1(T_c)$ at $0.3 < t < 1$ is greater than $\kappa_1(t)/\kappa_1(T_c)$ from Eilenberger's curves (see Fig. 29), confirming, in
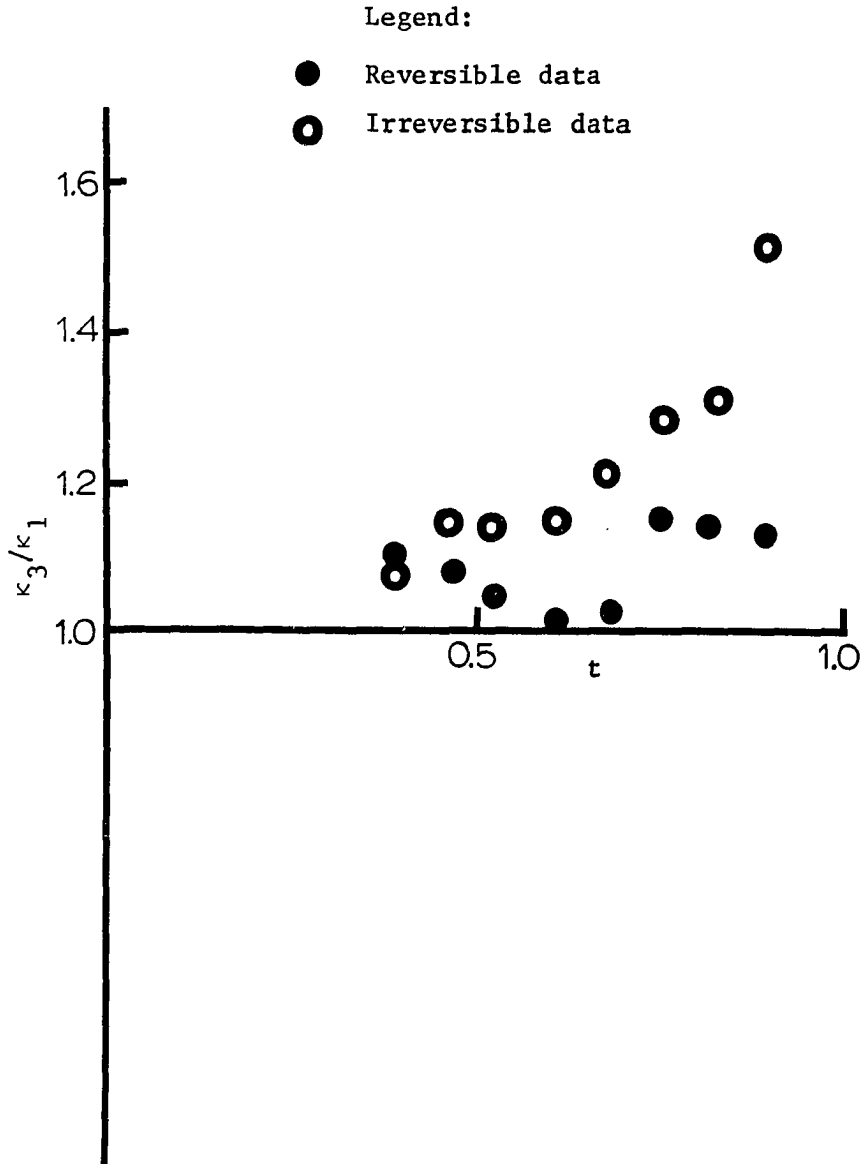
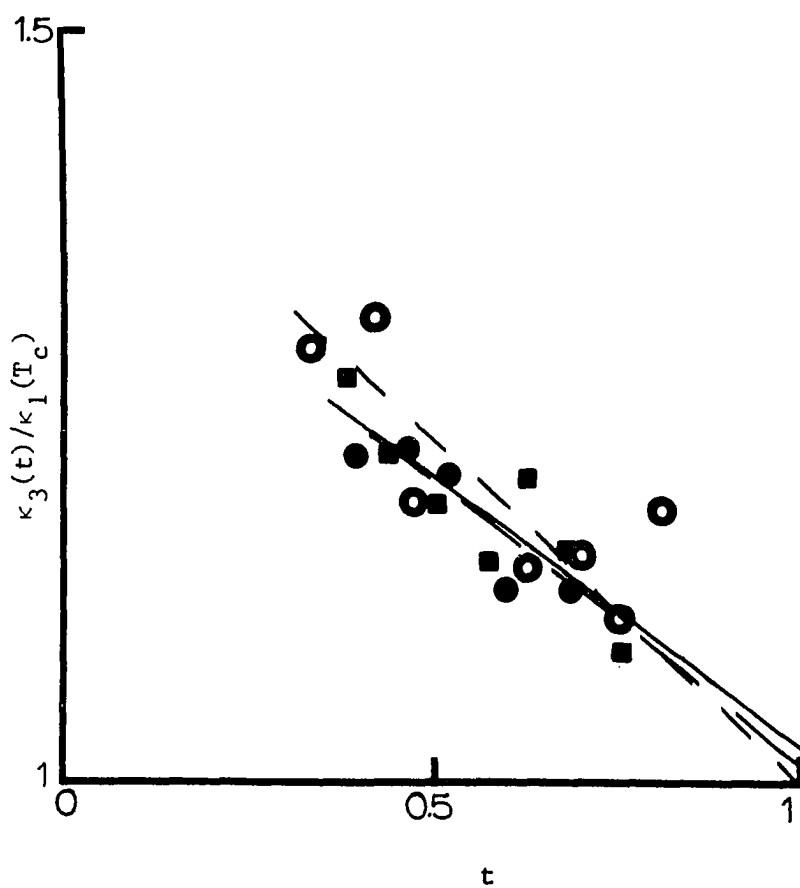Fig. 40. Variation of $\kappa_3(t)/\kappa_1(t)$ with reduced temperature t. Sample $97_{12.25}$.

Fig.41. $\kappa_3(t)/\kappa_1(T_c)$ as a function of reduced temperature.

part at least, Eq. (7.18).

To summarize, $H_{c_1}(t)$ computed by using $\kappa_3(t)$ approaches the experimental value as $t \to 1$, and is greater than that value for all t, as required by theory. $\kappa_3(t)$ was plotted as a function of t, and its general shape also agrees with theory.

Flux Trapping

The various imperfections inside a superconductor can trap flux in a magnetic field by creating regions with anomalously high critical fields. If the applied field which drives the superconductor normal is reduced, any multiply-connected inhomogeneous regions will trap the flux which threaded them at the moment of their transition back into superconductivity. As the field is then reduced to zero, this trapping will become apparent in the form of a positive magnetization at zero applied field.

As mentioned in Chapter III, one of the main methods of determining the homogeneity of an alloy is considering the magnitude of this trapped flux. In general, the samples in this study were found to have low values of trapped flux for Type II superconductors.

Another method of measuring the amount of inhomogeneity by means of the hysteretic magnetization curves is the ratio of the areas under the curves in the forward and reverse directions. Since this has not been discussed theoretically, the matter will not be pursued further.

Livingston and Schadler (14) note that there have been few systematic studies of the effect of defects on flux trapping. However, Budnick et al (114) found that regardless of the annealing times, the

trapped flux ratio (tfr) varied linearly with $(1 - t^4)^{-\frac{1}{2}}$, where t is

the reduced temperature. In Fig. 42, we present representative data on

the tfr for various Cd concentrations. The ratio tends to follow the

Budnick rule. Budnick defined

$$tfr = |4\pi\ M|/4\pi\ M_{max},$$

where $|4\pi\ M|$ is the actual trapped flux, and $4\pi M_{max}$ is the maximum value

of magnetization for the entire range of applied field.

As might be expected from the metallurgy, the tfr is higher

for the alloys with higher Cd concentration. However, it is difficult

to draw any quantitative conclusions concerning the correlation of the

slopes or the intercepts of the lines in Fig. 42 with concentration.

The trapped flux will always be sensitive to sample handling and

preparation.

Jurisson and Oakes (113) prepared a simple theory of the varia-

tion of tfr with temperature. We have rough qualitative agreement with

the Jurisson theory on the basis of Fig. 42; quantitative agreement

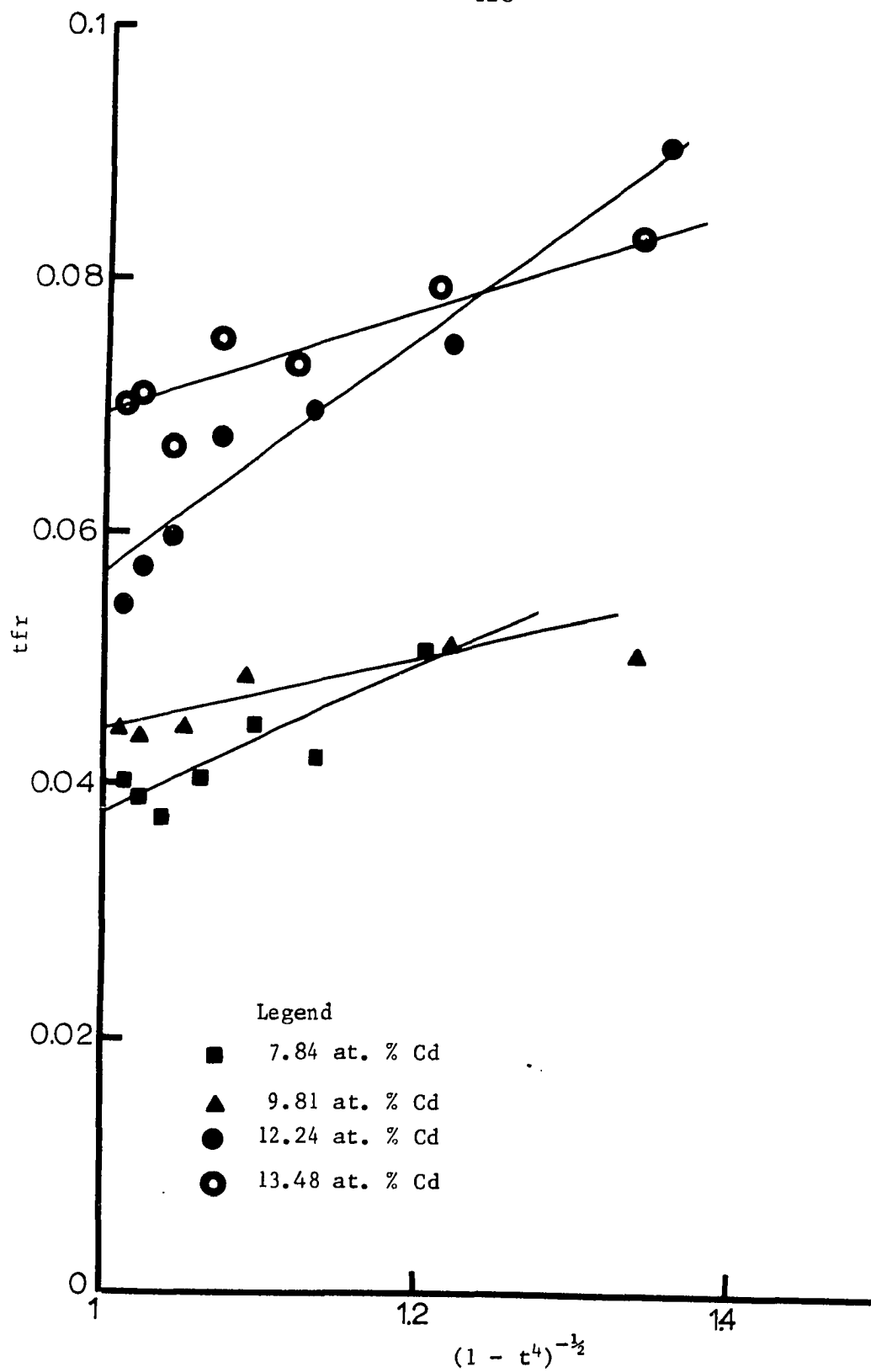might be achieved with appropriate adjustment of the parameters in their

theory.

Fig. 42. Trapped flux ratio as a function of $(1 - t^4)^{-\frac{1}{2}}$.

CHAPTER VIII

CONCLUSIONS

This chapter will be composed of two parts: one dealing with
the theoretical aspects of this work, and one dealing with the experi-
mental aspects.

Theoretical Conclusions

Theories of superconductivity are based on the reversibility
of the magnetization curve. However, the majority of Type II super-
conductors have at least some hysteresis, thus making comparison of
the Ginzburg-Landau parameters derived from the curves difficult, if
not invalid. A number of theories of hysteresis in superconductors have
been proposed, with "reversible" curves lying between the forward and
reverse curves.

Prime among these have been the theories of Campbell et al (37)
and Silcox and Rollins (39). These theories give at least a qualitat-
ive fit to experimental data.

The theories can be checked on a quantitative basis by using
the results of Goedemoed et al (33) for which irreversible and revers-
ible experimental curves (for the same superconductor) are available.
The fit to these experiments is inadequate.

In this thesis, a theory has been devised to give a better

129

fit to these data. Essentially, the theory consists of two modificat-
ions to the Silcox and Rollins theory. Firstly, the long range effects
of the fluxoid-fluxoid interactions were taken into account, using a
model based on work of Melville and Taylor (41). Secondly, an ad hoc
reversible curve was devised which fits the theoretical reversible
curve of Abrikosov (4) over different regions of applied field better
than the ad hoc curves of Campbell et al and Silcox and Rollins.

The latter point may be seen in Figs. 14 and 15 and the dis-
cussion following Eq. (5.11a). In general, we have good agreement with
the reversible curves of Abrikosov.

However, we wish as well to have quantitative agreement with
typical experimental data. Excellent agreement was reached with the
previously published data of Goedemoed et al, shown in Figs. 18 and
19. In Table 1, we see that the least-squares fit to this data for
the present theory is an order of magnitude better than the Campbell
or Silcox theories. Furthermore, the present theory fits both the ex-
perimental reversible and irreversible curves well.

Although the present theory is somewhat more complicated than
some previously formulated, it still can be put in closed form and
graphs may be used to find the relevant parameters, as illustrated in
Figs. 20 and 21.

The main object of the hysteretic theory is to determine the
reversible curves from the experimental irreversible curves, as the
former are generally not known. We have found good agreement with the
data of Goedemoed et al in this respect, and we have used the theory
to find the reversible curves from the In-Cd experimental data.

To summarize, we have formulated a theory of hysteretic behavior in superconductors. This theory enables us to derive the equivalent reversible magnetization curves from the hysteretic irreversible curves. Good agreement is reached with experimental data.

Experimental Conclusions

The magnetization curves of the fcc phase of Cd in In have demonstrated Type II behavior. The samples ranged in concentration from 7.8 to 16.0 at. % Cd, and were annealed for periods of 5 - 47 days, before being quenched in liquid nitrogen.

The critical temperatures were found to have the same variation with concentration as the work of Merriam (67), i.e., a sharp dropoff from $T_c \simeq 3.4$ K at around 8 at. % Cd to a fairly constant $T_c \simeq 3.0$ K at concentrations $\gtrsim 12$ at. % Cd. The transition widths were smaller than those of Merriam, indicating more metallurgically homogeneous samples. The residual resistivity at 4.2 K was found by an indirect method for each sample. It rose almost linearly with concentration, but was consistently lower than the values of Fischer (26). This may be due to the shorter annealing times in the latter's work.

A number of physical quantities, such as the mean free path and the electron-electron interaction strength $N(0)V$ may be found from this data and the theory of Chapter II. Most of the calculated quantities have an extremum or change of slope around the concentration 12 at. % Cd. Based on the work of Merriam (67) on low concentration In-Cd alloys, this may indicate a Fermi surface-Brillouin zone interaction near that concentration. Since the Fermi surface is known only imperfectly for alloys, more work will have to be done to confirm this. This

could be done, for example, by using the method of Higgins and Kaehn (60) to determine the Fermi surface by the variation of critical temperature with pressure.

So far we have been discussing the superconducting properties which are non-hysteretic. In order to calculate the Ginzburg-Landau parameters, we need to know the various critical fields mentioned in Chapters I and II. If we have hysteresis, we can obtain inaccurate values for these quantities.

As mentioned in Chapter VII, we have used the hysteretic theory developed in Chapter V to find "reversible" values of the quantities used in finding the GL parameters. We shall show in the rest of this chapter that the reversible values found by this method agree with the appropriate theory better than the values from the raw or "irreversible" data.

In Fig. 24, we see that the reversible value of H_o varies less with concentration than does the irreversible value, and is considerably less erratic. The reversible values coincide with the diagram of the variation of H_o with concentration for two mutually soluble superconductors as presented by Livingston and Schadler (14), whereas the irreversible values do not.

The erratic behavior of the irreversible values of H_o produce erratic values of γ, the electronic coefficient of specific heat, as computed by the BCS Eq. (4.2). Values are tabulated in Table 4. The values of γ calculated from reversible curves are smoother and reach a maximum around 12 at. % Cd, in line with the previously mentioned Fermi surface-Brillouin zone interaction.

As a corollary, the same effects occur in the computation of N(0), the density of states at the Fermi surface, and V, the net interaction energy between electrons. We thus see the superiority of the reversible curves for this phase of the results.

As previously noted, the data for T_c show a kink around 12 at. % Cd. These changes of slope in the T_c data have been attributed to the Fermi surface-Brillouin zone interaction (117).

A number of other superconducting parameters such as the coherence length, velocity of the electrons at the Fermi surface, etc., may also be computed. However, little previous work has been done to correlate these quantities with impurity effects, so that discussion of changes is necessarily limited.

Continuing with the discussion of reversible versus irreversible curves, we note that the value of γ', the thermodynamically computed value of the coefficient of specific heat (computed from Eq. (6.13)), is considerably less erratic when found from the reversible data. Values are shown in Table 9.

The trend noted above is continued in the results for H_{c_1}, the lower critical field. In Fig. 25, we see much less erratic behavior for the reversible values of H_{c_1}. The standard deviation for each alloy concentration also is less for the reversible data.

Now we shall compare the reversible and irreversible data in the light of the GL parameters and associated theories. We again see the superiority of the reversible data.

In Fig. 29, we have the normalized value of $\kappa_1(t)$ plotted as a function of the impurity parameter ρ for the Eilenberger theory (81).

The data from the reversible curves are closer to the theoretical values than the irreversible data; as well, the scattering is substantially lower.

In Fig. 30, the reversible data for the normalized value of $\kappa_1(t)$ versus t is clearly closer to Eilenberger's theory than the irreversible data. In fact, many of the points of the latter data fall below $\kappa_1(t)/\kappa_1(1) = 1$, which is not allowed theoretically.

The same pattern is repeated in Fig. 31, where $\kappa_2(t)$ is presented. The reversible data shows the same superiority over the irreversible data; as in Fig. 30, many of the latter points lie below the theoretical limit.

However, the reversible points themselves in Figs. 30 and 31 have some scatter, and it is difficult to predict a value of ρ from the data.

In Fig. 32, we see a possible explanation of the discrepancies of the value of $\kappa_1(t)/\kappa_2(t)$ which have appeared in the literature. As determined from the graph, this quantity appears to be hysteresis dependent, and since hysteresis varies considerably from one metallurgical system to another, this probably accounts for the contradictory results reported.

The normalized energy gap, $2\Delta(0)/kT_c$, was found to have values above the pure theoretical value of 3.52. As mentioned in the text, this is probably due to a combination of impurity effects and slightly stronger coupling in In-Cd alloys than in pure In.

The Helfand-Werthamer parameter h*(t) has been calculated. In general, we obtain fairly good agreement with theory for the four sam-

ples lowest in Cd concentration. However, at higher concentrations the experimental value of h*(0) diverges significantly from the theoretical value.

Typical values of the variation of $H_{c_2}(t)$ with t are presented in Fig. 37. For the samples with high Cd concentration, $H_{c_2}(t)$ is non-linear as t → 1. The effect is not seen for those samples low in Cd concentration. The reason for the non-linearity is not known. The effect may be noted in a quantitative manner by the large and negative values of D_{o_2} in Table 11.

The same effect occurs in $H_{c_1}(t)$, as seen in Fig. 38.

The discussion of H_{c_1} may be put on a more quantitative basis by considering the GL parameter κ_3, defined by Eq. (7.18). We can calculate values of $H_{c_1}(t)$ by setting $\kappa_1 \simeq \kappa_3$, and this is done in Fig. 39. The reversible theoretical and experimental values of H_{c_1} converge as t → 1, as required by Serin (112). However, when the irreversible data are used, as in Fig. 40, we do not obtain this convergence, indicating that the irreversible data is inadequate.

The amount of flux trapped in the alloys at H = 0 was generally very small, indicating good homogeneity of the samples. The data were fitted to the theory of Budnick et al (114) and produced an apparent fit. However, the result is not conclusive since a number of polynomials could be fitted with the present data.

To summarize, we have explored the magnetic superconducting behavior in the fcc phase of the In-Cd system. The theory of hysteretic magnetization derived in this thesis was used to derive reversible curves from the irreversible data. In a wide variety of ways, the rever-

sible data was found to be superior to the raw irreversible data.

APPENDIX A

EVALUATION OF THEORIES OF HYSTERESIS

The magnetization at any point in a material is

$$4\pi M = B - H \tag{A.1}$$

The average magnetization of a finite body is found by integrating this relationship over its volume and normalizing. Thus

$$4\pi M_{av} = \int (B - H) dV / \int dV$$

We wish to make this equation as simple as possible, and to eliminate demagnetization ratio effects. We assume a long superconducting cylinder whose main axis is parallel to the applied magnetic field. If its length $\ell >> R$, its radius, the demagnetization ratio vanishes. The volume is now $\pi R^2 \ell$, and the infinitesimal volume element is $2\pi \ell R dR$, giving

$$4\pi M = (2/R^2) \int \{B(R) - H\} R dR. \tag{A.1a}$$

We have first assumed no end effects. Secondly, we postulate cylindrical symmetry with respect to magnetic field in the sample. The first assumption is made viable by making the sample of suitable dimensions. The second assumption is valid if the sample is homogeneous. There is then no physical reason for non-cylindrical symmetry in the sample field distribution. We can now discuss the extant hysteresis models for both "hard" (those with extended lattice defects(47)) and Type II superconductors, although the two concepts are not mutually exclusive.

The Bean Model

Bean (48) was the first to discuss the problem of hysteresis in superconductors systematically. The theory assumes a "two-material" superconductor, in which thin filaments of critical field $H_{c_0} >> H_c$, the critical field of the rest of the sample, thread it in a multiply connected system. Although this "sponge" structure has been identified with a dislocation network (49), its relationship with the Abrikosov model is not known. The filaments can carry lossless currents up to $J = J_c$.

Below $H = H_c$, we have a Type I superconductor: $B = 0$. If the applied field is increased beyond this point, some of the outer "soft" material (the mesh) becomes normal, and a supercurrent is induced to flow in the outer filaments. By Ampere's Law, it flows to a depth

$$\Delta = c(H - H_c)/4\pi J_c \qquad (A.2)$$

The interior of the sample, $0 \le r \le R - \Delta$, is shielded by these supercurrents: $B = 0$. The assumption of the "critical state" has been used also. This implied that the supercurrents are either of magnitude J_c or vanish. At $r = R - \Delta$, $B = H_c$. At $r = R$, $B = H$. Assuming linearity in this "penetration depth", we find

$$B = H - K(1 - r/R), \qquad R - \Delta \le r \le R, \quad H_c < H \qquad (A.3)$$

where $K = 4\pi J_c R/c$.

If the external field is increased to $H = H_c + K$, $B = H_c$ at $r = 0$. The bulk properties of the superconductor are then destroyed. Then

$$B = H - K(1 - r/R), \qquad 0 \le r \le R, \quad H \ge H_c + K \qquad (A.4)$$

If Eqs. (A.2), (A.3), (A.4) and their accompanying conditions are substituted into Eq. (A.1a) we obtain

$$4\pi M = -H, \qquad 0 \le H \le H_c$$

$$4\pi M = -H + \frac{(H^2 - H_c^2)}{K} + \frac{H_c^2(3H - 2H_c) - H^3}{3K^2}, \quad H_c \leq H \leq K + H_c$$

$$4\pi M = -K/3, \quad H \geq H_c + K \tag{A.5}$$

The induction B and magnetization for typical values of K are shown in Figs. A.1a and A.1b. Now let us discuss the magnetization when the applied field is decreased. In a subsequent paper, Bean(50) discussed only the case when a field is applied and then reduced to zero. In this case, Bean reasons that the surface currents reverse under the influence of the now reversed emf. Maxwell's equation for this situation in cylindrical symmetry is

$$dB/dr = (4\pi/c)J, \tag{A.6}$$

within the superconductor. Since in Bean's model B has a constant slope, J = const. If, in Fig. A.1a, the total current is to be divided into two sections of equal and opposite magnitude, we merely reverse the slope of B at the point r = R - Δ/2, as shown in Fig. A.1b. Then we have, in analogy with the foregoing,

$$\begin{aligned} B &= H_c + K(1 - r/R), \quad R - \Delta/2 \leq r \leq R \\ B &= H - K(1 - r/R), \quad R - \Delta \leq r \leq R - \Delta/2 \end{aligned} \Bigg\} \quad H_c \leq H \leq K + H_c$$

$$\begin{aligned} B &= H - K(1 - r/R), \quad 0 \leq r \leq r/2 \\ B &= H - Kr/R, \quad\quad\quad R/2 \leq r \leq R \end{aligned} \Bigg\} \quad H \geq H_c + K \tag{A.7}$$

and B = 0 otherwise. The values of magnetization which will be obtained by substituting Eqs. (A.7) into Eq. (A.1a) will be those of the remanent or trapped flux (at H = 0) only. This is because we do not know how B varies with decreasing values of the applied field. Thus the values of magnetization for decreasing H which are shown in Fig. A.1c are merely suggestive of the real curve. Thus
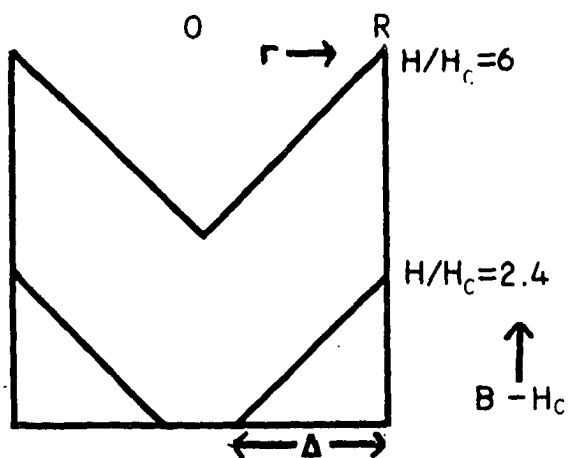
Fig. A.1a. Plot of local
fields in Bean's model for
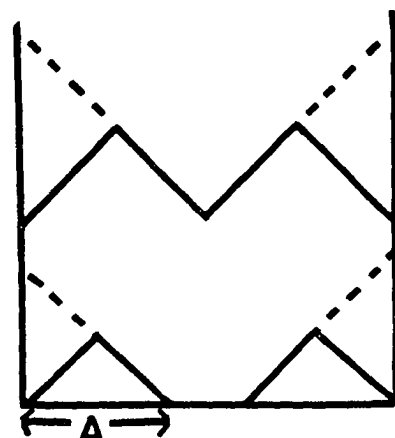increasing magnetic field.
K = 3H$_c$.

Fig. A.1b. Plot of local
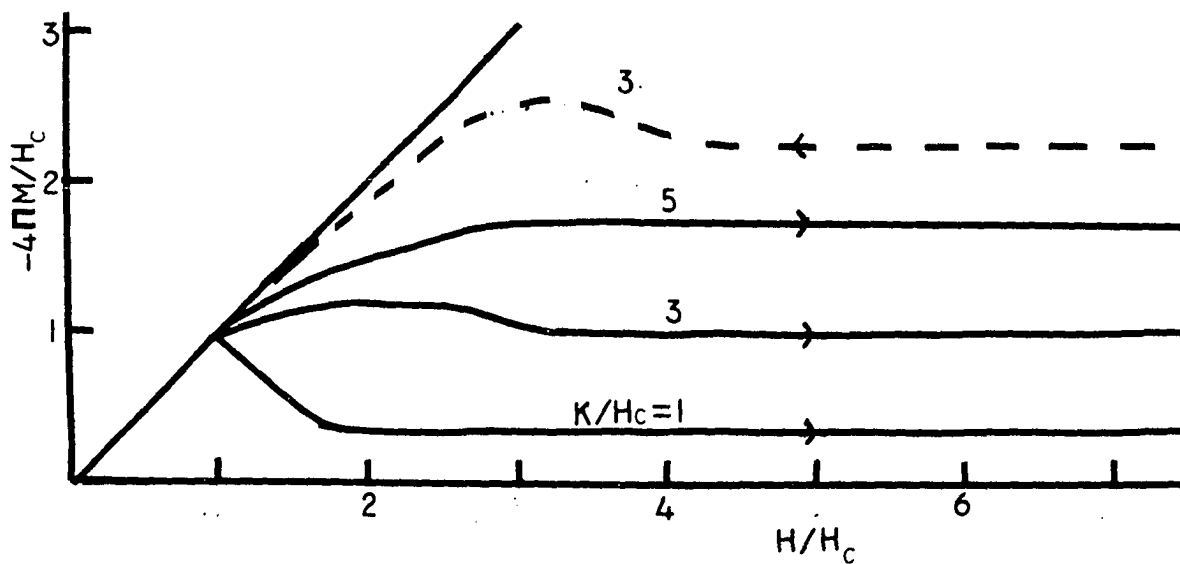fields for decreasing fields.
K = 3H$_c$.

Fig. A.1c. Magnetization as a function of applied field for Bean's model

$$4\pi M = -H, \qquad 0 \le H \le H_c$$

$$4\pi M = -H + \frac{H^2 - H_c^2}{K} + \frac{(H - H_c)^2 (3H_c + H + 2K)}{4K^2}, \qquad H_c \le H \le H_c + K$$

$$4\pi M = -3K/4, \qquad H \ge H_c + K \tag{A.8}$$

The magnetization for the return curve is sketched as a dotted line in Fig. A.1c.

The value of the parameter K, a linear function of the critical current J_c, will determine the shape of the curves. When K is low, the point $H \simeq H_c$ corresponds approximately to $H = H_{c_1}$. As K becomes larger, the maximum of $4\pi M$ becomes smeared out so that it is no longer distinguishable. Furthermore, when $H \ge H_c + K$, the magnetization does not decrease any further, as it does experimentally.

The return curve departs even more from experimental data. Although the curve shown is really a measure only of the trapped flux, we note that the trapped flux is always positive or zero experimentally, whereas in Bean's model it is always negative, and in magnitude greater than the maximum of the magnetization in the forward direction, which is not seen.

Thus although the Bean model shows a resemblance to experimental curves over certain ranges of applied fields for some values of the parameter K, in general it departs from experiment.

The reasons for this are as follows: (1) While the concept of "critical state" may be valid, the supercurrent J_c may be a function of r or B. (2) The assumption that B decreases slowly into the superconductor may be incorrect. It has been shown(44) that B decreases rapidly below the surface for at least some hard superconductors. (3) The reason for the constancy of $-4\pi M$ at high fields is due to the assumption that B varies

directly as H; thus B –H becomes constant. Presumably in real supercon-
ductors B does not quite achieve a linear relationship with H. (4) The
reverse magnetic curve is higher than that for the forward direction be-
cause Bean postulates a decrease in the values of B for this direction.
This decreases B – H and thus $4\pi M$ becomes more negative (see Eq. (A.1a)).
Experimentally, apparently the area under the B curve will increase as
H decreases.

The Kim Model

Kim et al (51) refined Bean's work. Their theoretical conclusions were
based on experimental results on hollow tubes of high field superconduct-
ors (Nb-Zr, Nb-Sn). Kim et al modify Bean's idea of the critical state
to encompass all of the sample, i.e., each region of the sample carries
a critical current density J(B) uniquely determined by the value of B in
that region. Now utilizing equation 5-81 of Jackson (52),

$$J = c(\nabla \times m) \tag{A.9}$$

Combining Eq. (A.9) with Eq. (A.1a), we have

$$B(r) = H + (4\pi/c)\int_{r}^{R} J\{B(r)\}dr \tag{A.10}$$

This cannot be solved in a closed form without simplifying assumptions.

If we differentiate Eq. (A.10) with respect to r, and note that the
external field H has no r dependence, we obtain, using the results of
Fietz et al(53),

$$dB/dr = \pm(4\pi/c)J(B). \text{ Then}$$

$$dB/J(B) = \pm(4\pi/c)dr \tag{A.11}$$

Let B = H at r = R; B = H + $4\pi m(r)$ at r = r, an arbitrary radial
distance. Integrating Eq. (A.11) and making use of these boundary cond-

itions,

$$\int_r^{H + 4\pi m(r)} dB/J(B) = \pm(4\pi/c)(r - R) \qquad (A.12)$$

Based on the experimental data gathered on the hollow tubes, Kim makes the _ad hoc_ assumption that

$$\alpha/J = B + B_o, \qquad (A.13)$$

where α and B_o are constants. Substituting Eq. (A.13) into Eq. (A.12),

$$\pm(4\pi\alpha/c)(r - R) = B_o(4\pi m) + H(4\pi m) + (4\pi m)^2/2,$$

$$4\pi m = -a_1 + \sqrt{a_2 - a_3 r} \qquad (A.14)$$

where $a_1 = B_o + H$, $a_2 = (B_o + H)^2 \mp 8\pi\alpha R/c$, and $a_3 = \mp 8\pi\alpha/c$. The negative surd is unphysical. The total magnetization is

$$4\pi M = (2/R^2) \int_r^R r 4\pi m(r) dr \qquad (A.15)$$

Substituting Eq. (A.14) into Eq. (A.15), after integration we obtain

$$4\pi M = -a_1 + (4/15 a_3^2 R^2)\{ 2a_2^{5/2} - (2a_2 \mp 3A)(a_2 \pm A)^{3/2} \}, \qquad (A.16)$$

where $8\pi\alpha R/c = A$. This last equation is in distinction to Eq. 14 of Kim, valid only for r = 0. Presumably the $\pm$ sign refers to the directions of increasing and decreasing H, respectively. Since we also require B(H,r), we may use Eqs. (A.14) and (A.1) and write

$$B = -B_o + \sqrt{(B_o + H)^2 \mp (A - Ar/R)} \quad , \qquad (A.17)$$

plotted in Figs A.2a and A.2b for the typical values for the parameters of $B_o = 5$ and $A = 10$. The applied field is in units of H_{c_1}.

The curves for increasing H are similar to those of Bean, except that the field B never vanishes at r = 0. Although not evident in Fig. A.2a, using Eq. (A.17) we can see that dB/dr is not constant for different values of H, as it is in Bean's theory.
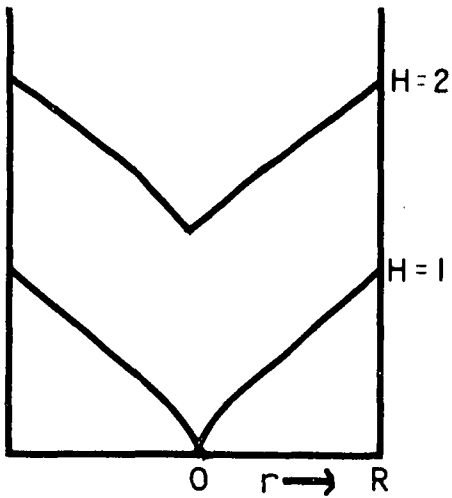
144

Fig. A.2a. Plot of local
fields in Kim's model for
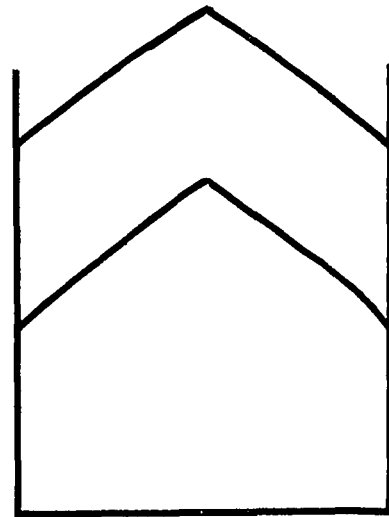increasing magnetic field.
B_o = 5, A = 10.

Fig. A.2b. Plot of local
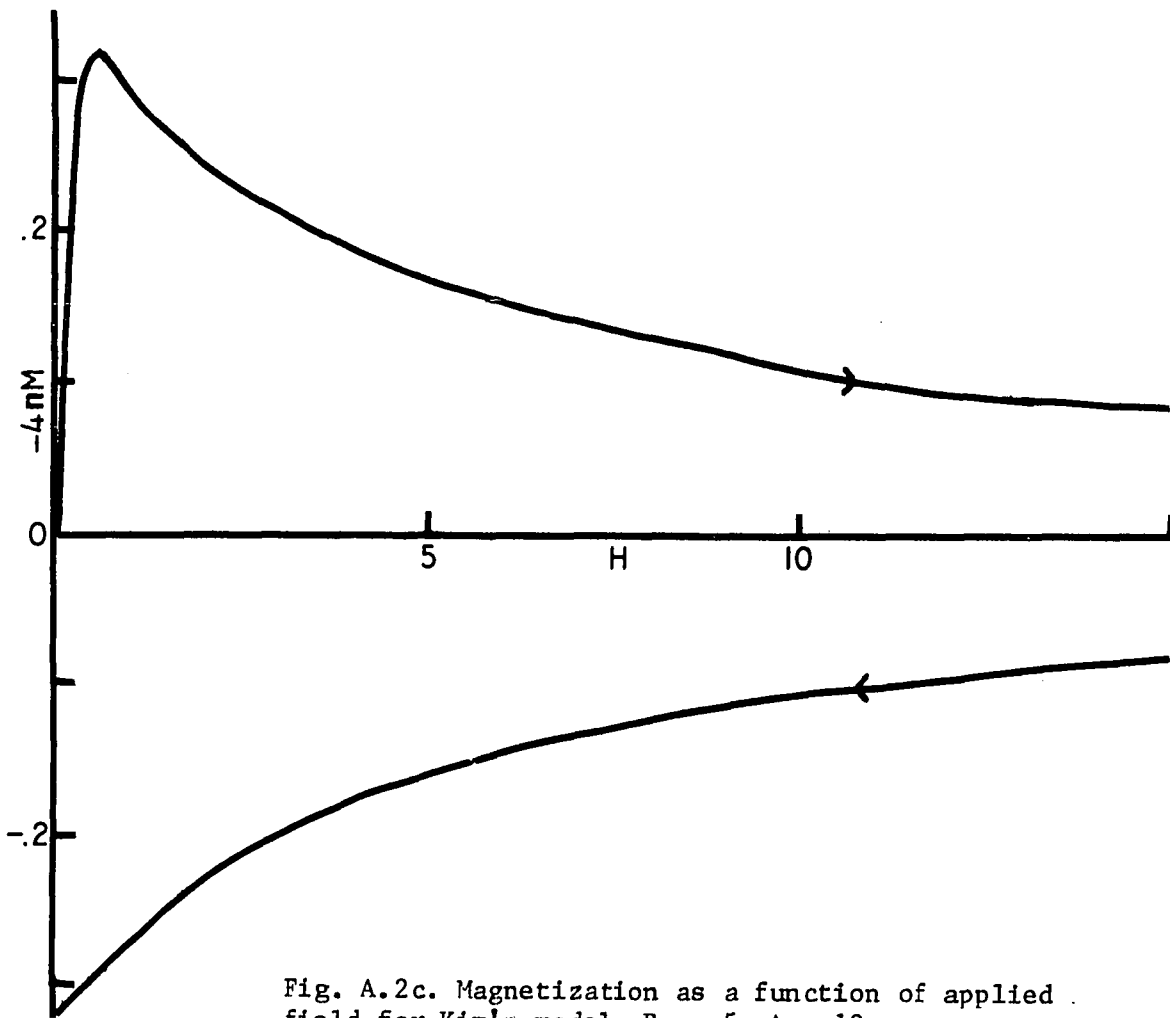fields for decreasing
field. B_o = 5, A = 10.

Fig. A.2c. Magnetization as a function of applied
field for Kim's model. B_o = 5, A = 10.

The curve for B(r) for decreasing H resembles Fig. A.2a strongly, except that the maximum of B is at r = 0. In both Figs. A.2a and A.2b, B = H at r = R. If $(H/H_{c_1}) < 0.91$ for the particular set of parameters $B_o = 5$, A = 10, then B(r) $\leq$ 0 for certain values of r/R for H increasing. This situation is eliminated by specifying that B $\geq$ 0 for all r for increasing H. This condition is taken into account in the calculation of the overall magnetization curve, shown in Fig. A.2c. As above, the magnetization and applied field are in units of H_{c_1}.

Eq. (A.16) is valid only for H > 0.91 in the forward direction; it is valid for all values of H in the reverse direction.

Now let us compare Fig. A.2c with Fig. 12a. There are regions of similarity: the forward curve rises to a maximum and then decreases. However, the magnetization shows no sign of decreasing to zero except as H $\rightarrow \infty$, which is unphysical. The same phenomenon occurs in the reverse direction. Furthermore, the reverse magnetization is always positive and increases monotonically to reach a trapped flux at H = 0 approximately equal to the maximum negative magnetization in the forward direction. While certain hard superconductors exhibit these characteristics, they are by no means universal. Thus, in the light of these departures from experiment, we may say that the Kim model is not a complete description of hysteresis in both Type II and hard superconductors.

The reasons for this are as follows: (1) The critical state concept may not be valid over the entire superconductor. (2) B probably does not equal H slightly below the surface of the superconductor, as mentioned in Bean's model. (3) The configuration of B(r) for decreasing H may have lower values that those shown in Fig. A.2b. This would decrease $4\pi M$ and perhaps make it negative.

Eq. (A.16) is of the same form as the equations in Table I of Fietz et al.

The de Jong Model

de Jong and Blaisse(54) presented a model of completely pinned superconducting filaments. This is a modification of Bean's work, but also takes into account the nature of the "hard" superconducting filaments.

As in Bean's model, the material surrounding the filaments has a critical field H_c. The filaments themselves, of diameter much less than the London penetration depth, have a critical field H_{c_2}, where H_{c_2} is defined by Fig. 12a. The reason for this critical field lies in the next equation. The filaments have a uniform density in the sample, and are concentric with its axis.

According to de Jong, the maximum supercurrent in a filament is

$$I = A\{H_{c_2} - B(r)\} , \qquad (A.18)$$

where A is a constant. From $0 \leq H \leq H_c$, the total sample is diamagnetic due to the shielding currents.

To determine the internal field distribution and magnetization above H_c, we use Eq. (A.18) and its assumption of critical (or maximum) supercurrents. Using Eq. (A.6),

$$dB/dr = \Lambda(4\pi A/c)\{ H_{c_2} - B(r)\} \qquad (A.19)$$

Using the boundary condition $B(R) = H$,

$$B(r) - H = (H_{c_2} - H)(1 - e^{\xi(R - r)}) \qquad (A.20)$$

where $\xi = 4\pi A\Lambda/c$, and Λ is the density of the filaments. Finally, $B = H$ at $r = R - \Delta$, determined by the magnitude of the critical field H_c. This

yields

$$\Delta = (R/\xi)\ln\{(H_{c_2} - H_c)/(H_{c_2} - H)\} \quad , \tag{A.21}$$

for increasing field. When the field decreases, the currents reverse and the constant $A \rightarrow -A$, and $\xi \rightarrow -\xi$.

Graphs of Eq. (A.20) are presented in Figs. A.3a and A.3b. There are two adjustable parameters, H_c/H_{c_2} and ξ.

We see on comparing Fig. A.3a with Fig. A.1a that the two graphs are similar in many respects. The exceptions lie in the curved portions of the upper portions of the internal field. Also, due to the parameters, the region of zero internal field will not in general be the same. Substitution of Eq. (A.20) into Eq. (A.1a) now yields the magnetization curve. We have

$$4\pi M = -H, \quad 0 \leq H \leq H_c. \tag{A.22}$$

Since $B(r) \geq 0$ for all r,

$$4\pi M = (2/R^2)\int_{R-\Delta}^{R} r(H_{c_2} - H)\{1 - e^{\xi(R - r)}\}dr$$

$$= -H + \{(\xi + 1)/\xi^2\}(2H_c - 2H) - (1/\xi^2)(H_{c_2} - H)\ln^2 k_1$$

$$+ \{(\ln k_1)/\xi^2\}\{\xi(2H_{c_2} - H) + 2(H_{c_2} - H_c)\} \tag{A.23}$$

where $k_1 = (H_{c_2} - H_c)/(H_{c_2} - H)$. It will be noted that this equation is somewhat different from de Jong's equation 13, as the latter equation does not provide a matching solution at $H = H_g$. H_g is the value of the external field such that $\Delta = R$, and so $H_g = H_{c_2}\{1 - (1 - H_c/H_{c_2})e^{-\xi}\}$.

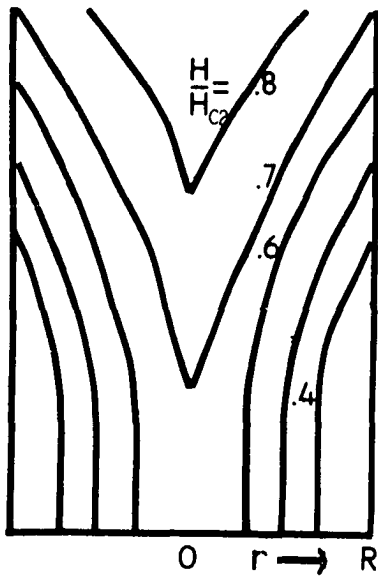Thus Eq. (A.23) is valid only up till $H = H_g$. Above this point, we merely integrate from 0 to R and obtain

Fig. A. 3a. Plot of local
fields in de Jong's model
for increasing magnetic
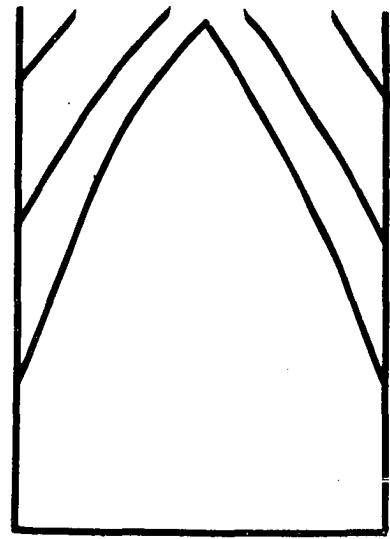field. $H_c = 0.2H_{c_2}$, $\xi = 1$.

Fig. A.3b. Plot of local
fields for decreasing
fields. $H_c = 0.2H_{c_2}$, $\xi = 1$.

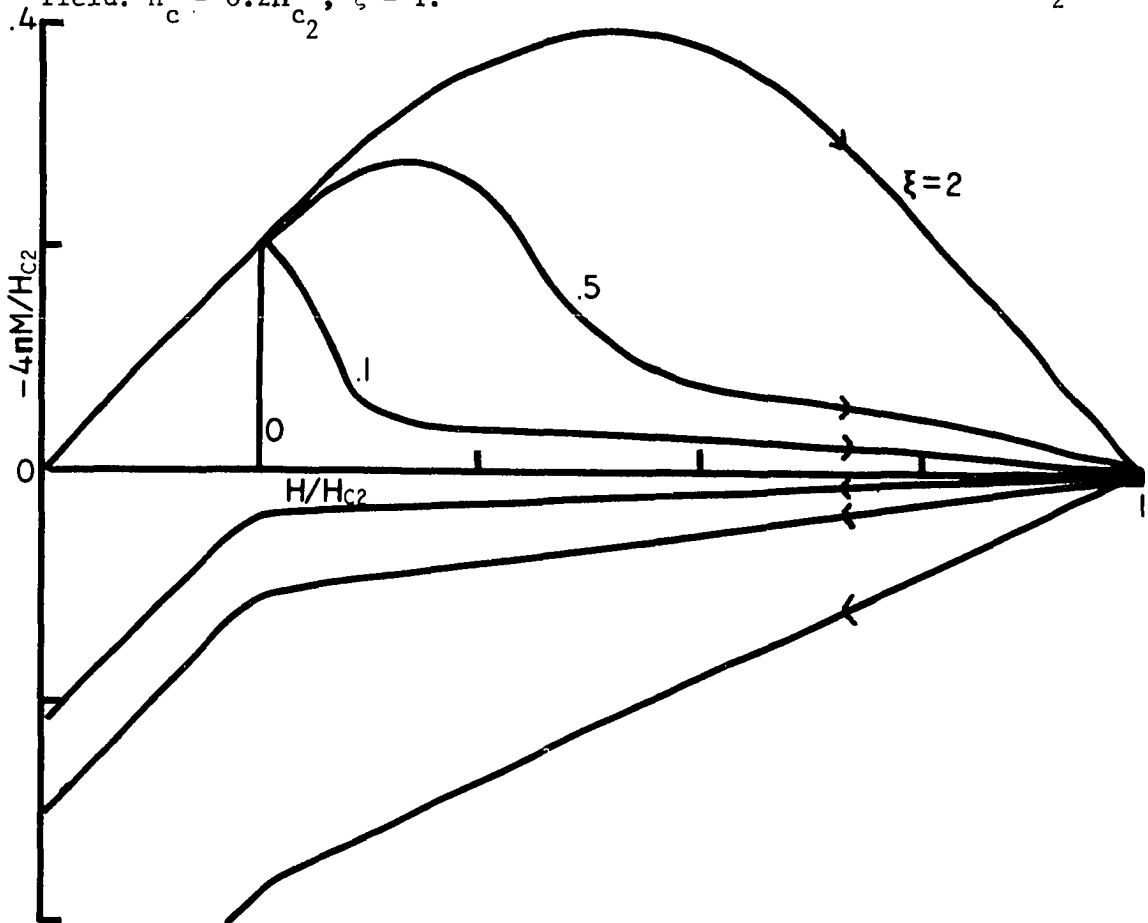
Fig. A.3c. Magnetization as a function of applied field for de Jong's
model. $H_c = 0.2H_{c_2}$.

$$4\pi M = 2(H_{c_2} - H)\{\tfrac{1}{2} + (1/\xi^2)(1 + \xi - e^{\xi})\} \tag{A.24}$$

Now let us consider the curve for decreasing H. Above $H = H_c$, we

change $\xi \to -\xi$ in Eq. (A.24), obtaining

$$4\pi M = 2(H_{c_2} - H)\{\tfrac{1}{2} + (1/\xi^2)(1 - \xi - e^{-\xi})\} \tag{A.25}$$

When $H < H_c$, de Jong specifies that the magnetization decreases diamag-
netically. The results of the above equations are presented in Fig. A.3c.
We can see that they approach the experimental data of Fig. 12a more
closely than the previous theories discussed. We now have a definite van-
ishing of $4\pi M$ at $H=H_{c_2}$. The shape of the forward curve for low values of
ξ resembles that of experimental data. Furthermore, the shapes of the
curves approach those for Type I superconductors for $\xi \to \infty$ or 0, which
would be expected physically.

However, the reverse curve does not agree with data. The shape is
that of strongly hysteretic samples, with the magnetization always pos-
itive. In addition, the trapped flux is always greater than the maximum
of $-4\pi M$, which is not correct. The portions of the forward curve past
$H = H_g$ are linear, which does not agree with theory. This point is dis-
cussed in the main body of this work.

The reasons for these discrepancies are: (1) There is probably not
a uniform density of fluxoids throughout the sample. (2) The fluxoids are
probably not completely pinned for all values of the applied field. (3)
The bulk of the material in the superconductor may not be Type I as postu-
lated.

The Goedemoed Model

Goedemoed et al (55) published a model based on a reversible mag-

netization curve and a hypothesis concerning the pinning force relation-
ship. However, this model is of limited applicability because it makes
use of the linear nature of the reversible magnetization curve near H =
H_{c_2} and is applicable only near there.

The driving magnetic force acting per unit length of a fluxoid is

$$F = (c\phi_o/4\pi\mu)(\partial B/\partial r) \tag{A.26}$$

where ϕ_o is the flux quantum and μ is the slope of the reversible magnet-
ization curve (45). Goedemoed assumes the following relationship between
the maximum pinning force per unit length of fluxoid F_p and induction a-
rising from the interaction between the fluxoid structure and defect
structure:

$$F_p \propto (H_{c_2} - B)$$

At equilibrium, the two forces are equal:

$$\partial B/\partial r = \beta(\mu/\mu_{c_2})(H_{c_2} - B) \tag{A.27}$$

where μ_{c_2} is the reversible constant slope at $H = H_{c_2}$, and β is a con-
stant. Making use of this slope, the magnetization near H_{c_2} is

$$4\pi M = -\mu_{c_2}(H_{c_2} - H). \tag{A.28}$$

Near H_{c_2}, we can generalize Eq. (A.28):

$$4\pi M(r) = -\mu_{c_2}(H_{c_2} - H(r)).$$

Using Eq. (A.1), we then have

$$B(r) = H(r) - \mu_{c_2}\{H_{c_2} - H(r)\} \tag{A.29}$$

When $r = R$, $H(R) = H$. Then

$$B(R) = H - \mu_{c_2}(H_{c_2} - H) \tag{A.30}$$

We deduce that $B \neq H$ at the surface unless $H = H_{c_2}$. Near H_{c_2}, Eq. (A.27)

151

becomes

$$dB/dr = \beta(H_{c_2} - B).$$ (A.31)

Using Eqs. (A.30) and (A.31), we obtain

$$B(r) = H_{c_2} - (1 + \mu_{c_2})(H_{c_2} - H)e^{\beta(R-r)}$$ (A.32)

Substituting Eq. (A.32) into Eq. (A.1a),

$$4\pi M = (H_{c_2} - H)\{1 - 2(1 + \mu_{c_2})\{(e^{\beta R} - 1 - \beta R)/\beta^2 R^2\}\}$$ (A.33)

Graphs of Eqs. (A.32) and (A.33) are presented in Fig. A.4. The graph for decreasing fields is constructed by setting $\beta \rightarrow -\beta$.

In Figs. A.4a and A.4b, the graph of internal fields B are somewhat similar to those previously described. However, in contrast to previous models, $B \neq H$ slightly below the surface of the superconductor. In Fig. A.4c, we note that the curves resemble those of Fig. 12a near $H = H_{c_2}$. The reversible magnetization curve is dotted. By adjusting the parameter βR, the reverse magnetization curve is negative for at least a portion of the range of H, which is often the case experimentally, especially in samples with few defects.

Since it has been shown theoretically that the reversible magnetization curve (and presumably the irreversible curve as well) is linear near $H = H_{c_2}$, Goedemoed's model agrees well with the theory. The only drawback to this work is its limited range of applicability. Any attempt to continue this model to other regions would violate its own assumptions.

A different approach was adopted by Fietz and Webb (FW) (56). Up to now the theories discussed have formulated a model for the internal fields and magnetization, and these results were then compared with experiment. FW formulated a model which used the experimental data to determine a reversible magnetization curve. The shielding currents (assum-
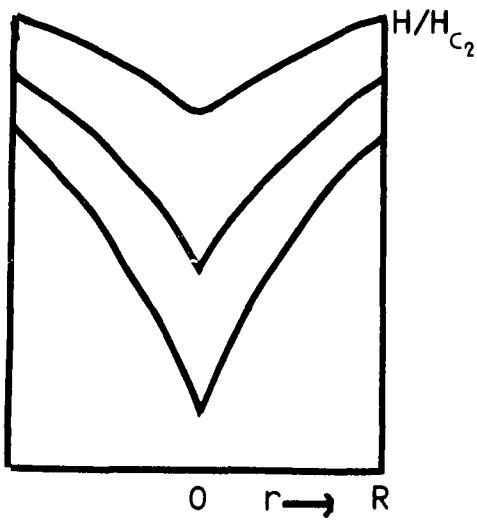
Fig. A.4a. Plot of local
fields in Goedemoed's
model for increasing mag-
netic field. μ_{c_2} = 0.1,
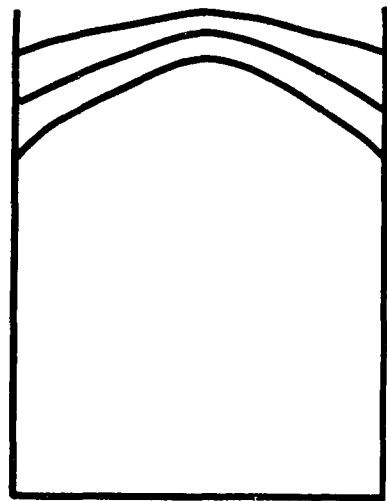βR = 1.

Fig. A.4b. Plot of local
fields for decreasing
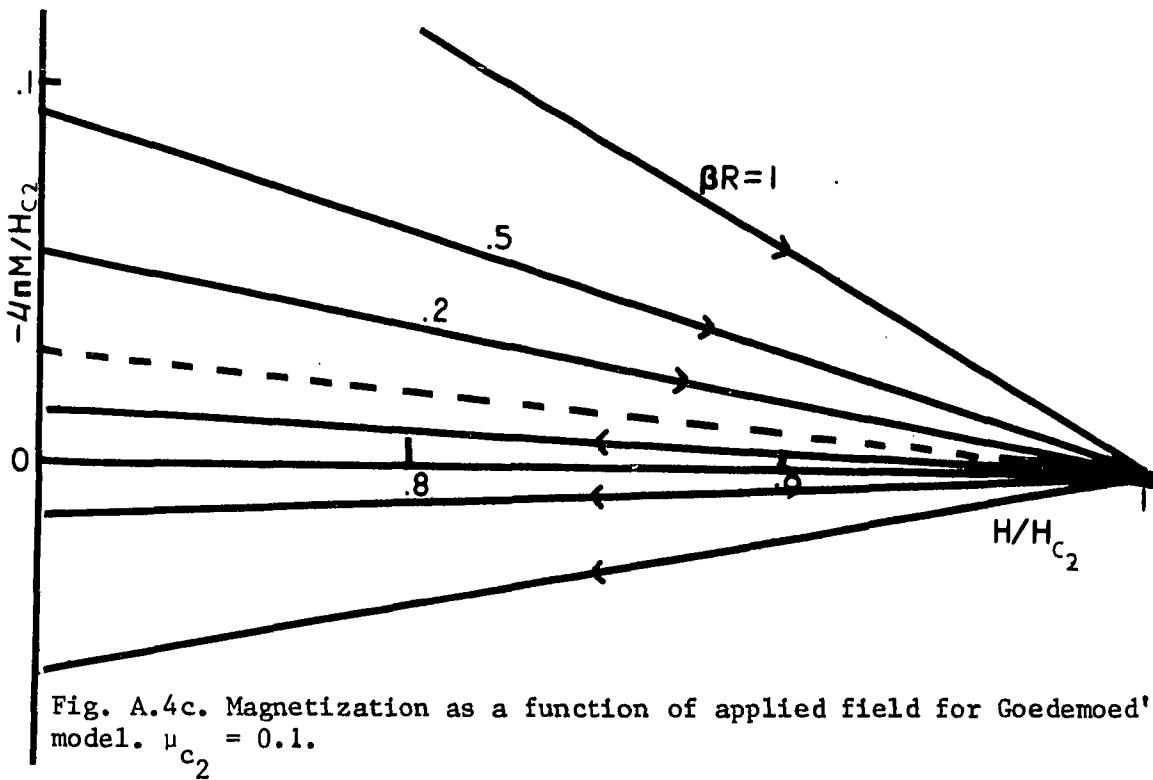fields. μ_{c_2} = 0.1, βR = 1.

Fig. A.4c. Magnetization as a function of applied field for Goedemoed's
model. μ_{c_2} = 0.1.

ed to be critical) are expanded in a Taylor series about the point r = R:

$$J_+(r) = J_+(R) + J'_+(R)(r - R) + J''_+(R)(r - R)^2/2! + \ldots \qquad (A.34)$$

where primes indicate derivatives. This equation applies to the forward curve. Negative subscripts would apply to the reverse curve. Integrating Eq. (A.34) using Eq. (A.6),

$$B_+(r) = B(R) + (c/4\pi)\{J_+(R)(r - R) + J'_+(R)(r - R)/2! + \ldots\} \qquad (A.35)$$

where $B(R) = H + 4\pi M_e$, and $4\pi M_e$ is the reversible magnetization in field H, to be determined. Integrating Eq. (A.35) using Eq. (A.1a),

$$4\pi M_+ = 4\pi M_e + (c/2\pi)(J_+R/3! - J'_+R^2/4! + \ldots) \qquad (A.36a)$$

$$4\pi M_- = 4\pi M_e + (c/2\pi)(J_-R/3! - J'_-R^2/4! + \ldots) \qquad (A.36b)$$

The critical state model assumes a one-to-one correspondence between the magnitude of the critical current and the local field B:

$$\left|J_c(B)\right| = \left|J_+(B)\right| = \left|J_-(B)\right|.$$

Also, from Eq. (A.34) we see that

$$(\partial^n J_+/\partial r^n)\Big|_{r=R} = (-1)^n(\partial^n J_-/\partial r^n)\Big|_{r=R}$$

Using these conditions and adding Eqs. (A.36a) and (A.36b),

$$4\pi(M_+ + M_-) = 2(4\pi M_e) - (2\pi/3c)J_+R^2 + \ldots$$

If the original series converges rapidly, we can write

$$4\pi(M_+ + M_-) \simeq 2(4\pi M_e), \qquad (A.37)$$

which indicates that the reversible magnetization is midway between the upper and lower irreversible magnetization curves.

Because this model uses the experimental data to compute the reversible curve, we cannot use it to independently check other data. In addition, its assumptions generally confine it to regions where $B(r) \neq 0$ for any value of r. These regions of H can be substantial, as noted

in Fig. A.3a. We also have no physical reason why $J_+(R)$ should be negligible with respect to $4\pi M_e$, as postulated. Thus we shall need a physical model of the reversible curve.

The Campbell Model

Campbell et al (37) proposed a hysteresis model similar to that of de Jong and Goedemoed noted above. The major differences lay in the assumption of a different formula for pinning force and a different reversible magnetization curve. Campbell defines a reversible magnetization curve as an approximation to the Abrikosov function: at H_{c_1}, B rises vertically to a value Δ, after which B varies linearly with H with a slope m. Since B = H at H = H_{c_2},

$$m = (H_{c_2} - \Delta)/(H_{c_2} - H_{c_1}) \qquad (A.38)$$

From this description, the pair of straight lines will bear a strong resemblance to the forward curve of Fig. 12b. Thus

$$B_o = \Delta + (H_{c_2} - \Delta)(H - H_{c_1})/(H_{c_2} - H_{c_1}), \qquad (A.39)$$

where B_o is the magnetic induction of the reversible curve. To explain the irreversible curve, Campbell assumes a relationship between pinning force and B of the form

$$F \propto B^{-1}. \qquad (A.40)$$

Using Eqs. (A.40) and (A.26), we have

$$dB/dr = \alpha/2B$$

where α is a constant. Upon integrating,

$$B^2 = \alpha(r - R) + B_o^2, \qquad (A.41)$$

assuming $B = B_o$ at $r = R$. We now have two adjustable parameters, α and Δ.

One problem which arises in integrating Eq. (A.41) is that we have

a non-zero magnetic induction for $H = H_{c_1}$:

$$B^2 = \alpha(r - R) + \Delta^2.$$

To insure that $4\pi M = -H_{c_1}$ at $H = H_{c_1}$, we subtract the magnetization arising from this induction from the overall magnetization. Now $B = 0$ when $r = R - B_o^2/\alpha$. Since we must have $B \geq 0$, the curve for increasing H is divided into 2 regions: $\Delta \leq B \leq \sqrt{\alpha R}$ and $\sqrt{\alpha R} \leq B \leq H_{c_2}$. Using Eq. (A.1a) and the above conditions, we have

$$4\pi M = -H + (4/15\alpha^2 R^2)\{B_o^3(5\alpha R - 2B_o^2) - \Delta^3(5\alpha R - 2\Delta^2)\}, \quad \Delta \leq B_o \leq \sqrt{\alpha R} \tag{A.42}$$

$$4\pi M = -H + (4/15\alpha^2 R^2)\{B_o^3(5\alpha R - 2B_o^2) + 2(B_o^2 - \alpha R)^{5/2}$$
$$-\Delta^3(5\alpha R - 2\Delta^2)\}, \quad \sqrt{\alpha R} \leq B_o \leq H_{c_2}. \tag{A.43}$$

On the reverse curve, $\alpha R \rightarrow -\alpha R$, yielding

$$4\pi M = -H + (4/15\alpha^2 R^2)\{2(B_o^2 + \alpha R)^{5/2} - B_o^3(5\alpha R + 2B_o^2)$$
$$+\Delta^3(5\alpha R + 2\Delta^2)\}, \quad \Delta \leq B_o \leq H_{c_2}. \tag{A.44}$$

Graphs of the above equations are presented in Fig. A.5 for particular values of Δ, αR and H_{c_2}/H_{c_1}. These equations are slightly different from those of Campbell.

The irreversible curves are not defined for $H < H_{c_1}$. The curves for $B(r)$ are somewhat similar to those previously described, but we observe that the irreversible curves are much more similar in shape to those of Fig. 12a than previous models. Another point in favor of this model is that the reversible curve is similar to that calculated by Koppe (38).

Campbell has compared the results of the model with work done on Pb-Bi alloys. However, because of the lack of criteria for a reversible
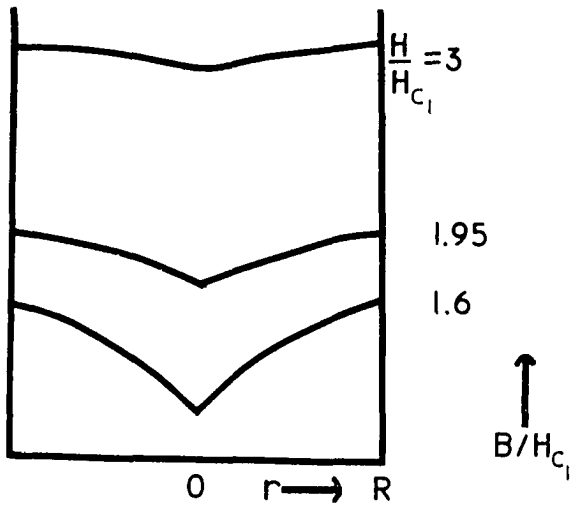
Fig. A.5a. Plot of local
fields in Campbell's mod-
el for increasing field.
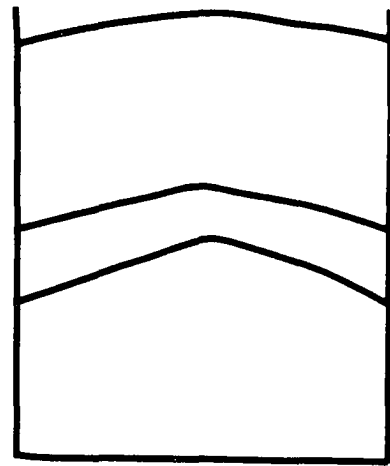$\alpha R = 1$, $\Delta = 0.3H_{c_1}$.

Fig. A.5b. Plot of local
fields for decreasing
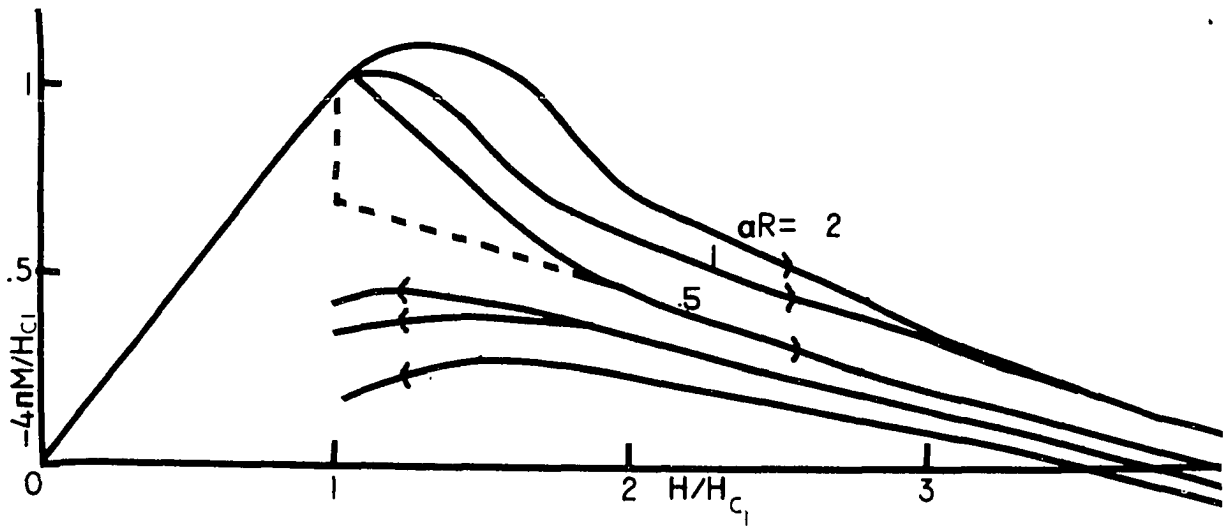fields. $\alpha R = 1$, $\Delta = 0.3H_{c_1}$.

Fig. A.5c. Magnetization as a function of applied field for Campbell's
model. $H_{c_2}/H_{c_1} = 4$, $\alpha R = 1$, $\Delta = 0.3H_{c_1}$.

curve for this data, it was chosen arbitrarily. We shall use some work of Goedemoed (33) to evaluate this model. Another problem which arises is that the reversible curve, for large values of κ, should decrease exponentially (36) rather than linearly. This is discussed in the main text.

The Silcox-Rollins Model

Silcox and Rollins (39) presented a model which determines the fluxoid-fluxoid interaction semi-empirically. The Gibbs free energy of the triangular fluxoid lattice is

$$G = n\varepsilon + f(n) - BH/4\pi,$$

where $f(n)$ is the energy associated with the fluxoid-fluxoid interaction, ε is the energy of each fluxoid, and $B = n\phi_o$, where n is the number of fluxoids and ϕ_o is the flux quantum. Setting $dG/dn = 0$, we obtain

$$\partial f/\partial n = (\phi_o/4\pi)(H - H_{c_1}), \qquad (A.45)$$

where we equate $H_{c_1} = 4\pi\varepsilon/\phi_o$. The authors approximate $f(n)$ by considering nearest-neighbor interactions only. Thus each fluxoid's potential energy $U(a)$ will be multiplied by $z/2$, where a is the equilibrium distance between fluxoids, and z is the coordination number of the fluxoid structure. Thus

$$f(n) = nzU(a)/2 \qquad (A.46)$$

Silcox and Rollins choose a reversible magnetization curve of the form

$$B = H_{c_2}(H - H_{c_1})/(H_{c_2} - H_{c_1}) = n\phi_o, \qquad (A.47)$$

i.e., linear in H. Using Eqs. (A.45), (A.46), (A.47) and the fact that, due to geometry, $n = 2/\sqrt{3}a^2$, we have

$$U(a) = \phi_o^2/\sqrt{3}\pi z\gamma a^2,$$

writing $\gamma = H_{c_2}/(H_{c_2} - H_{c_1})$. Thus

$$dF/da = d^2U(a)/da^2 = (2\sqrt{3}\phi_o^2)/\pi z\gamma a^4 \qquad (A.49)$$

where F is the force between fluxoids.

Now we can equate the pinning forces to the inter-fluxoid forces. These can be written as

$$\sum_i F(x_i) = \rho F_p,$$

where ρ is the density of pinning points along each fluxoid, each with a force F_p. If we expand the last equation in a Taylor series around the equilibrium point x = a, we have

$$6a(dF/dx) = 6a(dF/da)(da/dx) = -\rho F_p, \qquad (A.50)$$

where 6 is the number of nearest neighbors. The quantity x is now taken to be the radial distance in the sample. Silcox takes $n\rho = P$, where P is the density of pinning points through the whole sample, in order to determine ρ. The authors use Friedel's (45) estimate of the force F_p (although the latter's involves a logarithmic term in a):

$$F_p = (H_{c_1}\phi_o)/4\pi \qquad (A.51)$$

Combining Eqs. (A.48), (A.49), (A.50) and (A.51),

$$da/dx = -PH_{c_1}z\gamma a^5/96\phi_o \qquad (A.51a)$$

Integrating and using Eqs. (A.47) and (A.48),

$$B^2 = \beta x + const. \qquad (A.51b)$$

where β is a constant. Using the boundary conditions given by Eq. (A.47) for x = R,

$$B^2 = \{H_{c_2}(H - H_{c_1})/(H_{c_2} - H_{c_1})\}^2 - \beta(R - x) \qquad (A.52)$$

The induction will have a parabolic shape, similar to that of the Campbell model and others. Differences will lie in the boundary conditions chosen, as exemplified by the reversible magnetization curves.
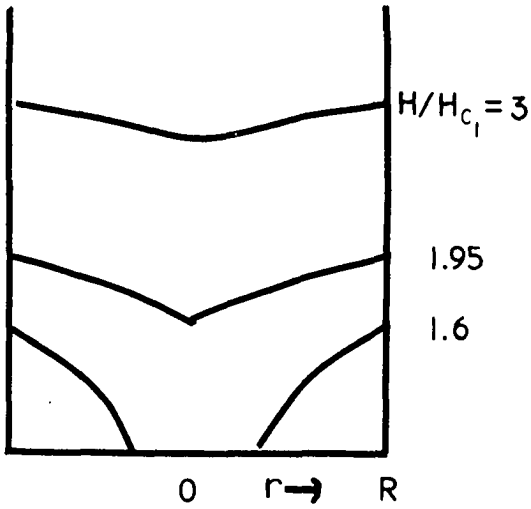
Fig. A.6a. Plot of local
fields in Silcox's model
for increasing magnetic
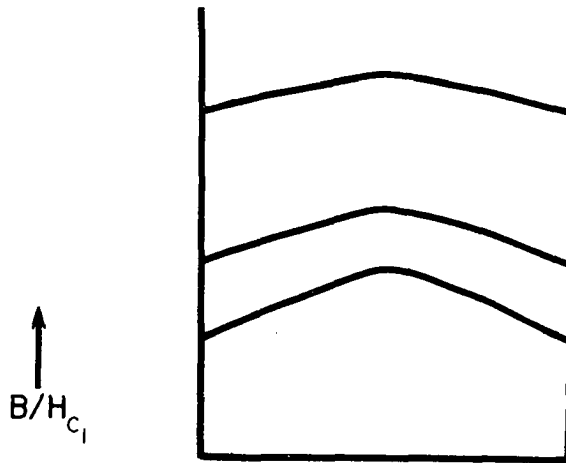fields. $\beta R = 1$, $H_{c_2}/H_{c_1} = 4$.

Fig. A.6b. Plot of local
fields for decreasing
fields. $\beta R = 1$,
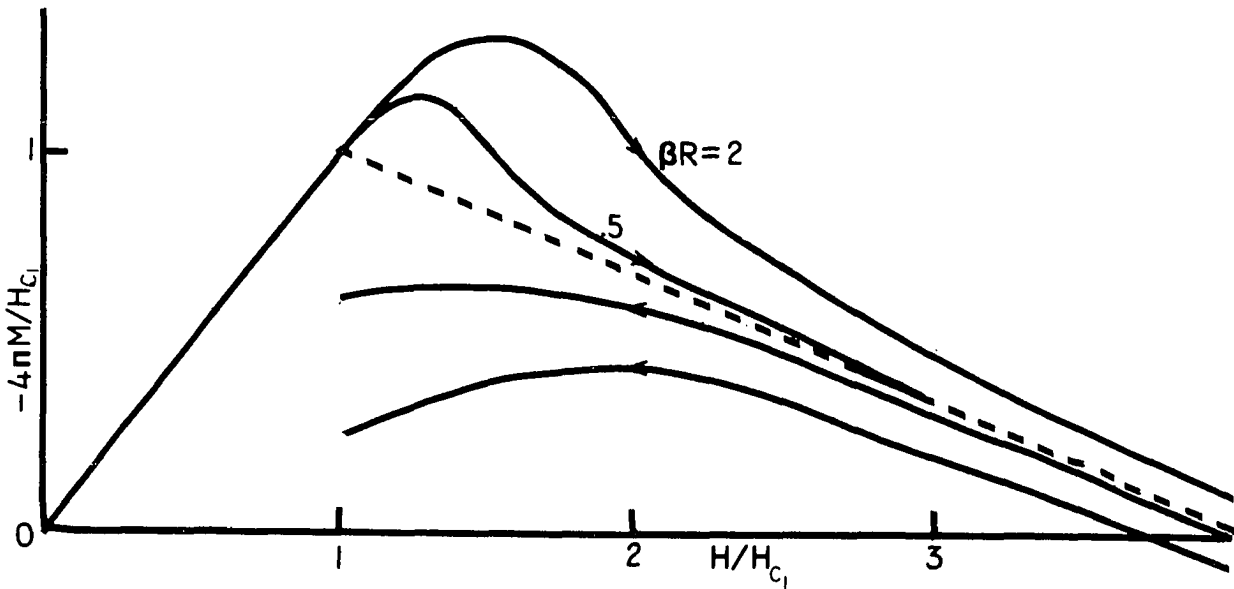$H_{c_2}/H_{c_1} = 4$.

Fig. A.6c. Magnetization as a function of applied field for Silcox's model.
$H_{c_2}/H_{c_1} = 4$.

Integrating Eq. (A.52),

$$4\pi M = -H + \{(4Q^3)/15(\beta R)^2\}\{5\beta R - 2Q^2\}, \quad 0 \le Q \le \sqrt{\beta R} \qquad (A.53)$$

where $Q = H_{c_2}(H - H_{c_1})/(H_{c_2} - H_{c_1})$.

$$4\pi M = -H + \{4/15(\beta R)^2\}\{Q^3(5\beta R - 2Q^2) + 2(Q^2 - \beta R)^{5/2}\},$$

$$\sqrt{\beta R} \le Q \le H_{c_2} \qquad (A.54)$$

For decreasing H, we have

$$4\pi M = -H + \{4/15(\beta R)^2\}\{2(Q^2 + \beta R)^{5/2} - Q^3(2Q^2 + 5\beta R)\}, \quad 0 \le Q \le H_{c_2}$$

$$(A.55)$$

Graphs of the above equations are presented in Fig. A.6. The values of B and $4\pi M$ show a strong resemblance to those of Campbell et al and to experimental data. These two models are compared to experimental data in the main text.

Irie (57) proposed a model for hysteresis which found an internal induction of the form $\lambda B^{2-\gamma} = \lambda_0 B_0^{2-\gamma} - (2 - \gamma)\alpha x/2$, where λ, λ_0, γ and α are constants. However, due to the assumption that B/H is linear near the surface of the sample, magnetization curves were obtained which were very similar to those of Kim(51), and this theory will not be discussed further.

Yasukochi et al (58) used the Silcox-Rollins formulation, with the exception that the density of pinning points along the fluxoids was taken to be of the form $n\rho^2 = P'$, to take account of the region of high fluxoid density. This yields an induction of the form

$$B^{3/2} = B_0^{3/2} - \alpha x. \qquad (A.56)$$

Use of Eq. (A.56) and the assumption that B/H is linear near the surface yields a magnetization of the form

$$4\pi M = -H + (3/20\alpha^2 R^2)\{5(H^{3/2} - \alpha R)^{8/3} - 8H^{3/2}(H^{3/2} - \alpha R)^{5/3} + 3H^4\},$$

$$H_{c_1} \leq H \leq (\alpha R)^{2/3}$$

This expression $\neq H_{c_1}$ when $H = H_{c_1}$, obviating its usefulness.

This completes the critical evaluation of the theories of hysteresis which are presently found in the literature.

LIST OF REFERENCES

1. L. W. Shubnikov, V. I. Khatkevich, J. D. Shepelev, and J. N. Rjab-
    inin, Zh. Eksperim. i Teor. Fiz., $\underline{7}$, 221 (1937).

2. V. L. Ginzburg, L. D. Landau, Zh. Eksperim. i Teor. Fiz., $\underline{20}$, 1064
    (1950).

3. J. Bardeen, L. N. Cooper, and J. R. Schreiffer, Phys. Rev., $\underline{108}$,
    1175 (1957).

4. A. A. Abrikosov, Sov. Phys. JETP, $\underline{5}$, 1174 (1957).

5. B. B. Goodman, Rept. Progr. Phys., $\underline{29}$, 445 (1966).

6. D. Saint-James, G. Sarma, and E. J. Thomas (eds.), Type II Super-
    conductivity, (Pergamon Press, Oxford, 1969).

7. F. London, Superfluids (John Wiley & Sons, New York, 1950), I.

8. U. Essmann and H. Trauble, Phys. Letters, $\underline{24A}$, 526 (1967).

9. K. Maki, Physics, $\underline{1}$, 21, 127 and 201 (1964).

10. C. Caroli, M. Cyrot, and P. G. de Gennes, Solid State Comm., $\underline{4}$, 17
    (1966).

11. B. B. Goodman, IBM J. Res. Devel., $\underline{6}$, 63 (1962).

12. A. A. Abrikosov, Dokl. Akad. Nauk. SSSR, $\underline{86}$, 489 (1952).

13. L. P. Gorkov, Sov. Phys. JETP, $\underline{9}$, 1364 (1964); $\underline{10}$, 998 (1960).

14. J. D. Livingston and H. W. Schadler, Prog. in Mat. Sci., $\underline{12}$, 183
    (1964).

15. T. Heumann and B. Predel, Z. Metallk., $\underline{53}$, 240 (1962).

16. F. N. Rhines, Phase Diagrams in Metallurgy (McGraw-Hill, New York,
    1956).

17. T. Heumann and B. Predel, Z. Metallk., $\underline{50}$, 309 (1959).

18. G. K. White, Experimental Techniques in Low Temperature Physics

(2nd ed., Oxford University Press, London, 1968).

19. M. W. Garrett, J. app. Phys., 22, 1091 (1951).

20. J. F. Cochran, D. E. Mapother, and R. E. Mould, Phys. Rev., 103 1657 (1956).

21. R. G. Chambers and J. G. Park, Brit. J. App. Phys., 12, 507 (1961).

22. P. Zoller and J. R. Dillinger, Am. J. Phys., 37, 519 (1969).

23. F. E. Hoare, L. C. Jackson, and N. Kurti (eds.), Experimental Cryophysics (Butterworths, London, 1961).

24. R. W. Shaw, D. E. Mapother, and D. C. Hopkins, Phys. Rev., 120, 88 (1960).

25. M. Hansen and K. Anderko, Constitution of Binary Alloys (2nd ed., McGraw-Hill, New York, 1958).

26. Sn: W. F. Love, Phys. Rev., 92, 238 (1953); S. L. Wipf, Cryogenics, 3, 225 (1963). In: T. Kinsel, E. A. Lynton, and B. Serin, Rev. Mod. Phys., 36, 105 (1964); K. Noto, Y. Muto, and T. Fukuroi, J. Phys. Soc. Japan, 20, 467 (1965); E. Fischer, Helvetica Physica Acta, 42, 1003 (1969).

27. B. Predel, J. of Less-Common Metals, 7, 347 (1964).

28. G. Knapp and M. F. Merriam, Phys. Rev., 140, 528 (1965).

29. U. Heubner and P. Wincierz, Metall., 7, 703 (1966).

30. R. R. Hake, Phys. Rev., 166, 471 (1968).

31. C. Chiou, R. A. Connell, and D. P. Seraphim, Phys. Rev., 129, 1070 (1963).

32. L. W. Dubeck, D. R. Aston, and F. Rothwarf, J. App. Phys., 41, 1593 (1970).

33. S. H. Goedemoed, A. van der Giessen, D. de Klerk, and C. J. Gorter, Phys. Letters, 3, 250 (1963).

34. J. Bartels et al (eds.), Landolt-Börnstein: Zahlenwerte und Funktionen aus Physik etc. (6th ed., Springer-Verlag, Berlin, 1959), II, Pt. 6, pp. 1, 36.

35. M. F. Merriam, J. Hagen, and H. L. Luo, Phys. Rev., 154, 424 (1967).

36. Saint-James et al, 62.

37. A. M. Campbell, J. E. Evetts, and D. Dew-Hughes, Phil. Mag., 10, 333 (1964).

38. H. Koppe and J. Willebrand, J. of Low Temp. Physics, $\underline{2}$ 499 (1970).

39. J. Silcox and R. W. Rollins, App. Phys. Letters, $\underline{2}$, 231 (1963).

40. B. B. Goodman, C. R. Acad. Sci., Paris, $\underline{258}$, 5175 (1964).

41. P. H. Melville and M. T. Taylor, Cryogenics, $\underline{10}$, 491 (1970).

42. P. G. de Gennes, Superconductivity of Metals and Alloys (W. A. Benjamin, Inc., New York, 1966).

43. M. de Botton and P. Merenda, C. R. Acad. Sci. Paris, $\underline{261}$, 1615 (1965).

44. H. E. Cline, R. M. Rose, and J. Wulff, J. App. Phys., $\underline{37}$, 1 (1966).

45. J. Friedel, P. G. de Gennes, and J. Matricon, App. Phys. Letters, $\underline{2}$, 119 (1963).

46. R. D. Parks (ed.), Superconductivity (Marcel Dekker Inc., New York, 1969), p. 69.

47. Ibid, p. 1109.

48. C. P. Bean, Phys. Rev. Letters, $\underline{8}$, 251 (1962).

49. Saint-James et al, p. 212.

50. C. P. Bean, Rev. Mod. Phys., $\underline{36}$, 31 (1962).

51. Y. B. Kim, C. F. Hempstead, and A. R. Strnad, Phys. Rev. Letters, $\underline{9}$, 306 (1962); Phys. Rev., $\underline{129}$, 528 (1962).

52. J. D. Jackson, Classical Electrodynamics (John Wiley & Sons, Inc., New York, 1967).

53. W. A. Fietz, M. R. Beasley, J. Silcox, and W. W. Webb, Phys. Rev., $\underline{136}$, A335 (1964).

54. L. N. J. de Jong and B. S. Blaisse, Physica, $\underline{31}$, 317 (1965).

55. S. H. Goedemoed, P. H. Kes, F. Th. A. Jacobs, and D. de Klerk, Physica, $\underline{35}$, 273 (1967).

56. W. A. Fietz and W. W. Webb, Phys. Rev., $\underline{178}$, 657 (1969).

57. F. Irie and K. Yamafuji, J. Phys. Soc. Japan, $\underline{23}$, 255 (1967).

58. K. Yasukochi, T. Ogasawara, N. Usui, and S. Ushio, J. Phys. Soc. Japan, $\underline{19}$, 1649 (1964).

59.   J. B. Goodenough, Phys. Rev., 89, 282 (1953).

60.   R. J. Higgins and H. D. Kaehn, Phys. Rev., 182, 649 (1969).

61.   N. E. Phillips, J. C. F. Brock, M. H. Lambert, and M. F. Merriam, presented at Twelfth International Conference on Low Temperature Physics, Kyoto, Japan, 1970.

62.   J. M. Ziman, Electrons and Phonons (Oxford University Press, New York, 1960), p. 58.

63.   M. F. Merriam, M. A. Jensen, and B. R. Coles, Phys. Rev., 130, 1719 (1963).

64.   S. Flugge (ed.), Handbuch der Physik (Springer-Verlag, Berlin, 1956), vol. 19.

65.   P. N. Dheer, Proc. Roy. Soc. (London), A260, 333 (1961).

66.   B. I. Verkin and I. V. Svechkarev, Sov. Phys. JETP, 20, 267 (1965).

67.   M. F. Merriam, Phys. Rev., 144, 300 (1966).

68.   B. B. Goodman, J. Phys. Rad., 23, 704 (1962).

69.   H. R. O'Neal and N. E. Phillips, Phys. Rev., 137, A748 (1965).

70.   D. Markowitz and L. P. Kadanoff, Phys. Rev., 131, 563 (1963).

71.   D. P. Seraphim, C. Chiou, and D. J. Quinn, Acta Met., 9, 861 (1961).

72.   W. L. McMillan, Phys. Rev., 167, 331 (1968).

73.   Parks, p. 542.

74.   P. Morel and P. W. Anderson, Phys. Rev., 125, 1263 (1962).

75.   T. P. Sheahen, Phys. Rev., 149, 368 (1966).

76.   L. V. Delvecchio and P. Lindenfeld, Phys. Rev. B, 1, 1097 (1970).

77.   R. I. Gayley, E. A. Lynton, and B. Serin, Phys. Rev., 126, 43 (1962).

78.   A. Ikushima and T. Mizusaki, J. Phys. Chem. Solids, 30, 873 (1969).

79.   Y. Kubota, T. Ogasawara, and K. Yasukochi, J. Phys. Soc. Japan, 29, 1209 (1970).

80.   L. P. Gorkov, Sov. Phys. JETP, 10, 998 (1960); 10, 593 (1960).

81.   G. Eilenberger, Phys. Rev., 153, 584 (1967).

82. E. Bucher, F. Heiniger, J. Muheim, and J. Muller, Rev. Mod. Phys., 36, 146 (1964).

83. J. K. Hulm, R. D. Blaugher, T. H. Geballe, and B. T. Matthias, Phys. Rev. Letters, 7, 302 (1961).

84. D. U. Gubser, D. E. Mapother, and D. L. Connelly, Phys. Rev. B, 2, 2547 (1970).

85. Parks, p. 734.

86. A. B. Pippard, Repts. Prog. Phys., 23, 176 (1960).

87. E. A. Lynton, Superconductivity (Metheun & Co. Ltd., London, 1964), p. 19.

88. N. Usui, T. Ogasawara, K. Yasukochi, and S. Tomoda, J. Phys. Soc. Japan, 27, 574 (1969).

89. T. Ogasawara, Y. Kubota, and K. Yasukochi, J. Phys. Soc. Japan, 25, 1307 (1968).

90. D. E. Farrell, B. S. Chandrasekhar, and H. V. Culbert, Phys. Rev., 177, 694 (1969).

91. T. Kinsel, E. A. Lynton, and B. Serin, Rev. Mod. Phys., 36, 105 (1964).

92. D. L. Decker and H. L. Laquer, J. App. Phys., 40, 2817 (1969).

93. K. Hechler, G. Horn, G. Otto, and E. Saur, J. Low Temp. Physics, 1, 29 (1969).

94. E. Helfand and N. R. Werthamer, Phys. Rev., 147, 288 (1966).

95. H. V. Culbert, D. E. Farrell, and B. S. CHandrasekhar, Solid State Comm., 7 571 (1969).

96. E. Trojnar, Physica, 45, 357 (1969).

97. T. McConville and B. Serin, Phys. Rev., 140, A1169 (1965).

98. J. E. Evetts and J. M. A. Wade, J. Phys. Chem. Solids, 31, 973 (1970).

99. Saint-James et al, p. 147.

100. C. J. Gorter and H. B. G. Casimir, Physica, 1, 306 (1934).

101. J. Bardeen and J. R. Schreiffer, Progress in Low Temperature Phys-

ics, ed. C. Gorter (North Holland Press, Amsterdam, 1961), vol. 3, p. 170.

102.   J. Bardeen and M. J. Stephen, Phys. Rev., 140, A1197 (1965).

103.   Lynton, p. 99.

104.   J. C. Swihart, D. J. Scalapino, and Y. Wada, Phys. Rev. Letters, 14, 106 (1965).

105.   G. Bergmann, Z. Physik, 228, 25 (1969).

106.   S. T. Sekula and R. H. Kernohan, J. Phys. Chem. Solids, 27, 1863 (1966).

107.   A. Ikushima, T. Mizusaki, and T. Odaka, Phys. Letters, 26A, 582 (1968).

108.   N. R. Werthamer and W. L. McMillan, Phys. Rev., 158, 415 (1967).

109.   J. L. Harden and V. Arp, Cryogenics, 3, 105 (1963).

110.   A. R. Eastham, unpublished Ph.D. dissertation, Dept. of Physics, University of Warwick, Coventry, England, 1969.

111.   L. Neumann and L. Tewordt, Z. Physik, 189, 55 (1966).

112.   Parks, p. 930.

113.   J. Jurisson and R. J. Oakes, Phys. Letters, 2, 187 (1962).

114.   J. I. Budnick, E. A. Lynton, and B. Serin, Phys. Rev., 103, 286 (1956).

115.   Parks, p. 779

116.   Ibid., pp. 71, 74.

117.   M. J. Merriam, Phys. Letters, 17, 16 (1965).

118.   J. J. Hopfield, Phys. Rev., 186, 443 (1969).

119.   J. M. Ziman, Principles of the Theory of Solids (Cambridge University Press, Cambridge, 1965), p. 63.